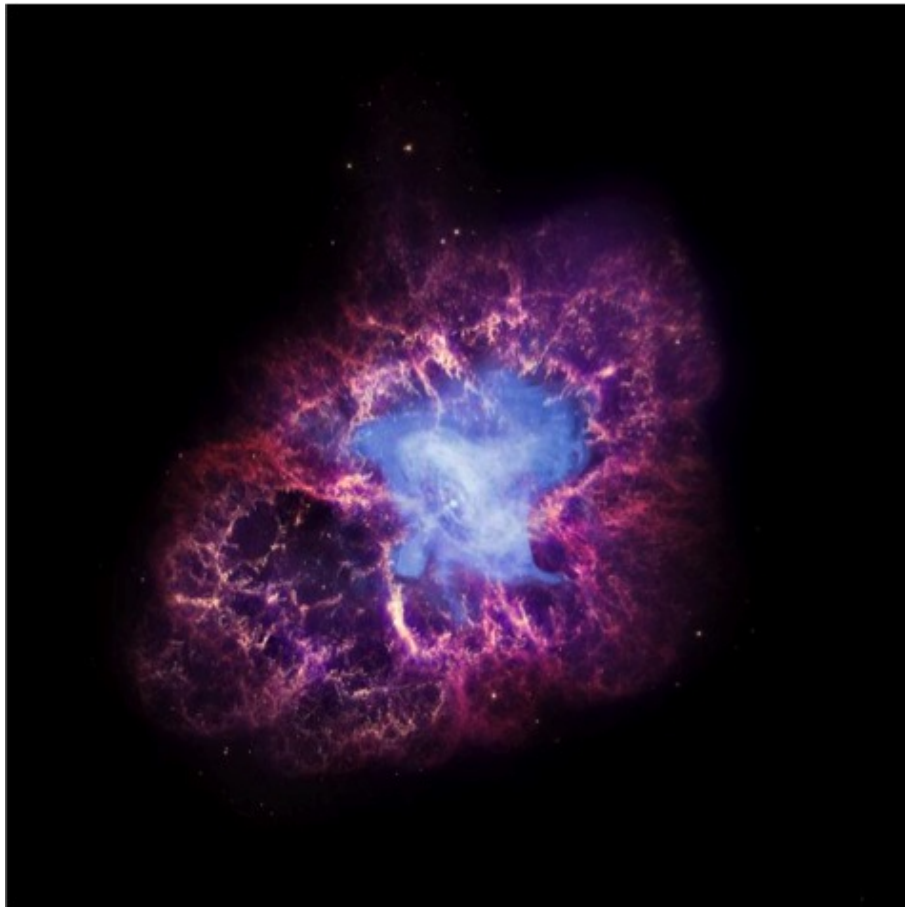


SUPERNOVA REMNANTS AND PULSAR WIND NEBULAE IN THE NORMA REGION

MASTER THESIS



SIMONE F. JUUL JAKOBSEN
8. JUNI 2013

MAIN ADVISOR: DARACH WATSON
CO-ADVISOR: JOHN TOMSICK
CO-ADVISOR: ALLAN HORNSTRUP

* NIELS BOHR INSTITUTE, COPENHAGEN UNIVERSITY 2013 *

Abstract

This thesis reports on the discovery of a new extended X-ray source that is well described by the expected properties of a moving pulsar driving a so called pulsar wind nebula. The discovery was done with the Chandra X-ray observatory in connection to a scheduled survey of the Norma region. The source exhibits a spectrum fitted well with an absorbed power law model. Comparing the Chandra spectrum of the source with one obtained from an archived XMM Newton observation results in best fit parameters $nH \sim 17 \times 10^{22} \text{ cm}^{-2}$ and $\Gamma \sim 1.25$. A spatial spectral investigation performed using Chandra data shows signs of spectral softening with increasing radius from the emission peak.

Inferring a lower bound on the distance to the source of $\sim 14 \text{ kpc}$ based on the large absorbing column, a spin-down luminosity of $\dot{E} \sim 7 \times 10^{36} \text{ erg s}^{-1}$ is estimated for the pulsar candidate.

Combining the Chandra data with radio data from the Molonglo Galactic Plane Survey epoch-2 (MGPS-2), reveals a cometary structure in X-rays and an elongated tail-like structure in radio. The emission is consistent with what is expected for a pulsar wind nebula and the observed structure is therefore used in order to calculate a Mach number $M \approx 3$ for the supposed pulsar. A light curve was extracted to search for pulsations, but no useful information could be extracted, because of the poor photon statistics.

Additionally this work presents the first detection of X-ray emission from an arc like structure in connection to the supernova remnant G337.2+00.1. The emission is deemed significant based on the result of an F-test and is interpreted as the forward shock interacting with a molecular cloud, based on the fact that it is nicely correlated with radio emission from the remnant. The detected remnant shell is positioned at a distance of $\sim 109 \text{ arcsec}$ from the center of the remnant, and this value is used together with the Sedov-Taylor self-similar solutions to achieve an approximate age of the remnant of $\sim 1400 \text{ yr}$. This is a value similar to what has been found previously and makes G337.2+00.1 a member of the historical supernova remnants with the explosion occurring sometime in the 7th century. Finally I present in this thesis the first Chandra detection of the mixed-morphology remnant G337.8-00.1.

Resumé

Dette speciale beskriver den første detektion af en ny udstrakt röntgenkilde, hvis egenskaber kan beskrives fyldestgørende som konsekvenser af en pulsar der bevæger sig supersonisk og driver en såkaldt pulsar vind. Kilden var detekteret med Chandra X-ray observatory i forbindelse med et planlagt studie af området omkring Norma spiralarmen i Mælkevejen kaldet Norma regionen. Kilden viser et spektrum der kan beskrives med en absorberet eksponentialfunktion og sammenligner man spektret opnået ved brug af Chandra data med det opnået ved brug af XMM Newton data, resulterer det i en bedste fit absorption af størrelsen $nH \sim 17 \times 10^{22} \text{ cm}^{-2}$ og et foton index med værdi $\Gamma \sim 1.25$. En undersøgelse af variationer af spektret henover kilden afslører tegn på at spektret bliver blødere med stigende afstand fra punktkilden.

Hvis man accepterer en nedre grænse for afstanden til kilden på $\sim 14 \text{ kpc}$ som er fundet ud fra den svære absorption, kan man udregne en spin-down luminositet af størrelsen $\dot{E} \sim 7 \times 10^{36} \text{ erg s}^{-1}$ for den formodede pulsar.

Kombinerer man Chandra data med radio data fra Molonglo Galactic Plane Survey epoch-2 (MGPS-2), er det tydeligt at kilden udviser en kometstruktur i röntgen og en længere udstrakt hale i radio området. Denne struktur er i overensstemmelse med hvad man ville forvente for en pulsar der driver en magnetiseret vind. Denne struktur er videre brugt til at estimere et Mach nummer $M \approx 3$ for pulsaren. Det var ydermere forsøgt at udtrække en lyskurve fra objektet for at lede efter tegn på pulsering. Dette var dog ikke muligt, siden kilden er svag, og der kun var meget få fotoner til rådighed.

Dette speciale præsenterer også den første detektering i röntgenområdet af en halvcirkel af emission der ser ud til at have en forbindelse til supernova resten G337.2+00.1. Den diffuse emission er bestemt til at være signifikant på baggrund af en F-test, og er forstået som den udadgående shock front fra supernova eksplosionen der nu interagerer med en molekylær sky. Dette er udledt på baggrund af sammenligning med radiodata som viser sig at være i overensstemmelse med denne konklusion. Den udadgående shock front er bestemt til at ligge i en afstand af $\sim 109 \text{ arcsec}$ fra centrum af supernova resten og denne værdi i sammenhæng med Sedov-Taylor løsninger giver et estimat af supernova restens alder på $\sim 1400 \text{ yr}$. Det er en værdi der er i overensstemmelse med hvad man har fundet andetsteds og gør G337.2+00.1 til et medlem af de historiske supernova rester, siden den forudgående supernova eksplosion fandt sted i starten af det 7. århundrede.

Endelig præsenterer jeg den første Chandra observation af en mixed-morphology supernova rest kaldet G337.8-00.1.

Indhold

1	Introduction	6
2	Supernova remnants: structure and evolution	8
2.1	Supernovae	8
2.1.1	Thermonuclear supernovae - type Ia	8
2.1.2	Core collapse supernovae type II, Ib and Ic	9
2.2	The evolution of supernova remnants	10
2.2.1	Phase I: The ejecta dominated phase	11
2.2.2	Phase II: The Sedov-Taylor phase	13
2.2.3	Phase I - II: The Truelove & McKee transition phase	13
2.2.4	Phase III and IV: The radiative snowplough phase and the merging phase	14
2.3	Shock heating	15
2.4	Cosmic-ray acceleration	16
2.5	Pulsar wind nebulae (PWNe)	16
2.5.1	Pulsar wind nebula evolution	18
3	Supernova remnants: observational characteristics	20
3.1	Emission processes in supernova remnants	20
3.1.1	Thermal continuum emission	20
3.1.2	Thermal line emission	22
3.1.3	Non-thermal emission	22
3.2	Shell type remnants	23
3.3	Pulsar wind nebulae - young pulsars	24
3.4	Bow-shock nebulae - evolved pulsars	26
3.5	Composite remnants	27
3.5.1	Plerionic composites	27
3.5.2	Thermal composites/Mixed morphology remnants	28
4	The Chandra Norma region survey	29
4.1	The extended sources of the Norma survey	29
4.2	G337.2+00.1	32
4.3	CXOU J163802.6-471358	33
4.4	G337.8-00.1/Kes41	33
5	This thesis - open questions	35
5.1	G337.2+00.1	35
5.1.1	Morphological typing	35
5.2	CXOU J163802.6-471358	36
5.3	G337.8-00.1	37
6	Methodology	38
6.1	Filtering data	39
6.1.1	Removing contaminating sources	39
6.2	X-ray imaging	39
6.2.1	Merging event files	39
6.2.2	Exposure correction	40
6.2.3	Radial profile	41

6.2.4	Determining the Chandra PSF	41
6.3	X-ray spectroscopy	41
6.3.1	Spectral extraction	41
6.3.2	Spectral fitting with XSPEC	42
6.4	Statistical analysis	43
6.4.1	Fit statistics	43
6.4.2	Error estimations	44
6.4.3	The F-test	45
7	Results	46
7.1	G337.2+00.1	46
7.1.1	The morphology of SNR G337.2+00.1	46
7.1.2	The point-like central emission	47
7.1.3	The spectral properties of SNR G337.2+00.1	49
7.2	CXOU J163802.6-471358	54
7.2.1	The spectral properties of CXOU J163802.6-471358	55
7.3	G337.8-00.1	63
7.3.1	The spectral properties of G337.8-00.1	64
8	Discussion	67
8.1	G337.2+00.1	67
8.2	CXOU J163802.6-471358	70
8.3	G337.8-00.1	75
9	Conclusion	76
9.1	G337.2+00.1	76
9.2	J163802.6-471358	76
9.3	G337.8-00.1	77
10	Further investigations	78
	Litteratur	79

1 Introduction

Supernova remnants (SNRs) are the relics of some of the most extreme events occurring in our Universe, namely supernova explosions (SNe). Starting out at the verge of the explosion the several solar masses of ejecta is thrown from the dying star and into the interstellar medium, carrying a kinetic energy of the order 10^{51} erg. The interaction and abrupt deceleration of the expanding ejecta forms a shock front that will expand into the interstellar medium throughout the course of several tens of thousands of years. The structure resulting from the interaction between the ejecta material and the interstellar medium, is what we refer to as the SNR.

Besides being beautiful to the eye, SNRs are also of great scientific importance. They are for instance responsible for the recurring chemical enrichment of the interstellar medium by distributing the products of the progenitor star nucleosynthesis into the ambient medium, and their shock fronts are thought to be the prime candidates for acceleration of Galactic cosmic rays.

Several hundreds of SNRs are known to reside in our own Galaxy, and as the technology evolves and more sensitive telescopes are being build, more are discovered. The main part of the SNR population was first discovered at radio wavelengths, but SNRs emit radiation across the whole electromagnetic spectrum during their evolution. Probably the best known supernova remnant is the Crab nebula which is also featured in the image on the front page of this thesis. That this is strictly speaking not a supernova remnant but rather a so called pulsar wind nebula will be discussed later in this thesis, but none the less is the Crab nebula still a good example of how complex in structure the relics of a supernova can be. The constant improvement of the spatial resolution of X-ray telescopes makes it possible to investigate the very center of remnants like the Crab nebula, where the high energy photons probe the sites where particles are being accelerated to ultra relativistic energies. It is exactly the sensitivity of such telescopes, as for instance the Chandra X-ray Observatory, that has made it possible to make SNR shocks the favored venues for recurring acceleration of Galactic cosmic rays (Vink 2011).

In this thesis I focus on the X-ray part of SNR emission, and by making use of the excellent spatial resolution of the Chandra X-ray observatory we examine three extended sources located in a small spiral arm in our Galaxy called the Norma arm. The SNR nature of two of the sources (G337.2+00.1 and G337.8-00.1) have been investigated elsewhere but have not previously been observed with Chandra, whereas the third (CXOU J163802.6-471358) is a new source of unknown origin. The scope of this thesis is therefore to investigate the spatial structure of all three sources, and through spatial and spectral analysis seek to determine the source type for the new extended object.

The thesis structure is meant to provide a chronological walk-through of the theoretical background needed to carry out the investigations that form the main part of this project. Chapter 2 sets in with an introduction to SNRs from a theoretical point of view. That being an overview of the different evolutionary phases of SNRs and the physics lying behind. Chapter 3 contains the observational aspects of SNRs and PWNe. That is, the emission processes and the observational characteristics of different types of SNRs and PWNe. Chapter 4 introduces the motivation for doing this investigation and presents the a priori knowledge about the sources that are the focus of the investigation. Chapter 5 presents the detailed scope of the project. That being the open questions about the three sources which we will aim at answering through a series of imaging and spectroscopic investigations. Chapter 6 presents the methodology of the project including the statistics used. In Chapter 7 we present the results from the investigations introduced in Chapter 5 and 6. Chapter 8 offers a discussion of the results presented in Chapter 7. Chapter 9 holds the conclusions made, based on all the previous Chapters.

It is to be noted that this thesis focuses on the X-ray part of SNR emission. Almost all analysis done in this thesis is based on Chandra data, which means that I do not provide any detailed description of methods for XMM Newton, MGPS-2, Spitzer or Vista data reduction, as that is beyond the scope of the project. Comparison is made between results from the X-ray analysis done in this thesis and results from previous radio investigations, but no detailed description of the radio analysis methods is provided.

The additional data is only used for comparison purposes and have not been processed in any way, and in the case of XMM Newton, the spectra used in the fitting analysis was provided by John Tomsick, meaning that no insight in spectral extraction of XMM data is presented. Furthermore is it noted that the main focus has been on two of the three sources mentioned (G337.2+00.1 and CXOU J163802.6-471358) because of the timeline of the project and because of the distinctly different nature of the third source.

2 Supernova remnants: structure and evolution

In the following chapter I introduce some basic properties of SNRs. I present a description of the structure of SNRs and their evolutionary phases and mention some of the models and simulation results that the theory is based on.

2.1 Supernovae

Supernovae (SNe) are violent bursts of energy of the order of $\sim 10^{51}$ erg (Woosley & Janka 2005).

SNe are first and foremost classified based on their spectral characteristics in the optical. SNe which do not contain hydrogen are called type I, and the rest are of type II, because they exhibit a $H\alpha$ line in their spectra (Minkowski 1941; Vink 2011; Reynolds 2008). Furthermore, each group can be divided into several subgroups.

The supernovae without hydrogen in their spectra are of type Ia if a silicon line is observed, type Ib if there is no silicon but helium present, and Ic if there is no silicon and no helium lines (Filippenko 1997; Vink 2011; Reynolds 2008).

The type II supernovae are divided into subgroups based on their light curve shapes in the photospheric phase, which is the phase where the star is still opaque to radiation and therefore dominated by the properties of the stellar envelope (Schaeffer 2003). The type II supernova light curve generally shows a rise to a peak brightness followed by a decline. The decline in brightness determines the type, where type IIP shows a plateau with the brightness declining slowly, and type IIL shows a linear, quick decline. The Type IIb supernova is somewhat different as it is an intermediate class between type II and type Ib. It starts out as a type II, but later the spectrum evolves into a type Ib spectrum (Filippenko 1997; Vink 2011; Reynolds 2008).

A new additional type is the IIn supernova, which is characterized by narrow hydrogen emission lines and a slowly declining light curve. They are believed to originate from a dense circumstellar medium (CSM) that might have been created by progenitor stellar winds (Filippenko 1997).

The physics governing the explosion processes in supernovae are still being uncovered, but it is possible to divide supernovae into two broad categories based on their explosion mechanisms: thermonuclear supernovae and core collapse supernovae. Type II events are all of the core collapse type, whereas type I's can be both thermonuclear- or core collapse supernovae.

2.1.1 Thermonuclear supernovae - type Ia

Type Ia supernovae are believed to be the result of a thermonuclear explosion of a CO white dwarf. The white dwarf consists of degenerate matter, governed by the Pauli exclusion principle, and the electron degeneracy pressure is what supports the white dwarf from collapse (Shapiro 1991; Leibundgut 2001; Schaeffer 2003). White dwarfs are found among old stellar populations, which indicate that they do not have massive stars as their progenitors. Instead the explosion is ignited by violent nuclear burning caused by the white dwarf exceeding the Chandrasekhar mass limit ($1.44 M_{\odot}$ (Janka et al 2007)). It is obvious that the extra material must come from accretion, but it is not clear what kind of progenitor system is needed, other than it must be a binary one. Whether it is a white dwarf and a main sequence or evolved star (single degenerate system) or two white dwarfs (double degenerate system) is not clear (Vink 2011).

The peak brightness for all type Ia SNe are very similar which goes hand in hand with the idea that all type Ia explosions have the same progenitor. This is one of the reasons why SNe type Ia have been used extensively as standard candles for distance measurements. Some observations of SNe Ia show a deviation from the standard picture though, which could indicate that all type

Ia events cannot be described with the exact same model (Leibundgut 2001).

Several models for SNe Ia events are considered: detonation models, deflagration models, and delayed detonation models and all of them have their own issues. Detonation models describe how a supersonic wave travels through the white dwarf, heating up and igniting the material. This process would lead to an overabundance of iron-group elements and an underabundance of intermediate- mass elements compared to observations (Leibundgut 2001).

In the deflagration model, the burning front moves subsonically and the burning is sustained by convection. This model estimates a too large ^{54}Fe to ^{56}Fe ratio, compared to observations, and for that reason the most used model is the delayed detonation model. This model starts out with deflagration and turns into a detonation wave which provides a good prediction for the observed abundances (Vink 2011).

The fact that observations have shown recently that a variety of SNe Ia events exist, could indicate that multiple burning processes might be responsible for different SN Ia explosions (Leibundgut 2001).

2.1.2 Core collapse supernovae type II, Ib and Ic

After going through the consecutive burning stages, the most massive stars with $M \gtrsim 8M_{\odot}$ end up with an iron core of about $1.5M_{\odot}$ (Woosley & Janka 2005), and an onion like structure with a specific burning product in each of the layers: iron in the core, silicon, oxygen, neon and magnesium, carbon, helium and in the outer most layer, hydrogen (Christensen-Dalsgaard 2008). Because the iron group elements possess the highest binding energy per nucleon, no further energy can be released to sustain the star from undergoing collapse. Another means of energy loss is electron capture by the iron nuclei, turning them into neutrons. As electrons are responsible for most of the pressure in the star, the star collapses quickly into a proto-neutron star, and if the progenitor star is massive enough it collapses further into a black hole (Woosley & Janka 2005; Janka et al 2007). When the core collapses it falls nearly freely until the density reaches a value approximately two times that of the atomic nucleus ($\sim 10^{14} \text{ g cm}^{-3}$). The quick deceleration of the core and the following bounce triggers an outward going shockwave initialized by the outer layers of the star crashing down upon the forming proto-neutron star. If this shock is responsible for the expulsion of the outer layers of the star, this is called the 'prompt mechanism'. However, simulations show that the energy is not sufficient, and that the shock will stop before it leaves the outer region of the core, and it can therefore not be responsible for the explosion by itself (Janka et al 2007). Something must be adding energy to the shock and it is believed that the energy supply comes from absorption of the neutrinos emitted by the proto-neutron star, and that the shock is by those means responsible for the final supernova explosion after all, an effect called the 'delayed neutrino-heating mechanism' (Woosley & Janka 2005; Janka et al 2007; Schaeffer 2003).

However, the simulations have not yet been able to reconstruct a supernova explosion using this mechanism, which suggests that additional conditions are needed (Janka et al 2007; Vink 2011). Multi dimensional modeling shows that instabilities in the core of the supernova might hold some of the answers. This including convection, but also instabilities in the proto-neutron star accretion, which leads to slushing motions of the shock and by those means more efficient neutrino absorption. This initiates an asymmetric explosion resulting in a recoil of the neutron star in the opposite direction of the direction where most mass is ejected. Such neutron star kicks are observed for some young pulsars as we will see in a later section (section ????) and the velocities obtained by simulations are consistent with these observations. A 3D version of this model, might be able to also explain the rotation of neutron stars (Janka et al 2007).

An explosion is still only obtained when a sufficiently high value of neutrino luminosity is picked,

so some problems are still present in this solution (Janka et al 2007).

2.2 The evolution of supernova remnants

Supernova remnants (SNRs) are the aftermath of supernova explosions, where the ejected material interacts with the ambient interstellar medium (ISM). The resulting structure is of great scientific interest, as it gives an insight into the explosion mechanisms of the supernova that created the structure, cosmic ray production, and the chemical enrichment of the Universe.

Taking into account that only about 2-3 supernova explosions occur in our Galaxy every century (Vink 2011), the scientific importance of SNRs is great, as they linger behind for several hundreds of thousand years after the explosion occurred.

The type of explosion that created the SNR determines its structure, chemical composition, overall shape etc, but often it is still very difficult to determine the progenitor of a remnant. One needs to use X-ray spectroscopy in the very early stages, where the explosion is ejecta dominated and therefor still contains the fingerprints of the progenitor star (Vink 2011; McKee 1974). We will see in the following section, why this is.

The emission from the oldest SNRs is no longer originating from the ejecta directly and it is therefor difficult to trace it back to the correct progenitor system. Other indicators are needed, such as the presence of a central compact object, which points towards a core collapse origin. Furthermore, it is typical for core collapse supernovae to occur in the Galactic disk, as they are produced by short-living, massive stars, whereas the SNIa are generally found above or below the Galactic disk and associated with older stellar populations (Christensen-Dalsgaard 2008; Vink 2011). However, it is, for instance, a possibility that an observed central object is a foreground source and therefor not related to the SNR at all (Kaspi 1998). Nevertheless, the evolution in time and space of a particular SNR is dependent on it being created by a thermonuclear supernova (SNIa) or a core collapse supernova, as this determines the initial conditions for the remnant. Core collapse progenitors tend to change their surroundings before the explosion, by recurring mass loss in form of stellar winds, and the most massive progenitor stars will enter a phase of extreme mass loss, namely the Wolf-Rayet star phase, that will affect the surrounding medium severely (Van Veelen et al. 2009; Chevalier 1982). This results in the CSM being left with a density profile $\rho \propto r^{-s}$ with $s = 2$ (Chevalier 1982; Matzner & McKee 1999; Reynolds 2008) which will influence the propagation of the blast wave from the explosion. The white dwarf progenitors of SNIa events does not obviously affect their surroundings in that way, so a constant density profile of the surrounding medium ($s = 0$) is usually used (Leibundgut 2000; Dwarkadas & Chevalier 1998). It is possible though, that the binary companion could alter the CSM of the white dwarf, which would result in a not so simple density profile (Van Dyk et al 1999).

A very crude picture of the SNR evolution can be collected into four consecutive phases irrespective of their explosion type: 1) The ejecta dominated phase, where the expansion is close to free, 2) the Sedov-Taylor phase where the ISM becomes the dominant part and the ejecta profile is not taken into account, 3) the snow plough phase where the expansion is pressure driven and 4) the merging phase where the expansion becomes sub-sonic. These phases are only meant as guidelines, as the phase of a SNR is not always clearly determined and different parts of a SNR can be in different phases, because neither the remnant nor the ISM is homogeneous.

2.2.1 Phase I: The ejecta dominated phase

When a supernova ignites and the about 10^{51} ergs (Woosley & Janka 2005) of energy is released, the pressure increases in the area and the disturbed medium begins to expand accordingly (Draine & McKee 1993; McKee & Hollenbach 1980). The pressure gradient will be so large that, the ejecta will impact on the ISM with velocities of around 10000 km s^{-1} for SNIa explosions and 5000 km s^{-1} for a core collapse event, both much larger than the speed of sound in the CSM of about 10 km s^{-1} (Reynolds 2008). The velocity determined by the kinetic energy of the ejecta:

$$v = \sqrt{\frac{2E_{\text{ej}}}{M_{\text{ej}}}}, \quad (1)$$

with E_{ej} and M_{ej} being the energy and mass of the ejecta, respectively (Reynolds 2008). The supersonic behavior of the ejecta drives a shock, which is usually referred to as the supernova blast wave. The intensity of the shock is described by its Mach number, which is the shock velocity divided by the sound speed in the medium ($M = V_s/c_{\text{ISM}}$) (McKee & Hollenbach 1980). The blast wave will sweep up, compress, heat and accelerate the ISM it encounters (McKee & Hollenbach) and as long as the ejecta is dominant over the swept up material from the ISM, so that $M_{\text{ej}} \gg M_{\text{ISM}}$, the expansion of the ejecta behind the shock can be seen as almost free, following the velocity profile $v = r/t$ (Matzner & McKee 1999). The free expansion will continue through the first century of the SNR lifetime and the SNR will emit largely in the optical regime.

The further evolution of the SNR shock is determined by the distribution of material and temperature in the expanding ejecta as well as the distribution of the ambient material. The initial distribution of the ejecta is determined by the progenitor star and can be described by a power-law $\rho \propto r^{-n}$ (Chevalier 1982) with an index $n = 10 - 12$ representing a core collapse supernova (Matzner & McKee 1999), and $n = 7$ for a SNIa explosion (Colgate & McKee 1969). The appropriate indexes are established by the hydrodynamics of the supernova explosion itself. By examining the density distribution in the outer layer of several progenitors, and by approximating the motion of the blast wave through the star, (Matzner & McKee 1999) calculates the coefficients of the power law describing the density profile of the ejecta material from a core collapse supernova. Colgate & McKee showed in 1969 that the explosion of a $n = 3$ polytrope, which describes a white dwarf fairly well, will be followed by a density profile with index 7, but later results from hydrodynamic simulations, shows that an exponential gives a better fit to observations of the type Ia SNe SN1006 and Tycho (Dwarkadas & Chevalier 1998).

No matter the density distribution of the CSM, whether it has been modified by progenitor stellar winds or not, the ejecta will decelerate when the mass of the swept up ISM approaches the mass of the ejecta ($M_{\text{ISM}} \sim M_{\text{ej}}$) (Reynolds 2008). As the density of the ejecta has been lowered because of the expansion, this has triggered a so called rarefaction wave traveling inwards, lowering the pressure of the ejecta. The pressure will at some point drop below the pressure behind the outward traveling blast wave and an inward-facing compression wave is born. Because of the low sound speed in the ejecta, the wave will transform into a shock - a reverse shock that will heat up the ejecta material to high enough temperatures that thermal X-rays are emitted (McKee 1974). This is the emission that still contains the fingerprints from the progenitor star, as mentioned in the previous section.

Because the velocity of the innermost ejecta is still large, and bigger than the velocity of the reverse shock, the reverse shock will actually move outwards at first, seen from our rest frame (Ballet 2003; Reynolds 2008), but when the shocked part of the ejecta obtain a pressure higher than the pressure of the un-shocked ejecta, the reverse shock will begin to move inwards. Now

the SNR consist of two shock fronts traveling in opposite directions, separated by a contact discontinuity as depicted in Figure 1.

The contact discontinuity is subject to Rayleigh-Taylor instability, which occurs when a light

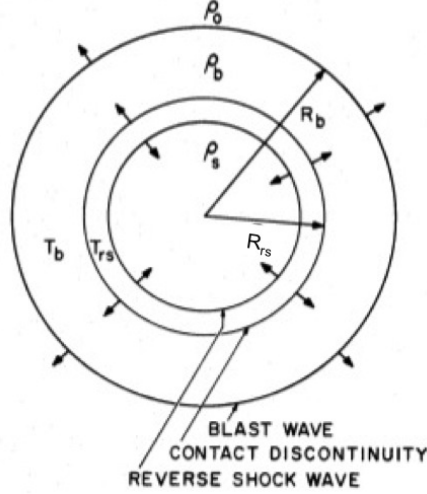


Figure 1: The structure of the SNR as it will look in the ejecta dominated phase. R_b is the blast wave radius, and its evolution is described by equation 2, R_{rs} is the reverse shock. The contact discontinuity separates the shocked interstellar medium from the shocked ejecta, where T_b is the temperature of the first, and T_{rs} is the temperature of the latter. From McKee 1974.

fluid is accelerated into a heavy fluid, because the interface between the two fluids cannot stay sharp. Small irregularities in the interface will grow bigger and result in large scale mixing of the inner and outer ejecta (Chevalier 1976; Bandiera 1984; Sharp 1984; Ballet 2003).

Assuming that the density profile of the ejecta is represented by a steep power law with $n > 5$ and that of the CSM is a shallow power law with $s < 3$, the early evolution of a core collapse SNR can be described by a self-similar solution of the form:

$$R_s \propto t^\beta, \quad (2)$$

with

$$\beta = \frac{(n-3)}{(n-s)}, \quad (3)$$

where R_s is the radius of the blast wave and β is the expansion parameter taking into account both the structure of the ejecta (index n) and the CSM (index s) (Vink 2011). If we assume that the SN Ia ejecta follows a power law density profile and not the probably more correct exponential profile from Dwarkadas & Chevalier (1998), we can use the self-similar solution for these events as well. The form of the solution does not change for different problems, and is not dependent on the timescale, because the only dependence is on the value of n and s which are constant throughout the problem.

The two-shock phase can last up to thousands of years (Reynolds 2008) and the solution can be used to describe the evolution until the reverse shock has reached the inner part of the ejecta. This happens at a time:

$$t_{ST} \approx 7 \left(\frac{M_{ej}}{10 M_\odot} \right)^{5/6} \left(\frac{E_{SN}}{10^{51} \text{ ergs}} \right)^{-1/2} \left(\frac{n_0}{1 \text{ cm}^{-3}} \right)^{-1/3} \text{ kyr}, \quad (4)$$

where n_0 is the number density of the ISM, E_{SN} is the energy of the SN and M_{ej} is the ejecta mass. At this time the SNR evolution will continue into the Sedov-Taylor phase.

2.2.2 Phase II: The Sedov-Taylor phase

When the reverse shock has reached the innermost ejecta and enough interstellar material has been swept up, so that $M_{\text{ej}} \ll M_{\text{ISM}}$, the SNR enters the Sedov-Taylor phase. Hence, when a SNR is in this phase it is no longer dominated by the ejecta, and the fingerprints of the progenitor is no longer visible (Jones & Straka 1981). This makes it difficult to determine the type of the supernova event. The evolution is still described by a self-similar solution, but here it is assumed that the explosion is an adiabatic point explosion where a finite amount of energy E is injected into a uniform medium of density ρ_0 . The structure of the supernova ejecta itself is not taken into account, and the solution does therefor not apply to the earliest evolution stage where the ejecta is dominant.

The self-similar solution was found by Sedov in 1959 using dimensional analysis where only a unique combination of the variables in the problem, which are the age t , the explosion energy E , and the density of the ambient medium ρ_0 , have the dimension needed for the shock front radius R_s (Taylor 1950):

$$R_s = S(\gamma) \left(\frac{E}{\rho_0} \right)^{1/5} t^{2/5}, \quad (5)$$

This gives an expansion parameter for the Sedov-Taylor phase as $\beta = 2/5$. S is a function of γ , the dimensionless adiabatic index describing the heat capacity ratio. The heat capacity ratio is related to the degree of freedom for a molecule by: $\gamma = 1 + \frac{2}{f}$, which means that for a monatomic gas with three degrees of freedom: $\gamma = 5/3$ and $S(\gamma) \sim 1.15$ (Reynolds 2008).

Again the self-similar solution is only dependent on parameters which are constant throughout the problem.

The velocity of the shock front V_s is accordingly:

$$V_s = \frac{dR_s}{dt} = \frac{2}{5} S(\gamma) \left(\frac{E}{\rho_0} \right)^{1/5} t^{-3/5} = \frac{2}{5} \frac{R_s}{t}, \quad (6)$$

In Figure 2 a comparison between the Sedov model and the Chevalier model can be seen, depicting the structure of a SNR. The expansion coefficient β is given in eq. 3 for the first phase and $\beta = 2/5$ from equation 4 is valid for phase II.

2.2.3 Phase I - II: The Truelove & McKee transition phase

The transition between phase I and phase II is described using a model by Truelove & McKee (1999). This model is continuous but consists of two parts, one for the ejecta dominated phase and one for the Sedov-Taylor phase, where t_{ST} describes the transition age of the remnant. The model is useful since many young SNRs are in a stage of their evolution that places them in a late ejecta dominated phase or an early Sedov-Taylor phase.

The Truelove-McKee model implements a set of characteristic length, time and mass scales, derived using dimensional analysis for the parameters given in the problem, which are the ejecta

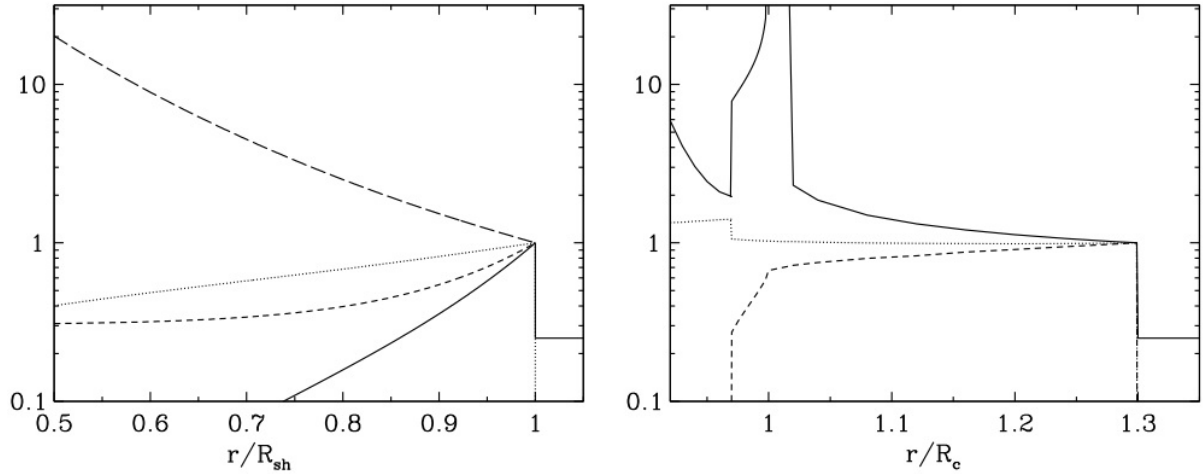


Figure 2: The structure of a SNR described by the Sedov (1959) model (left) and the Chevalier (1982) model (right) for the case where $n = 7$ and $s = 2$. The radius is given in units of the shock front radius for the Sedov model and in units of the discontinuity radius for the Chevalier model. The **solid lines** show the density, the **dotted lines** show the velocity and the **short-dashed lines** show the pressure. For the Sedov model, the **long-dashed line** shows the temperature. From Vink 2011.

energy E_{ej} , the ejecta mass M_{ej} , and CSM density ρ_0 :

$$R_{\text{ch}} = M_{\text{ej}}^{1/3} \rho_0^{-1/3}, \quad (7)$$

$$t_{\text{ch}} = E^{-1/2} M_{\text{ej}}^{5/6} \rho_0^{-1/3}, \quad (8)$$

$$M_{\text{ch}} = M_{\text{ej}}, \quad (9)$$

Instead of a similarity solution, which is used for the ejecta dominated phase and the Sedov-Taylor phase, Truelove & McKee uses a unified solution which can be utilized when the ambient pressure is non negligible.

The above equations are now only dependent on n and s and the dimensionless variables $R^* = R/R_{\text{ch}}$ and $t^* = t/t_{\text{ch}}$. For $n = 7$ and $s = 0$ (a type Ia SN) the solution tends towards a self-similar form at early and late times. This means that the Truelove & McKee solution becomes $R_b = 1.06t^{4/7}$ at times $t^* < t_{\text{ST}}$ (the ejecta dominated phase) and $R_b = (1.42t^* - 0.312)^{2/5}$ at times $t^* > t_{\text{ST}}$ (the Sedov-Taylor phase) (Truelove & McKee 1999; Vink 2011). These results are consistent with the expansion parameters given in the two previous sections.

2.2.4 Phase III and IV: The radiative snowplough phase and the merging phase

When the shock has slowed down to around a few 100 km/s (Reynolds 2008) and the remnant has grown to a size bigger than ~ 10 pc across (Ballet 2003), the adiabatic approximation no longer apply because radiation losses becomes important. This is the end of the Sedov-Taylor phase, and the beginning of the snowplough phase. Even though the material just behind the shock front cools down, the interior can still be sufficiently hot to push the cold shell of gas through the ISM (Ballet 2003). The expansion then continues as $R_s \propto t^{2/7}$ (Ballet 2003; McKee & Ostriker 1977). At this point the remnant will only be observable in radio.

When the pressure becomes ineffective, the further expansion is driven by momentum-conservation,

such that:

$$MV_s = \frac{4\pi}{3} R_s^3 \rho_0 \frac{dR_s}{dt} = \text{constant}, \quad (10)$$

where M is the mass of the swept up material from the CSM and V_s is the velocity of the forward shock. Here the expansion is continuing as $R_s \propto t^{1/4}$ (Ballet 2003) until the SNR merges with the ISM at the time where the expansion becomes subsonic.

2.3 Shock heating

The mean free path of a Galactic particle is larger than the size of a young SNR, because of the very low densities involved (Helder 2010). It is therefore surprising that shocks are indeed observed in SNRs. This means that the heating of the ISM is not mediated by collisions but through particle interaction with the electromagnetic fields arising from the collective motion of charged particles (Draine & McKee 1993; McKee & Hollenbach 1980).

A characterization of the shock can be done using that the mass, energy and momentum across the transition region separating the downstream (shocked) region from the upstream (unshocked) region are conserved, and that the jump conditions from one region to the other is determined by the Rankine-Hugoniot relations (McKee & Hollenbach 1980; Vink 2011; Reynolds 2008). For the previous mentioned case where $\gamma = 5/3$, and where the magnetic field is neglected, the relations giving the post shock pressure and temperature are (Helder 2010; McKee & Hollenbach 1980; Vink 2011; Reynolds 2008):

$$r_{\text{comp}} = \frac{\rho_d}{\rho_u} = \frac{\gamma + 1}{\gamma - 1} = 4, \quad (11)$$

$$p_d = \frac{2\rho_u v_u^2}{\gamma + 1} = \frac{3}{4} \mu_u m_p n_u v_u^2, \quad (12)$$

$$kT_d = \frac{2(\gamma - 1)}{(\gamma + 1)^2} \mu m_p v_u^2 = \frac{3}{16} \mu m_p v_u^2, \quad (13)$$

where r_{comp} is the compression ratio, n is the particle number density, the subscript u denotes the conditions upstream, and the subscript d denotes the conditions downstream. μ is the mean mass per particle in units of the proton mass m_p .

These results are dependent on there being no radiation losses and on the cosmic rays not contributing to the downstream plasma pressure, which means that the pressure is seen as purely thermal. If this is not the case, and the cosmic rays contribute with a non-thermal part, the compression ratio becomes much larger than 4 (see section 3.2 for an observational perspective). This is called the non-linear cosmic-ray acceleration case and leads to lower plasma temperatures simply because some of the energy available goes to accelerating the cosmic rays instead of heating the plasma (Vink et al 2010; Vink 2011).

Another important thing to note, is that the temperature relation in equation 12 is for the average temperature of the downstream plasma. This means that it is very important whether or not collisionless shocks result in temperature equilibrium of all particle species behind the shock. The temperature found from spectral fitting, only reveal the electron temperature and if the particles are not in equilibrium, the temperature found will not be the average. Observational evidence point towards non-equilibration being important for high Mach number shocks because collisionless shock heating is more efficient for protons and heavier ions. A minima of the temperature ratio between electrons and protons of ($T_e/T_p \sim m_e/m_p$) is reached at $v_s > 2000 \text{ km s}^{-1}$ (Ghavamian et al 2007), which means that using the electron temperature as the average for high Mach number shocks will result in an underestimation of the shock velocity (Vink 2011,

Ghavamian et al 2007). The proton temperature is a much better estimate of the average plasma temperature (Vink et al 2010).

Whether or not the particles are in temperature equilibrium behind the shock is not only dependent on Mach number, but also on magnetic field orientation, and the ratio of magnetic pressure over kinetic pressure (Bykov et al 2008).

2.4 Cosmic-ray acceleration

Galactic SNRs are considered the prime candidate source of cosmic rays with energies of up to $3 \cdot 10^{15}$ eV (Vink 2011; Ginzburg & Syrovatskij 1967) where the cosmic ray spectrum becomes slightly steeper and form a feature called "the knee". The reason for SNRs being considered a source of cosmic rays is that the cosmic ray energy density $\rho_{\text{cr}} \sim 1 \text{ eV cm}^{-3}$ (Hörandel 2008) together with the average time a cosmic ray spend in the Galaxy $\tau_{\text{esc}} \propto E^{-0.6}$ (Ballet 2003), require a particle production with the power of at least $L_{\text{cr}} = \rho_{\text{cr}} V / \tau_{\text{esc}} \approx 10^{41} \text{ erg s}^{-1}$ (Hörandel 2008; Baade & Zwicky 1934), and the only known source providing the necessary amount of power are supernovae. Taking their explosion energy and event rate into account, they provide a power of $\sim 10^{42} \text{ erg s}^{-1}$ (Vink 2011), so about 10% of this energy is needed to maintain the production of cosmic rays.

The acceleration process in supernovae was first described by Enrico Fermi (1949) and is now referred to as first-order Fermi acceleration or just diffusive acceleration. The idea is that high energy charged particles scatter back and forth across the shock front and each time they complete a cycle, that is travel from the upstream (unshocked) region to the downstream (shocked) region and back again (Hörandel 2008), they will have gained a net energy given by (Vink 2011):

$$\frac{\Delta E}{E} \approx \frac{4}{3} \frac{v_{\text{u}} - v_{\text{d}}}{c}, \quad (14)$$

where v_{u} is the upstream velocity and v_{d} is the downstream velocity.

The particles will be able to cross the shock front because it is thinner than the Larmor radius of a thermal proton, which is the radius of the circular path that the proton follows in the presence of a magnetic field (Bell 1978).

The most convincing evidence for Fermi acceleration being responsible for Galactic cosmic rays is that the resulting energy spectrum is a power law with an index close to what is observed for cosmic rays (Bell 1978). Observational evidence for particle acceleration taking place at the shock front of a SNR have recently been confirmed for the historical supernova Tycho, which we will look at in the next chapter.

2.5 Pulsar wind nebulae (PWNe)

Plerionic remnants, pulsar wind nebulae or Crab like SNRs as they are also called are strictly speaking not SNRs, as their emission does not originate directly from the SN, but rather from the neutron star left behind after a core collapse explosion. It was already predicted in the 1960's that core collapse SNe would be able to create rapidly rotating neutron stars, so called pulsars (Hoyle 1964), and that the period of rotation would increase in time, as the pulsar would lose its rotational energy (Gold 1968). The neutron star relics of SNe are indeed observed to rotate and slow down over time, and as mentioned in section 2.1.2 a 3D model of the explosion scenario including asymmetries might be able to explain the observed rapid rotation (Janka et al 2007). In 1969, the link between the spin-down of the pulsar in the Crab nebula and the observed emission was made by Gold, where he showed that the energy loss of the pulsar was approximately the same as the energy required to power the Crab nebula. This implied that the

pulsation properties of the pulsar is responsible for most of the emission seen from pulsar wind nebulae.

The theory is that the pulsar will lose rotational energy through a wind of relativistic electrons and positrons that will expand into the SN ejecta as a bubble. Because of the slow expansion of the SN ejecta, the wind will decelerate and form a termination shock. Here the charged particles are accelerated to ultra relativistic energies and because the wind is magnetized the particles will emit synchrotron emission across the electromagnetic spectrum, as described in Section 3.1.3 (Gaensler & Slane 2006; Kirk et al 2009).

The spin period P and the change in period over time $\dot{P} = dP/dt$ of a pulsar can be determined from observation of the pulsed signal (Gaensler & Slane 2006) and the spin-down-luminosity is then given by:

$$\dot{E} = -dE_{\text{rot}}/dt = 4\pi^2 I \frac{\dot{P}}{P^3}, \quad (15)$$

which is the rate at which the rotational energy from the pulsar is dissipated into the surroundings. I is the moment of inertia of the neutron star, which is usually assumed to have the value of $10^{45} \text{ g cm}^{-2}$ (Gaensler & Slane 2006). The value of \dot{E} range from $\sim 5 \times 10^{38} \text{ ergs s}^{-1}$ and down to $3 \times 10^{28} \text{ ergs s}^{-1}$.

The age and the magnetic field strength of the pulsar can be inferred from P and \dot{P} , given that certain assumptions are made. Assuming a power law deceleration model, a value of the exponent, called the braking index n can be approximated to $n = 3$ which describes the behavior according to the so called magnetic dipole model (Kirk et al 2009). The value is also in good agreement with observations (Shapiro 2008; Gaensler & Slane 2006). If this value for n is assumed and that $P_0 \ll P$, where P_0 is the initial spin period, then the characteristic age of a pulsar is given by:

$$\tau_{\text{ch}} \equiv \frac{P}{2\dot{P}} \quad (16)$$

This is often an overestimate of the true age, which indicate that the approximation of $P_0 \ll P$ is not entirely valid (Gaensler & Slane 2006).

The equatorial magnetic field strength is given by:

$$B_{\text{pulsar}} = 3.2 \times 10^{19} (P\dot{P})^{1/2} \text{ G} \quad (17)$$

The magnetic field strength B_{pulsar} range from $1 \times 10^{12} \text{ G}$ to $5 \times 10^{13} \text{ G}$ (Gaensler & Slane 2006), although there are extreme cases, such as millisecond pulsars with a weak magnetic field (also called recycled pulsars, for reasons we will touch upon in the following section) and magnetars with a strong magnetic field (around 5 – 10% of the pulsar population are magnetars) (Vink 2011).

The magnetized wind around a pulsar is generally described by its magnetization parameter σ which is given by the ratio between the Poynting flux and the particle flux:

$$\sigma \equiv \frac{F_{E \times B}}{F_{\text{particle}}} = \frac{B^2}{4\pi\rho\gamma c^2}, \quad (18)$$

where B is the magnetic field as given above, ρ is the mass density of particles and γ is the Lorentz factor in the wind ($\gamma = 1/\sqrt{1 - (v^2/c^2)}$). This parameter is an expression of how effectively the magnetic field affects the particle trajectory.

The further evolution of the pulsar and its emission is influenced by its surroundings, especially because it is born in the center of a SNR.

2.5.1 Pulsar wind nebula evolution

We have already looked at the different phases of evolution of a SNR, but in the case where a PWN is present, it will interact with the surrounding SN ejecta, and the evolution becomes more complex.

Young pulsars

A young PWN is expanding in the unshocked ejecta of the SN, which corresponds to the earliest phase of the SNR evolution, where the ejecta is almost freely expanding. As mentioned earlier, asymmetries in the explosion can give the pulsar a random space velocity, which often lies in the range $100 - 1000 \text{ km s}^{-1}$ (van der Swaluw 2003). However, the pulsar will at early times be located near the center of the SNR as it has not had time to move away from its birth site and its kick velocity is usually much smaller than the velocity of the remnant expansion (van der Swaluw et al 2003).

Because the pressure of the ejecta surrounding the PWN is low, the PWN will expand supersonically and therefore drive a shock in the same way as for the forward SNR shock. If a spherical symmetry is assumed, the expansion of the PWN will follow the equation (Gaensler & Slane 2006):

$$R_{\text{PWN}} \equiv 1.5 \dot{E}_0^{1/5} E_{\text{SN}}^{3/10} M_{\text{ej}}^{-1/2} t^{6/5} \quad (19)$$

where R_{PWN} is the radius of the PWN shock at time t . M_{ej} is the ejecta mass of the SN and E_{SN} is the energy of the SN explosion.

The SNR will after a time t_{ST} (given in Equation 4) reach the Sedov-Taylor phase where the swept up ISM mass is approximately the same as the ejecta mass. Leading up to this time a reverse shock will move inward through the ejecta, heating it up along the way, and in the presence of a PWN, the reverse shock will collide with the PWN termination shock, typically a few thousands years after the SN explosion (Gaensler & Slane 2006). The collision gives rise to Rayleigh-Taylor instabilities which leads to mixing of the thermal and non-thermal material. The magnetic field of the PWN will increase and lead to severe synchrotron burn-off of the highest energy electrons (Bucciantini et al. 2003; Reynolds 2009). When the reverse shock hits the PWN it will be crushed, and as the SNR is most likely asymmetric because of the inhomogeneities of the ISM, such that different parts of the SNR will be in different evolutionary phases at the same time, the reverse shock will also reach different sides of the PWN at different times. This means that the PWN will be displaced from the pulsar, leaving behind a relic nebula which is still detectable in radio (Safi-Harb 2012). As the reverse shock hits and compresses the PWN, the internal pressure increases and the nebula will respond by a fast expansion. This oscillating behavior will continue on a time scale of a few thousand years. In the very rare case where the SNR, and PWN are symmetric, the PWN will not be displaced from the pulsar, and the oscillating behavior of the nebula will eventually wear off and settle into expansion once more. This time the expansion is in the hot ejecta heated by the reverse shock, and the expansion therefor continues subsonically (Gaensler & Slane 2006).

The fact that one needs to take into account both the random velocity of the pulsar caused by the asymmetric SN explosion, together with the asymmetries of the reverse shock interaction with the PWN termination shock, leads to complicated three-dimensional models of the PWN evolution inside a SNR (Gaensler & Slane 2006).

Old pulsars

When the SNR reaches the Sedov-Taylor phase, the original PWN has already become a relic and the displaced pulsar has had time to create a new much smaller PWN at its current posi-

tion. The relic PWN will at some point reach pressure equilibrium with its surroundings and the expansion will cease.

The pulsar on the other hand will continue to move away from the center of the SNR, and because the sound speed in the shocked ejecta drops towards the edge of the SNR, the pulsar will become supersonic and drive a bow-shock on its way through the remnant interior. The transition into a bow-shock nebula takes place when the pulsar has moved $\sim 68\%$ of the distance between the center and the forward shock of the Sedov-Taylor SNR. The pulsar will usually cross the SNR edge after ~ 40000 years. When a pulsar has left its parent SNR, it will move supersonically through the ISM while it drives a bow-shock nebula with a large Mach number ($M \gg 1$). When the pulsar has moved clear of its remnant, its \dot{E} drops and at some point its energy output is not high enough to drive a synchrotron nebula. Some old pulsars in binary systems will evolve in a slightly different way, since they can be spun up by accretion from their companion star. This is called recycling of the pulsar, and this leads to a pulsar with sufficient energy to drive a bow-shock nebula despite its old age. The morphology of the bow-shock nebula will be reviewed in Section 3.4.

3 Supernova remnants: observational characteristics

SNRs are characterized based on their appearance on the sky or based on their spectra (Vink 2011). There are several ways of distinguishing different types, but here I will focus on the morphological characteristics. Based on that, they can be divided into three groups: shells, plerions (pulsar wind nebulae), and composites, all of which we will review in this Chapter.

3.1 Emission processes in supernova remnants

The main difference between the hot ($kT_e > 10^6 K$) SNR plasmas and other hot astrophysical plasmas is that SNR plasmas are often out of ionization equilibrium. This is termed Non-Equilibrium Ionization (or NEI) plasmas and is a result of the very low densities. Because of the swift changes in temperature in SNR plasmas, brought about by the shock, the plasma need to adjust the ionization balance quickly, but because of the low densities resulting in very few ionizing collisions, it takes too long to adjust to the new temperature (Vink 2011; Kaastra et al 2008). This means that the number of atoms in a specific ionization state is lower for a NEI plasma at a specific temperature, than for other plasmas. Therefore, the temperature of a NEI plasma will often be lower than what the ionization indicates (Vink 2011).

3.1.1 Thermal continuum emission

That emission is thermal, means that the particles creating it has a Maxwellian energy distribution. Three different emission processes contribute to the collective thermal continuum emission in SNR X-ray spectra: Bremsstrahlung (free-free process), recombination emission (free-bound process) and two-photon emission (bound-bound process) (Kaastra et al 2008; Mewe 1997; Vink 2001).

Bremsstrahlung is produced when a free plasma electron collides with an ion. After the collision the electron carries on as a free particle, but with less kinetic energy. The lost electron energy is emitted as a bremsstrahlung photon and the emissivity of the process can be written as (Vink 2011; Melia 2009):

$$\epsilon_{\text{ff}} = 6.8 \times 10^{-38} g_{\text{ff}}(T_e) T_e^{-1/2} \exp\left(-\frac{h\nu}{kT_e}\right) n_e \sum_i n_i Z_i^2 \text{ erg s}^{-1} \text{ cm}^{-3} \text{ Hz}^{-1} \quad (20)$$

where i indicates the ion species and eZ_i is the charge of the ion. The Gaunt factor g_{ff} is dependent on the ratio between the maximum value of the impact parameter b (which is the distance of closest approach between the electron and the ion) and the minimum value of the impact parameter b . For most astrophysical thermal plasmas $g_{\text{ff}} \approx 1$ (Vink 2011; Melia 2009; Longair 1999).

It can be seen from the equation, that metal-rich plasmas will have higher emissivity, because of the Z^2 dependence. This is because the ionized metals contribute with a larger number of free electrons, which means a more frequent encounter with ions (Vink 2011).

The Bremsstrahlung spectrum is flat for photon energies $\ll kT$ and has a characteristic roll-over at $h\nu \sim kT$ whereafter it starts declining exponentially (see Figure 3). This means that, once the photon energy corresponding to the roll-over has been determined, the temperature of the emitting plasma is directly given (Melia 2009).

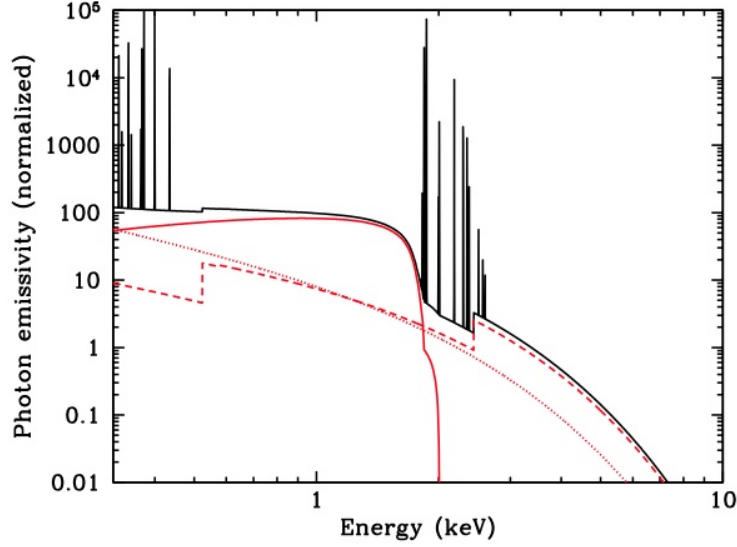


Figure 3: The total thermal continuum spectrum is shown as the **black solid line**, the contribution from bremsstrahlung, recombination emission and two-photon emission are shown as the **dotted line**, **dashed line**, and the **red solid line**, respectively. The emission spikes caused by cascade emission from electrons with an energy just below the edge energy are shown for the L- and K-shell. The spectrum is for a pure silicon NEI plasma with $kT_e = 1$ keV and $n_e t = 5 \times 10^{10} \text{ cm}^{-3} \text{ s}$. From Vink 2011

Recombination emission arises as a free electron is captured by an ion and a photon is emitted, which is the reverse of photoionization where a photon kicks an electron out of its shell (Kaastra et al 2008). The photon will have an energy given by $h\nu_n = E_e + \chi_n$ where E_e is the energy of the free electron and χ_n is the ionization potential of an electron in the energy level n . The emissivity for a specific energy level is given by:

$$\epsilon_{\text{fb}} = \left(\frac{2}{\pi}\right)^{1/2} n_e n_{z+1} \frac{g_i}{g_{i+1}} c \sigma(h\nu) \left(\frac{h\nu}{\chi_n}\right)^3 \left(\frac{\chi_n^2}{m_e c^2 kT}\right)^{3/2} \exp\left(-\frac{(h\nu - \chi_n)}{kT_e}\right) \text{ erg s}^{-1} \text{ cm}^{-3} \text{ Hz}^{-1}, \quad (21)$$

where n_{z+1} is the density of the ion before recombination, n_z is the density of the recombined ion, $\sigma(h\nu)$ is the photoionization cross section of the recombined ion. The statistical weights of the ion before and after recombination, g_{i+1} and g_i , are roughly equal to the number of substates with the same energy. (Liedahl 1997; Vink 2011; Kaastra et al 2008).

The spectrum exhibits sharp edges at the photoionization energy of the different energy levels (see Figure 3). An edge arises because of the minimum energy required in order for the recombination of a specific energy level to take place, for a specific ion. This means that there will be a quick rise in emission at that energy and the emission will fall off in a way that resembles the bremsstrahlung continuum, determined by the Maxwellian velocity distribution of the free electrons together with the cross section that goes as $\sigma(h\nu) \propto v^{-3}$. The sharp spikes of emission will arise because of the cascade emission that is emitted when an electron travels from the outer most shell to the recombination shell which will happen for the electrons that do not fulfill the energy criteria for the recombination edge. This is seen in the spectra of overionized plasma.

Recombination emission is not dominant in young SNRs, as the plasma has recently been heated by the shock, which means that there are only few highly ionized ions present, which are able to recombine and produce emission (Liedahl 1997).

Two photon emission is most important for hydrogen-like and helium-like ions. An electron from the $1s$ state is excited to the $2s$ state and cannot decay back to the $1s$ state, because $\Delta l = 0$. Such a transition is forbidden according to the selection rules (Kaastra et al 2008). Instead it can be excited even further by collision with another electron and then de-excite all the way to the $1s$ state again. This is, however, very unlikely due to the low densities, and another possibility is much more likely. In this scenario, the electron de-excites from the $2s$ state to the $1s$ state by emitting two photons, where the associated energy has been divided between them evenly (Kaastra et al 2008; Foot 2008; Vink 2011).

The spectrum can be seen in Figure 3.

3.1.2 Thermal line emission

Line emission is produced as a consecutive process to excitation. Several process can result in excitation of an atom or ion, but the dominant process in SNRs is electron-ion collisions. After an ion has been excited, collisional excitations, de-excitations, and ionizations can be neglected, because of the low density. A characteristic type of line emission for NEI plasma is the consequences of inner shell ionization. In this kind of ionization, an electron from one of the inner shells is removed, whereas the higher level shells are still filled. The ion can then de-excite by letting the outer electrons jump down to fill the hole, and use the energy from that transition to excite the ion further. This is called Auger transitions.

Another possibility is that the ion adjusts radiatively without further excitation which is called fluorescence.

The power of a specific line is given by (Kaastra 2008, Mewe 1997):

$$P_{ij} = A_{ij}n_j, \quad (22)$$

where A_{ij} is the probability of a transition from the excited state j to a lower energy level i and n_j is the number density of ions in the excited state j .

Not all transitions are allowed. Only the ones that fulfill the selection rules are allowed, which are the ones where the spin of the electron is not changed during the transition ($\Delta s = 0$) and where the electron is not staying in the same orbital ($\Delta l = \pm 1$). There are of course exceptions, and forbidden lines are observed (Foot 2008).

Line emission in SNRs can also be caused by radioactivity. The most important radioactive element for the SNR evolution is ^{56}Ni , because it provides the main energy for expansion of the ejecta during the first year after the supernova explosion. ^{56}Ni has a decay time of 8.8 days, whereafter it decays into ^{56}Co and then ^{56}Fe . Most of the ^{56}Fe is produced by SN type Ia, which amounts to around 10 times as much as the core collapse supernovae ($\sim 0.6 M_{\odot}$ per explosion, which is why they have strong Fe-L-shell emission that is often used as a characterization tool.

3.1.3 Non-thermal emission

Non-thermal emission is produced by electrons that have a non-thermal velocity distribution which is often nicely approximated by a power law. The most common type of non-thermal emission is synchrotron emission.

Synchrotron radiation is emitted when charged particles travel at relativistic velocities in the vicinity of magnetic fields. A relativistic electron will, in presence of a constant magnetic field, experience the effect of the Lorentz force, which results in the electron accelerating and

moving along a circular path in a plane perpendicular to the magnetic field (Als-Nielsen & McMorro 2011). The electron will emit continuous radiation, but the maximum emission is reached at the critical frequency ν_c :

$$\nu_c = 1.8 \times 10^{18} B_{\perp} \left(\frac{E}{1 \text{ erg}} \right)^2 \text{ Hz}, \quad (23)$$

where B_{\perp} is the magnetic field component perpendicular to the motion of the electron. The intensity spectrum of synchrotron emission from one electron is described by $\epsilon_{\text{SR}} \propto \nu^{1/2} e^{-\nu/\nu_c}$. This means that at low frequencies $\nu \ll \nu_c$, the spectrum goes as $\epsilon_{\text{SR}} \propto \nu^{1/3}$ and for frequencies $\nu \gg \nu_c$ the exponential cut-off dominates the spectrum. Synchrotron radiation is solely responsible for the radio emission from SNRs and will also contribute up to a few tens of keV as we will see later (Reynolds 2008).

Non-thermal bremsstrahlung can also contribute to the integrated spectrum, produced by bremsstrahlung or inverse Compton scattering of lower energy electrons (Vink 2011). Inverse Compton scattering is important in the case of SNRs in the GeV-TeV range. This means that many SNRs are expected to have counterparts in γ -rays, which is also observed with for instance H.E.S.S. (High Energy Stereoscopic System) (Aharonian et al 2006). Non-thermal bremsstrahlung is a candidate for continuum emission in SNRs, but has not yet been identified since the emissivity is expected to be low (Vink 2011).

3.2 Shell type remnants

When the SN blast wave moves through the ISM it creates a shell of heated, swept up material as described in section 2.2. The reverse shock wave will move inwards and heat up the ejecta. The resulting shell of hot material is observed as a ring and not a blob of emission, because of the greater amount of hot gas in our line of sight at the edges than through the middle of the remnant, which is called limb brightening. A radial profile of such objects, will therefore show an increase in brightness with increasing radius. The shell region is a source of both X-ray continuum emission and line emission from ionized elements, and the spectral characteristics of the regions can tell us about the supernova nucleosynthesis and about the initial density profile of the supernova (Decourchelle 2004). The smoothness or irregularity of the shell emission can be an indicator of the ISM being inhomogeneous. That is, the ISM is denser in the areas where the shell is brighter (Decourchelle 2004).

In the case of a very bright remnant, the shell can be resolved in such great detail, that it is possible to distinguish the different regions and the contact discontinuity separating them. It is then very useful to be able to determine the ratio between the blast wave radius and the reverse shock radius $R_b/R_r = l$ (Truelove & McKee 1999), as this can be an indicator of the evolutionary state of the remnant (Gotthelf 2001). l is called the lead factor, indicating with how much the blast wave shock front leads the reverse shock.

The location of the forward and reverse shocks can be determined from a surface brightness profile as it is for instance done in Cassiopeia A (Gotthelf et al 2001), where the forward shock and the reverse shock are indicated by two separate peaks in the profile. From this, Gotthelf et al (2001) derive a lead factor value l of $\sim 3 : 2$, which indicate that the reverse shock and the blast wave shock are quite close to each other. And as the Sedov-Taylor phase will set in at approximately the time where the reverse shock reaches the core of the ejecta, and maybe even a little bit sooner, it can be concluded that Cas A must be in the transition phase between the

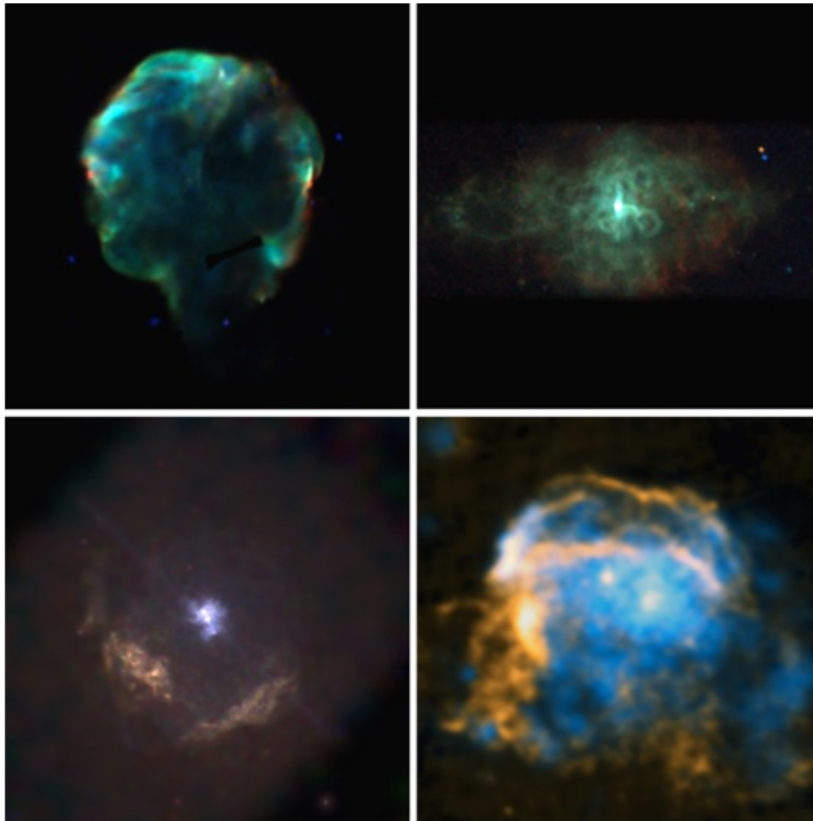


Figure 4: This Figure illustrates the morphology of the different SNR types. *Top left:* The Cygnus Loop, which is a shell remnant. The observation is from ROSAT with the colors red, green, blue, representing the energies ($\sim 0.1 - 0.4$ keV), ($\sim 0.5 - 1.2$ keV), and ($\sim 1.2 - 2.2$ keV) respectively. *Top right:* The plerion/pulsar wind nebula 3C58 observed with Chandra. *Bottom left:* The plerionic composite remnant Kes 75. The red, green, and blue colors represent ($1 - 1.7$ keV), ($1.7 - 2.5$ keV), and ($2.5 - 5$ keV), respectively. *Bottom right:* The thermal composite/mixed-morphology remnant W28 observed in X-ray with ROSAT (blue color) and in radio with the VLA (orange color). (Image credit: Vink 2011)

ejecta dominated phase and the Sedov-taylor phase (Gotthelf 2001; Truelove & McKee).

Famous examples of shell remnants are Cassiopeia A (G111.7-02.1), which is a core collapse SNR, Tycho (G120.1+01.4) and Kepler (G004.5+06.8) which are both the relics of a type Ia SN (Green 2009; Ferrand et al 2012).

Probably the most exciting thing about remnant shells, is that observations of the forward shock and the precursor can reveal the presence of efficient particle acceleration as mentioned in section 2.4. When particle acceleration is efficient in a SNR shock, the interaction region becomes very thin (Decourchelle 2004; Decourchelle et al 2000), which is equivalent to the compression ratio being large, as mentioned in section 2.3. This is for instance the case for the SNR Tycho.

3.3 Pulsar wind nebulae - young pulsars

The probably most studied PWN, the Crab nebula, shows an easily detectable X-ray morphology consisting of a torus structure and two jet-like features (see Figure 5). The particles that are accelerated at the PWN termination shock are believed to form the torus shape around the pulsar equator because of the pulsar rotation. The jet-like features are formed because of collimation in the wind outflow along the axis of rotation. An observation in X-rays can therefor

be an indicator of the orientation of the pulsar (Gaensler & Slane 2006; Kirk et al 2009). Even though the Crab nebula is probably the best studied PWN, it is still far from fully understood, since no SNR shell is observed. This is actually quite common, since out of the ~ 90 Galactic SNRs that contain a PWN, about 30 of those have no detected SNR shell (Safi-Harb 2012). These can be referred to as "naked" PWNe.

In general, and not taken into account whether a shell is present or not, a PWN is characterized by an increase in brightness towards the center, which makes them easily distinguishable from shell type remnants, which show a limb-brightened morphology. The spectroscopic characteristics of a PWN is dominated by non-thermal synchrotron emission observable from radio to X-ray energies (Safi-Harb 2012).

PWNe are observed to have an X-ray size which is smaller than their radio and optical size, due to the fact that higher energy emitting synchrotron electrons have shorter lifetimes (X-ray emitting electrons have a lifetime of only a few years) (Kirk et al 2009; Slane et al 2000). This means that the electrons that emit most of their energy at a high ν_c (see Section 3.1.3, Equation 23) will not be able to travel as far as the electrons emitting most of their energy at lower ν_c (Slane et al 2000). This effect is called synchrotron burn-off or synchrotron losses and makes high energy observations of PWNe very important, since the high energy photons probe the acceleration venues. It turns out that the acceleration takes place at the termination shock close to the pulsar, as is observed in for instance the Crab nebula. Spectral softening is therefore expected with increasing radius from the pulsar, given that the synchrotron lifetime is shorter than the age of the pulsar which is in turn decided by the strength of the magnetic field B (Kirk et al 2009; Slane 2000) as given in the equation (Bamba et al 2010):

$$t_{\text{synch}} = 2 \left(\frac{B}{10\mu\text{G}} \right)^{-3/2} \left(\frac{E_{\text{synch}}}{1\text{keV}} \right)^{-1/2} \text{ kyr}, \quad (24)$$

where E_{synch} is the peak energy of the electron synchrotron emission.

The spectrum of a PWN shows a flat spectral index in the radio regime, with a spectral index in the range of $\alpha = -0.3 - 0$ ($S_\nu \propto \nu^\alpha$), and a much steeper photon index in X-rays of $\Gamma = \alpha + 1 \sim 2$ ($N_E \propto E^{-\Gamma}$) (Gaensler & Slane 2006; Safi-Harb 2012; Combi et al 2006; Kirk et al 2009). The reason for this spectral steepening is not understood, but might be a product of a spectral break in the injected electron spectrum (Kirk et al 2009; Gaensler & Slane 2006), synchrotron losses, lack of effective acceleration at high energies or other unknown effects (Combi et al 2005).

Recent gamma ray observations have revealed gamma ray counterparts for several known PWNe (Bamba et al 2010, Aharonian et al 2009) which suggests that PWNe might also be important sources of cosmic-ray acceleration.

As a PWN expands inside its host SNR, Rayleigh-Taylor instabilities will form at the boundary between the fast moving synchrotron nebula and the slower moving unshocked SN ejecta. This interaction will form dense wispy structures that will be photoionized by the synchrotron emission, and emit radiative recombination lines observable at optical and ultraviolet wavelengths. These structures will compress the surrounding magnetic field and thereby enhance the synchrotron emission, which will be observable at radio wavelengths (Gaensler & Slane 2006).

It is important to note that not all core collapse supernovae becomes plerionic remnants. That a neutron star is present in the center of a remnant, does not necessarily mean that a pulsar wind nebula will form (Vink 2011). As seen from the previous section, core collapse supernovae can result in a simple shell-type remnant.

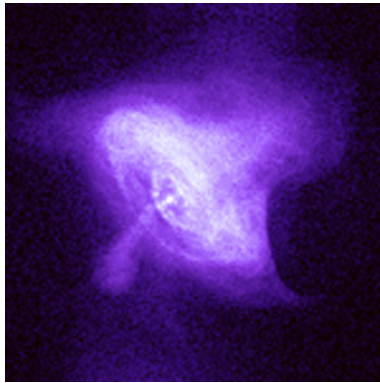


Figure 5: X-ray emission from the Crab nebula as observed with Chandra. The torus and jet-like structures are clearly distinguishable. The Crab pulsar resides in the center of the torus shape. (Image credit: Chandra web site gallery <http://chandra.harvard.edu/photo/category.html>)

3.4 Bow-shock nebulae - evolved pulsars

Only pulsars younger than ~ 20000 yr tend to form a Crab like PWN, whereas older pulsars that have a high spatial velocity and are on the way to, or already have left their parent SNR will power a bow-shock nebula (van der Swaluw et al 2003). A pulsar driving a bow-shock nebula will have a cometary appearance at both X-ray and radio wavelengths with the radio emission trailing behind reflecting the difference in synchrotron lifetime for X-ray and radio emitting electrons. The "tail" emission will fade into the background further away from the pulsar (Gaensler et al 2004).

From hydrodynamical simulations, it is seen that the wind from the pulsar will terminate in the same way as for a young PWN resulting in a double-shock structure, a forward shock where the encountered ISM is heated, and a termination shock (see Figure 6) (Bucciantini 2002). The pulsar is marked with an asterisk in the Figure and the region surrounding it contains the free unshocked wind which is observable in Crab-like PWNe as a dark cavity surrounding the pulsar (see Figure 5). This has not yet been seen in bow-shock nebulae (Gaensler et al 2004). A termination shock is formed where the energy density of the free wind balances the external pressure in the same way as for Crab-like PWNe, but for bow-shock pulsars the termination shock is elongated and have therefor a larger radius behind the pulsar than in front, as can be seen from Figure 6. At the termination shock, relativistic particles emit synchrotron emission. The particles that are shocked at the termination shock behind the pulsar are confined to a cylindrical narrow region trailing behind the pulsar, the rest are spread out and creates a larger and broader structure (Gaensler et al 2004, Bucciantini 2002)). The material in the narrow region typically moves subsonic, whereas the material in the broader region moves supersonic (Gaensler et al 2004). A contact discontinuity separates the shocked wind from the shocked ISM, and if the pulsar is traveling through ISM and not its SNR host, the forward shock of the PWN will be visible in $H\alpha$ emission. This means that observations in the optical can reveal bow-shocks around moving pulsars (Bucciantini 2002). The structure described by the hydrodynamical simulations fits well with observations as seen in the right panel of Figure 6.

Comparing the hydrodynamical simulation model and observations tells us that the brightest part of the X-ray emission corresponds to the termination shock, whereas the fainter, more diffuse and extended emission corresponds to the shocked wind (Gaensler & Slane 2006; Bucciantini 2002). If high resolution imaging data is available, it is possible to determine the ratio between the radius of the termination shock in front and behind the pulsar, which is approximately equal

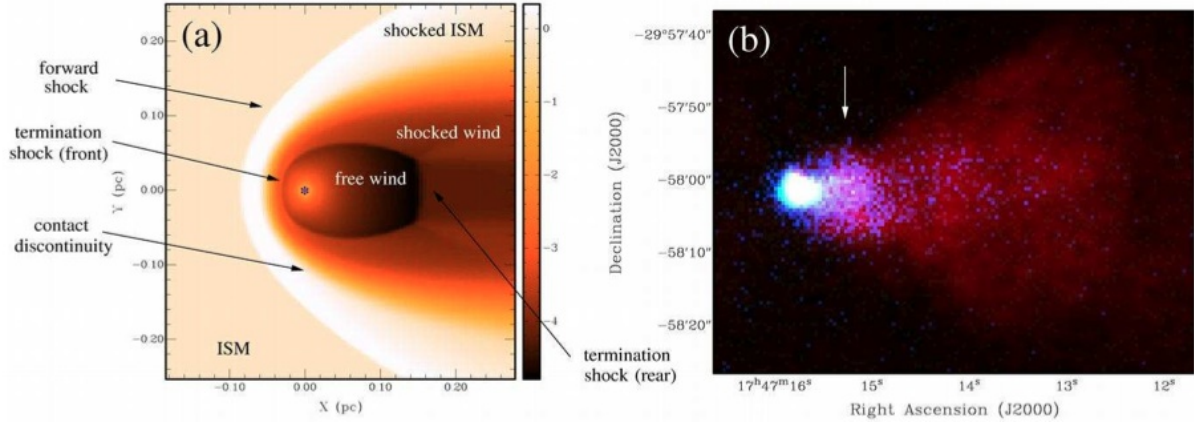


Figure 6: The left panel shows the result of the hydrodynamical simulation described in the text. The right panel shows an image of "the Mouse" which is a bow shock pulsar. (blue) is emission in the X-ray regime obtained with Chandra, (red) is radio emission from the VLA. The white arrow points to where the termination shock is thought to be located. From Gaensler & Slane

to the Mach number M of the pulsar. A pulsar traveling supersonically through its parent SNR will generally have a Mach number of $M \sim 1 - 3$ (van der Swaluw et al 2003; Gaensler & Slane 2006; Gaensler et al 2004), whereas for pulsars traveling through the ISM, the Mach number will reach a limit of $M \sim 5 - 6$ (Gaensler & Slane 2006; Gaensler et al 2004).

The spectra of bow-shock PWN is expected to show the same characteristics as a static PWN. That is, a non-thermal nature with softening of the spectrum with increasing distance from the pulsar (Gaensler et al 2004). The spectrum is expected to be correlated with the spin-down luminosity, meaning that pulsars with lower \dot{E} has a flatter photon index (Gaensler et al 2004).

3.5 Composite remnants

A composite remnant consists of a shell-like structure and a centrally filled structure, depending on which part of the electromagnetic spectrum they are observed in. Two types of composite remnants are recognized: plerionic composites and thermal composites.

3.5.1 Plerionic composites

This SNR type has a shell type morphology in radio, and is centrally filled in X-ray with the central part being a PWN. In very early stages, we expect to see a SNR that is expanding very fast, a PWN which is symmetric and positioned in the center of the SNR, and a pulsar near the center of the PWN as described in Section 2.5.1. This type of source is very complex since the SNR part of the source evolves as described in Section 2.2 and the PWN evolves as described in Section 2.5.1.

Many remnants are classified as plerionic composite remnants based on their shell shape in radio and their non-thermal centrally filled X-ray emission, even though no pulsations have been detected from the supposed pulsar. Even though the pulsar has not been directly observed, some quantities can be determined based on its X-ray emission. Because the X-ray nebula is directly linked to the pulsar properties as we saw in Section 2.5, a lot can be inferred from

observations of the nebula. Several authors have found relations linking the X-ray luminosity of the pulsar or PWN to the spin-down luminosity of the pulsar (Possenti et al 2002; Seward & Wang 1988; Becker & Trümper 1997).

The relation found by Seward & Wang (1988) is based on the 0.2-4.0keV luminosity of 8 different pulsars and their nebulae and the observed rotational period. The relation is given by $\log L_X = 1.39 \log \dot{E} - 16.6$. Possenti et al (2002) did a similar investigation but using the energy range 2-10 keV which was meant to reduce the fit uncertainties due to absorption and in order to be able to ignore the emission component arising from the cooling of the neutron star. Other than doing a combined study of a much larger sample (39 pulsars) than what was used in Seward & Wang study, they also divide them into groups based on their type and obtain fits for each type. The combined fit reveals a relation given as: $\log L_X = 1.34 \dot{E} - 15.34$.

3.5.2 Thermal composites/Mixed morphology remnants

Mixed morphology remnants are a relatively new class of remnants that are only poorly understood. These objects are characterized by centrally dominating thermal X-ray emission and a shell-like appearance in radio (Vink 2011; Combi et al 2008). Besides these most basic characteristics, they tend to have other things in common as well. Most of them are quite old (≥ 20000 yr), and have therefore reached an evolutionary stage similar to the snow-plough phase (see Section 2.2.4). This is not a rule, though, since the mixed-morphology remnant W49 has an age of 1000 – 4000 yr.

Several models try to explain the X-ray morphology of mixed-morphology remnants. The most renowned explanation is that of clouds surviving the interaction with the remnant forward shock, and subsequently starts to evaporate in the center of the remnant (White & Long 1991). Another model propose that the remnant forwards shock has decelerated and the shell cooled so that it does not emit X-rays (Cox et al 1999).

Thermal composites generally have homogenous X-ray plasma temperatures which is due to thermal conduction (Cui & Cox 1992) and turbulent mixing (Shelton et al 2004) and because of the evolved state of the remnant, it will have reached pressure equilibrium, leading to rather homogeneous densities as well (Vink 2011). Furthermore, many of the remnants also have metal-rich plasma in their interior, and as metal-rich plasma emit more X-ray emission, this increase the contrast between the metal-rich X-ray emitting interior and the cool radio shell. Many thermal-composite SNRs are close to ionization equilibrium, and some also show radiative recombination continua emission in their spectra, which is a sign of over ionization (Vink 2011).

4 The Chandra Norma region survey

The Chandra X-ray observatory was launched in 1999 into a highly elliptical orbit with an apogee height of ~ 145000 km and a perigee height of ~ 4000 km. The telescope was launched in order to provide great improvement on spatial and spectral resolution over previous X-ray missions (Chandra X-ray Center 2012).

The optics module (or the High Resolution Mirror Assembly, HRMA) consists of four nested pairs of grazing-incidence mirrors arranged in a Wolter-1 design, that is a paraboloid part and a hyperboloid part. The mirrors are made from polished Zerodur glass coated with iridium and the optical assembly results in a focal length of 10 m (Chandra X-ray Center 2012). Baffles are mounted inside the optical bench separating the HRMA from the detectors, and their key purpose is to prevent low energy electrons and stray light from reaching the focal plane and washing out the image (Chandra X-ray Center 2012).

The Science Instrument Module (SIM) contains the focal instruments, the ACIS and the HRC. In this thesis we will focus on the ACIS instrument, since all observations are done with the ACIS-I turned on. The best spectral resolution is obtained with the High Energy Transmission Grating (HETG) which has been optimized for high-resolution spectroscopy of bright sources.

The ACIS instrument contains two CCD arrays. The first one is a wide field imager (ACIS-I) with a field of view (FOV) of $\sim 16 \times 16$ arcmin provided by an array of 4 chips numbered I0-I3. The second one consists of 6 CCDs in a linear array (ACIS-S) which is optimized for grating observations providing high resolution spectroscopy for bright objects. The ACIS-S3 chip provides the best energy resolution of the ACIS system (Chandra X-ray Center 2012). It is common to have both the ACIS-I array and the S2 and S3 chips turned on for observations where imaging is the main goal, since this provides the best grounds for chance observations (Chandra X-ray Center 2012).

The CCDs have a pixel size of $0.492 \text{ arcsec} \pm 0.0001 \text{ arcsec}$ providing a high spatial resolution compared to previous X-ray missions. They are made of primarily silicon, and photoelectric absorption of an X-ray photon will release a proportional amount of electrons and good spectral resolution depends on how accurately the instrument can determine the charge resulting from one photon.

An important part of the spacecraft system is the Pointing Control and Aspect Determination (PCAD) which controls the dithering and pointing of the telescope. Dither is added to each observation in order to spread out the image over many pixels, so that sharp pixel-to-pixel variations are minimized and to provide some exposure in the chip gaps (Chandra X-ray Center 2012). The dither pattern spans 16 arcsec peak to peak for ACIS observations (Chandra X-ray Center 2012).

4.1 The extended sources of the Norma survey

An X-ray survey of a 2° by 0.8° region of the Norma spiral arm was done during summer 2011. 27 Chandra observations, each of ~ 20 ks duration were performed with the Chandra telescope for an in depth study of the region (private conversation with John Tomsick). An image of the Milky Way picturing the extend of the Norma spiral arm can be seen in Figure 8, and a mosaic image of the Chandra Norma survey observations can be seen in Figure 9.

The primary goal of the survey was to find new High-Mass X-ray Binaries (HMXBs) in order to study their evolution. The Norma region was chosen because the hard X-ray imaging of the Galactic plane done by the INTErnational Gamma-Ray Astrophysics Laboratory (INTEGRAL)

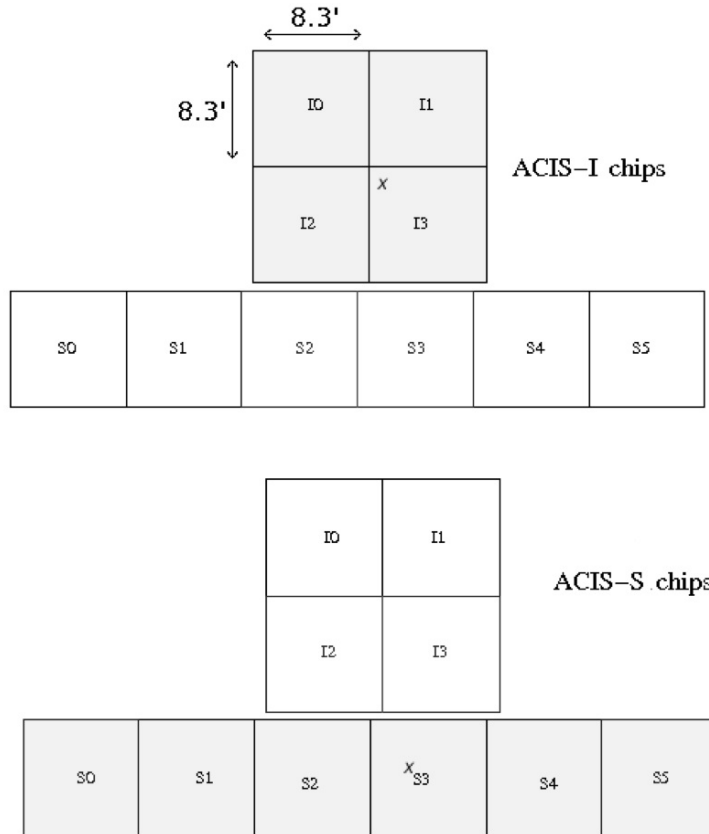


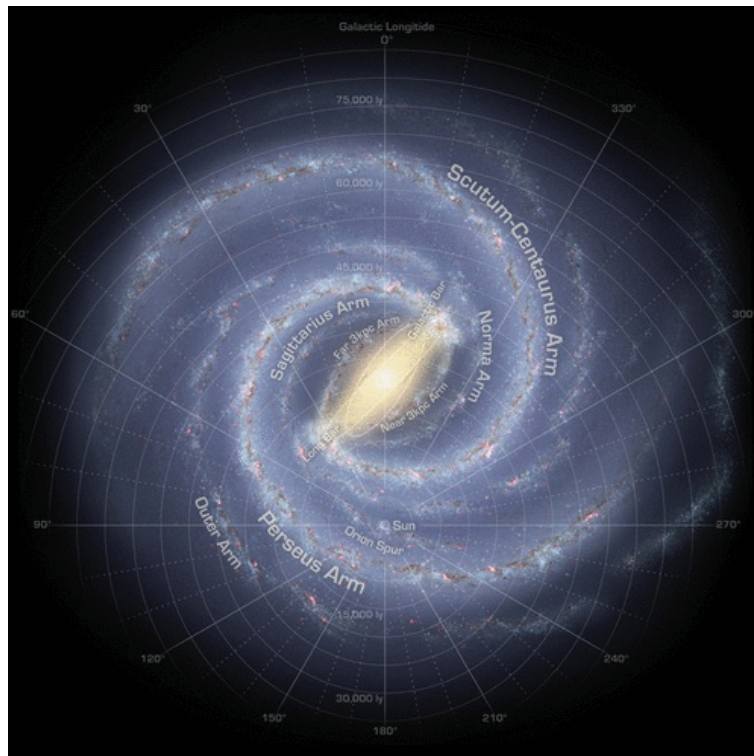
Figure 7: An illustration of the ACIS instrument. ACIS-I with chips I0-I3 and ACIS-S with chips S0-S5. The small cross marks indicate the aimpoints of the telescope for each instrument. From <http://cxc.harvard.edu/cal/Acis/index.html>

revealed that the Norma region contains the largest amount of hard X-ray sources, after the Galactic center (Fornasini et al 2012). Around 1500 sources were found in this survey and a catalog of these sources is under development, which will be useful in comparison with later surveys of the same region, as is for instance scheduled for the Nuclear Spectroscopic Telescope Array (NuSTAR), which will look for X-ray emission in the hard energy range of 6 – 79 keV. Out of these 1500 sources, at least 6 extended sources were detected, four of which were known on beforehand as SNRs and mentioned in SNR catalogs such as the Green catalog (Green 2009) and the new high energy Galactic SNR catalog (Ferrand et al 2012) and two of which are not listed in the mentioned catalogs and are therefore of unknown origin.

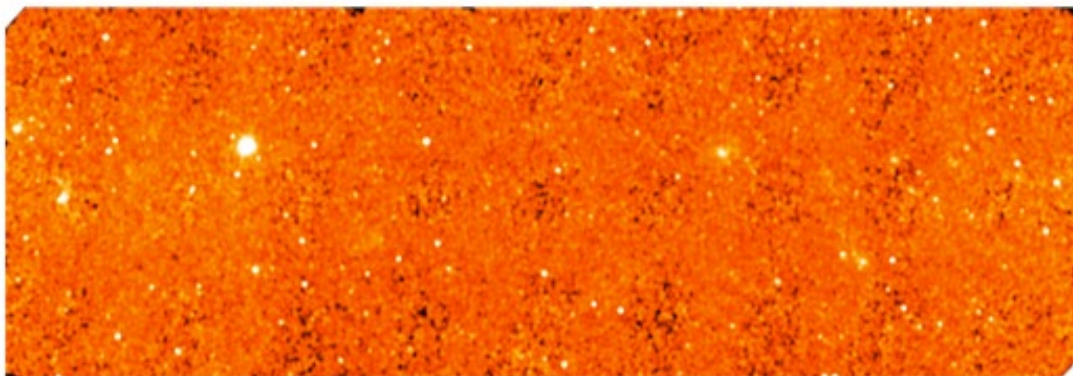
The focus of this thesis will be on three of the six sources: the two sources that are previously identified with other telescopes, but have not yet been subject to investigation using Chandra data (G337.2+00.1 and G337.8-00.1) and one of the new extended sources that have not been previously analyzed (CXOU J163802.6-471358). The three sources are listed in Table 1 showing the coordinates for the peak X-ray emission as determined from the previous missions with the exception of CXOU J163802.6-471358 where the coordinates are from the Norma region survey source catalog (Fornasini et al - in prep).

Additional to the Chandra data, also XMM Newton data, radio data from the Molonglo Galactic Plane Survey epoch 2 (MGPS-2), and infrared data from the Spitzer GLIMPSE survey and Vista all sky survey are available for the Norma region (a mosaic image of the MGPS-2 survey of the Norma region can be seen in Figure 10).

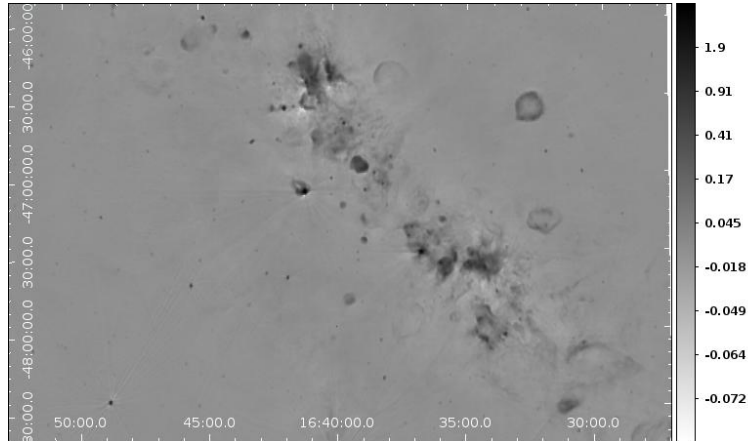
The high angular resolution data from Chandra together with the additional data available, makes it possible to determine the morphological characteristics of the new extended objects and to uncover some of the still unanswered questions regarding the already known ones. The open questions that will be addressed in this thesis will be presented in Section 5 based on the a priori knowledge about the three sources given here.



Figur 8: The image shows location of the Norma spiral arm, and its extension out to 15.5 ± 2.8 kpc from the Sun (Churchwell et al 2009). (Image credit: Churchwell et al 2009).



Figur 9: A mosaic image of the 27 Chandra pointings covering the Norma region. (Image credit: Tomsick 2013 - in prep).



Figur 10: The MGPS-2 radio map covering the Norma region. Obtained from the MGPS-2 source catalog web page <http://www.astrop.physics.usyd.edu.au/mosaics>.

Tabel 1:
Norma region sources

Source	R.A	Dec.	Type
G337.2+00.1	16:35:55.3	-47:19:04.5	plerionic composite?
CXOU J163802.6-471358	16:38:02.7	-47:13:58.4	? ^a
G337.8-00.1	16:38:55.7	-46:58:32.4	thermal composite

^aThis source is newly discovered and the source type has therefore not been determined.

4.2 G337.2+00.1

SNR G337.2+00.1 was first discovered in the 843-MHz radio survey by the Molonglo Observatory Synthesis Telescope (MOST) (Whiteoak & Green 1996) and has an integrated flux density of 1.6 ± 0.2 Jy. The radio source is positioned at $(\alpha, \delta)_{J2000} = (16^{\text{h}}35^{\text{m}}55^{\text{s}}.8, -47^{\circ}19'03'')$ in equatorial coordinates, with a 3σ uncertainty of $15''$. Later radio analysis of the source was done by Combi et al 2005, comparing the MOST results to the results from a higher frequency survey (4.85 GHz), and estimating from that a mean spectral index for the radio source of $\alpha \sim -0.78$. Using data from the Southern Galactic Plane Survey (SGPS) they identify a sharp absorption feature in the HI map at a velocity of $\sim -20 \text{ km s}^{-1}$, which is interpreted as the SNRs interaction with the foreground ISM. From this they infer a distance to the source of at least 13.5 kpc. This result and the angular size of the radio source of 2×3 arcmin are further used in combination with the Sedov self-similar solution from Equations 5 and 6 in order to yield an age of the remnant of $\sim 1500 \text{ yr}$, and a shock front velocity of $\sim 215 \text{ km s}^{-1}$.

X-ray emission from G337.2+00.1 has been observed with the ASCA telescope (Sugizaki et al 2001) and with the XMM Newton telescope (Combi et al 2006). The X-ray emission peak in the XMM Newton observation was located at $(\alpha, \delta)_{J2000} = (16^{\text{h}}35^{\text{m}}54^{\text{s}}.95, -47^{\circ}19'02''.2)$ with errors at 90% confidence of $\epsilon_{\alpha} = \pm 2^{\text{s}}.1$ for the right ascension and $\epsilon_{\delta} = \pm 3''.3$ for the declination, which is in good agreement with the previous estimate of the position of the radio emission (Combi et al 2005).

The XMM Newton observation does not reveal a limb-brightened shell structure for the SNR,

and the size of the X-ray emission is therefor not concluded (Combi et al 2006). No point-like emission is observed in the center of the remnant

The spectral analysis of the source done by Combi et al (2006) contain extraction and evaluation of spectra from the whole source (defined as a circular region with a 50 arcsec radius), the central emission (a circular region with a 12 arcsec radius), and from the outer diffuse emission with the compact center excluded (an anulus of inner-outer radius 12 – 50 arcsec). The three spectra were fitted with a non-thermal power law model and a thermal model, both affected by absorption. The best fit was obtained with an absorbed powerlaw and the spectral investigation showed signs of spectral softening with increasing radius, with the photon index varying from $\Gamma = 0.96$ in the inner region of the SNR to $\Gamma = 2.38$ in the outer region. The column density was determined to be $nH \sim 5.9(\pm 1.5) \times 10^{22} \text{ cm}^{-2}$ (Combi et al 2006). This is consistent with the X-ray source being of plerionic nature (Combi et al 2006; Boccinno & Bykov 2001). From this and from the actual values of the photon indexes, Combi et al (2006) concluded that G337.2+00.1 must be a non-thermal SNR with a pulsar wind nebula in the center. However, no pulsations from the central compact X-ray emission have been detected and the presence of a PWN is therefor not fully concluded.

4.3 CXOU J163802.6-471358

This source is not to be found in any of the mentioned catalogs, and the detection of this source has to our knowledge not previously been reported. This means that no a priori information is available for this object.

4.4 G337.8-00.1/Kes41

This SNR was first discovered with the Molonglo telescope at 408 MHz (Shaver & Goss 1970). The radio source is $6' \times 9'$ in size and exhibits a distorted shell structure which is elongated in the northeast-southwest direction. A distance of 7.9 kpc was inferred from HI observations (Caswell et al 1975), whereas a distance of 12.4 kpc was determined from the detection of maser emission by Koralesky et al (1998). A spectral index of $\alpha = -0.51$ was obtained from spectral fitting (Combi et al 2008, Shaver & Goss 1970).

The SNR has been detected in the X-ray regime by the XMM Newton telescope (Combi et al 2008). It is observed to be centrally brightened with the emission filling the radio structure and being brightest in the South-Western part of the radio shell. Combi et al (2008) produced narrow band images in the energy ranges 0.5 – 2.0 keV, 2.0 – 4.0 keV, 4.0 – 6.0 keV, and 6.0 – 10.0 keV, which showed that the source is almost undetected below 2.0 keV and that most of the emission lies in the energy range of 2.0 – 6.0 keV.

They report that a spatial spectral investigation was not possible due to a low number of detected counts, but a spectrum of the whole source was extracted from an elliptical region with a major axis of 5 arcmin and a minor axis of 3.2 arcmin (Combi et al 2008). The resulting spectrum was fitted with a NEI model affected by absorption and the fit showed signs of emission features originating from S XV and Si XIV at ~ 2.4 keV. The X-ray luminosity of the source was found to be $L_X \sim 4.5 \times 10^{34} \text{ erg s}^{-1}$ and $L_X \sim 1.3 \times 10^{35} \text{ erg s}^{-1}$ for a distance to the remnant of 7 and 12 kpc, respectively.

The source is interpreted as being an addition to the emerging SNR type called thermal composites or mixed-morphology remnants based on the centrally brightened X-ray thermal

emission and the shell-like non-thermal radio emission. The radio emission is proposed to be originating from the SNR shock front where high energy electrons produce synchrotron emission (Combi et al 2008). Based on the location of the remnant close to a massive molecular cloud, the most likely explanation for its peculiar morphology is deemed to be that of White & Long (1991) where clouds are proposed to evaporate in the center of the remnants giving rise to thermal emission (described in Section 3.5.2).

5 This thesis - open questions

The a priori knowledge presented in the previous chapter, leaves some open questions about the three Norma region sources. To address these questions, we make use of the observations made by Chandra described in Section 4 and compare the results to data from XMM Newton, MGPS-2, Spitzer or Vista data where it is meaningful.

5.1 G337.2+00.1

Especially questions concerning the morphological typing of this remnant are of importance. Questions about the spatial properties of this source can be addressed using the excellent spatial resolution of the Chandra telescope.

Three archived Chandra obsIDs cover the remnant (a summary of the details can be seen in table 2). Two of the observations (12523 and 12526) are from the Chandra Norma region survey, whereas the last one (10087) is an observation from an observation done by Halpern in 2010. None of the three obsIDs have ideal pointing, as the two Norma observations have the source located at a large off-axis angle as can be seen in Table 2, and the third observation has the source located almost on axis, which means that it is somewhat influenced by chip gaps. However, the Norma survey observations both cover the whole remnant on one chip, and the source extension described in Combi et al 2006 is covered by the obsID 10087. It will be preferable to use the Norma survey observations for morphological studies on larger scales than previously done, whereas the third observation can be used in combination with the Norma survey observations in order to investigate the central part of the remnant emission. General exposure correction of the source will increase the reliability of the morphological investigations.

5.1.1 Morphological typing

A surface brightness profile of the source based on a deep exposure obtained from merging the observations might reveal the overall spatial structure of G337.2+00.1 as it was for instance done for the composite SNR G310.6-1.6 (Renaud et al 2010). As described in Section 4, no limb-brightened emission has been detected previously. This means that a possible discovery of limb-brightening will trace the forward blast wave shock and provide a more secure estimate of the remnant age, and the expansion velocity through application of the Sedov-Taylor self-similar solutions. It has furthermore not been securely determined whether or not the SNR contains a PWN and the signature of such a structure could also be revealed by the radial profile.

Through spectroscopic investigations it might be possible to reproduce some of the previously determined parameters concerning the spectral nature of the compact central emission of the proposed PWN and the point-like emission in the very center of the remnant and because of the very dim nature of the source, a hardness ratio map will be calculated for complementary purposes.

Based on the result of the full source surface brightness profile, all or some of the following components of the SNR G337.2+00.1 will be investigated in the present thesis:

1. Point source
 - (a) surface brightness profile with more narrow binning compared with a simulated PSF will determine how point-like the central emission is.
 - (b) timing analysis in order to look for pulsations

2. PWN

- (a) spectral fitting to determine nature of emission

3. Shell

- (a) surface brightness profile fit with a gaussian will provide an estimate of the broadness
- (b) spectral fitting to determine nature of emission

Tabel 2:
Norma region survey

ObsID	Source	Date of observation	Instrument/chip#	Exposure [ks]	Off-axis angle [arcmin]
10087	G337.2+00.1	2010-06-22	ACIS-I/0123	10.03	0.5
12523	G337.2+00.1	2011-06-14	ACIS-I/1	19.01	8.4
12526	G337.2+00.1	2011-06-14	ACIS-I/3	19.02	6.4
12519	J163802.6-471358	2011-06-13	ACIS-I/3	19.56	3.8
12520	J163802.6-471358	2011-06-13	ACIS-I/0	19.25	8.4
12513	G337.8-00.1	2011-06-27	ACIS-I/1	20.42	10.4
12514	G337.8-00.1	2011-06-10	ACIS-I/0	20.05	8.9
12516	G337.8-00.1	2011-06-11	ACIS-I/3	19.76	8.5
12517	G337.8-00.1	2011-06-11	ACIS-I/2	19.76	6.6

5.2 CXOU J163802.6-471358

The main goal for the analysis of this object, is to determine the source type. Since the emission is point-like, but show signs of extension, it has been proposed that the emission could be that of an evolved pulsar driving a PWN (Tomsick - private conversation).

Two Chandra Norma region observations cover the source in question (obsIDs 12519, and 12520), and they are listed in Table 2. They both have the source located in the edge area of the chips, which is not ideal. The source was not picked up as a point source in the thorough source detection search reported in the source catalog but picked out by eye.

1. Imaging

- (a) Narrow energy range images in order to look for size versus energy effects.
- (b) Radial profile along symmetry axis to investigate cometary structure.
- (c) Comparing the X-ray and radio emission available to look for an elongated tail.

2. Spectroscopy

- (a) Spectral investigation and comparison with XMM Newton spectrum to determine nature of emission and look for softening with increasing radius.

No optical data is available for the region, and the absorption in the line of sight of the Norma spiral arm is high, which means that it is not possible to look for a bow-shock in $H\alpha$. However, motivated by the fact that infrared observational data is available for the position of the sky where the PWN candidate is located, images from the Spitzer GLIMPSE survey and the Vista

all sky survey were obtained and used to look for an infrared counterpart. This was inspired by a newly released paper on arXiv, where a serendipitous detection was made of an infrared bow-shock near a moving pulsar (Wang et al 2013).

Finally, a search for pulsations will be performed for the point-like source.

5.3 G337.8-00.1

Since this source is a mixed morphology (MM) remnant, the most interesting aspect of it, is its spectrum. Depending on the count rate of the source, an examination of the remnant spectrum will be performed with the aim of reproducing the spectral fitting done by Combi et al (2008).

Four Chandra Norma observations cover the source (12513, 12514, 12516, 12517), with exposures 20.42 ksec, 20.05 ksec, 19.76 ksec and 19.76 ksec, respectively (see Table 2) which potentially provide a good photon statistics. However, the peak emission coordinates determined by Combi et al (2008) reveals that the source is located on the edge or very close to the edge of the chip in all of the four observations and taking into account the size of the remnant given in Combi et al (2008), the remnant will be severely affected by chip gaps as it also was in the XMM Newton observations analyzed by Combi et al (2008).

One of the characteristics of a MM is that its central thermal emission is homogenous in temperature. If it is possible to extract spectral information from the source, and if it is possible to extract more than one spectrum, the homogeneity of the thermal emission will be a valuable thing to investigate.

No pulsar is expected to reside in the remnant, but it cannot be discarded that a pulsar is present without a more reliable spectral and spatial analysis that might be provided with Chandra. If the Chandra data shows non-thermal emission from a not prior detected point-like source, the nature of this SNR could instead be much more complicated.

6 Methodology

Before commencing the analysis, all relevant files were downloaded from the Chandra Data Archive through WebChaSeR (<http://cda.harvard.edu/chaser/>). A search of the database was performed using the coordinates for each of the relevant sources with a search radius of 10 arcmin in order to make sure that no other observations of the sources were available. Only in the case of G337.2+00.1 an additional observation was found, and it is listed in table 2. All observations used in this work were done with the ACIS-I instrument in the Timed Exposure VFAINT mode without any grating. Timed Exposure has the advantage that one can control the amount of time (Frame Time) that the CCD collects data before the charge is transferred and read out. The VFAINT mode provides a reduced background for sources with low count rates, where the risk of saturation and pulse pileup is minimal (Chandra X-ray Center 2012). Since the Norma region sources suffers from massive extinction leading to a generally low count rate, the VFAINT mode is preferable.

The downloaded files include:

- **Level 2 event file** (evt2.fits) - these files contain the event lists for each obsID including the event number and corresponding time, energy and sky coordinates. These files constitute the core in the further analysis. They are produced from the level 1 event files by filtering them with the Good Time Intervals (GTIs), which are when all parameters that affect the quality of the data are within acceptable ranges.
- **Bad pixel file** (bpix1.fits) - contains a list of flagged pixels, which means that they did not live up to the criteria set on beforehand. Reasons for identifying a pixel as "bad" include hot pixels and pixels with bias problems during the observation.
- **Aspect solution file** (pcad_asol1.fits) - these files contain information about the orientation of the telescope, that is the pointing and the roll, as a function of time. It is with the combination of the aspect solution file and the event file possible to trace the accurate celestial position of one particular event.
- **Mask file** (msk1.fits) - this file holds information on which part of the detector was active during the observation.
- **Parameter block file** (pbk0.fits) - the parameter block file is used to determine observational parameters.

All analysis was done using the CIAO software version 4.3 and 4.4. CIAO is an analysis tool, customized for treating astronomical X-ray data (Fruscione et al 2006). The script packages and tools distributed together with the CIAO software release 4.3 and 4.4, including the SAOImage DS9 visualization tool, the fitting package Sherpa, the plotting package Chips, and the raytracing software ChaRT as well as the simulation software MARX, have also been used extensively throughout this work. For spectral fitting, the X-ray SPECTral fitting package XSPEC has been used.

The effect of pileup was not taken into account in any of the analysis since no pileup is expected when the source count rate is low.

The dither of the telescope We need to take into account that the sources might dither outside the edge of the chip. This is only an issue for G337.8-00.1, though since the two other sources are located well within the 8 arcsec half-amplitude of the edge. G337.8-00.1 is cut in half by

6.1 Filtering data

When the needed obsIDs have been downloaded for each of the sources, the event files are filtered, so that only the events falling on the chip of interest (the one where the source is located) are included in the further analysis. The event lists are also filtered so that events with an energy falling outside the energy range of interest are excluded. All filtering is done, using the CIAO routine **dmcopy**.

There are several reasons for filtering on energy. First of all because of molecular contamination on the CCD chips, which becomes larger than 10% below 1.0 keV, and affects the quantum efficiency of the detector (fraction of incident photons registered by the detector) severely. Secondly, the high energy particle background increases by a factor of 8 between 7 – 10 keV, which is important when investigating faint extended sources (Biller et al 2002). Because of the dimness of the sources in question, an energy interval of 0.5 – 8.0 keV have been chosen in the specific case of this thesis work.

6.1.1 Removing contaminating sources

It is important to remove any unwanted point sources from the event file in order to be able to localize diffuse emission. For the two Norma survey observations, information from a point source catalog under development was used (Fornasini et al - in prep). This catalog will be released some time this year and will contain detailed information about the location of point sources and extended sources in the Norma region and their significance. The significance of a source is a measure of how likely it is that the source is real and not due to background noise, and all point sources with a significance above the 3σ threshold were removed from the respective event lists used in this thesis. In the case where a non-Norma survey observation has been used for analysis, the CIAO source detection tool **wavdetect** has been utilized for that particular observation.

When the sources have been identified, regions representing each of them are defined in DS9 and are then removed using **dmcopy**.

6.2 X-ray imaging

Since Chandra provides a superior spatial resolution compared to previous X-ray telescopes, X-ray imaging is an important analysis tool in addressing the unanswered questions concerning the morphology and nature of the extended Norma region sources.

6.2.1 Merging event files

Whether or not to merge obsIDs have been evaluated for each source individually. It is highly favorable to get as deep an observation as possible of a specific source, especially if the source is dim. This can be achieved by merging separate data sets into one collective event file. There are several things though, that are of importance for the decision of merging event files, such as variability of the source, and off-axis angle as well as technical considerations.

It is generally not recommended to simply merge the event files of several observations. This is due to the fact that the telescope properties can change over time, which will affect the detector response. These effects counts contamination effects which will increase over the lifetime of the telescope, as well as changes in the telescope pointing for each observation. The change in the detector response is taken into account in the newly released CIAO routine **merge_obs** where the response files are calculated for each observation, and then afterwards combined into one. This routine is therefore used in all cases where merging of observations have been favorable.

The event files are given as a comma separated list together with their respective aspect solution files, bad pixel files, masking files and parameter block files. Exposure maps and exposure corrected images are created automatically with this routine, and for that reason, one needs to supply `merge_obs` with a binsize and with one (or several) energy bands. A standard choice is the science energy bands, which are divided into a broad energy band containing the whole range of energies, the soft band which spans 0.5 – 1.2 keV, the medium band of 1.2 – 2.0 keV and the hard band 2.0 – 7.0 keV. The hard band is in this work chosen as 2.0 – 8.0 keV in order to match the energy filter used. An exposure map is created for each of the bands, evaluated at a specific monochromatic effective energy for each band. By comparing the exposure corrected images for the soft, medium and hard energy bands, it is possible to determine the approximate hardness of the source.

6.2.2 Exposure correction

The analysis of extended sources is influenced by the spatial variation of the exposure across the source. That the actual exposure varies is related to the variation in response of the telescope, which is for instance caused by telescope vignetting. This is when there is a fractional decrease in the telescope throughput with growing off-axis angle, because photons passing through the telescope with a large incident angle might not get a second reflection and are therefore bend away from the focal point, or simply absorbed before reaching the detector. The effective area of the telescope is therefore lessened for large off-axis angles (Chandra X-ray Center 2012).

The real source flux is related to the observed count rate through an equation that involves the effective area of the telescope, roughly taken as the product of the effective area of the mirrors and the quantum efficiency (QE) of the detector. At one given energy, the effective area as a function of the position on the detector is called the instrument map and combined with the pointing of the telescope during the observation, as it is given in the aspect solution file, will result in an exposure map, containing values for the spatial variation of the exposure across the source. The exposure map is created based on the information available in the aspect solution file for the observation and on information from an instrument map. The instrument map is an image of the effective area of the mirrors projected to detector coordinates with the quantum efficiency of the detector applied. In generating the exposure map, the information about the telescope pointing given in the aspect solution file is used in order to get the effective area in terms of the sky position. The exposure map can then be used to correct the count image of the specific source in question (CIAO AHELP Guide 2013).

The effective area of the telescope is furthermore dependent on energy, which means that the source flux is dependent on the spectrum of the source. This is linked to the fact that the reflectivity of the mirrors vary with energy, as the grazing angle for total reflection of higher energy photons is bigger than for lower energy photons. For that reason it is necessary to create an exposure map that is weighted with energy, for extended sources, where the spectrum varies across the source, but if one can show that the source only has a throughput in a narrow energy band, an approximate exposure map can be made from one monochromatic energy.

Other than taking into account the spatial variations of the exposure, and sometimes the variations of the exposure with energy, an exposure map can also reveal the existence of bad columns and bad pixels. That is pixels that for some reasons were turned off during the observation.

6.2.3 Radial profile

It is possible to calculate a radial profile of a source using the CIAO scripts **dmextract** and **dmtcalc**. Several concentric annuli, centered on the source in question and covering the whole source area, are selected in DS9 and saved as one region file. This region file can be used as an input to **dmextract** and a histogram over number of counts can be calculated, where each annulus represents a bin of a specific area. The number of annuli is chosen so that the bin size provides the grounds for good statistics. A background region is also defined and subtracted in order to achieve the average net counts for each region.

The exposure map generated by the CIAO routine **merge_obs** was supplied as well, in order to take the spatial exposure variation into account. The result is a file with several columns that can be used to plot the radial profile. The needed columns are the radial distance from the pulsar given in arcsec, the exposure corrected net flux per area and its corresponding errors. The radial position is determined as the midpoint of the bin. The surface flux is calculated as the exposure corrected net count values for each bin divided by the total region area, and the errors are the result of count error propagation.

The radial profile can be loaded into the modeling and fitting package Sherpa and fitted with a model of choice. Usually a beta model is chosen, which is a Lorentzian model with a varying power law:

$$f(x) = A \left(1 + \left(\frac{x - x_{\text{pos}}}{r_0} \right)^2 \right)^{-3\beta+1/2} \quad (25)$$

6.2.4 Determining the Chandra PSF

A PSF can be created using the Chandra Ray Tracer (ChaRT) and the MARX simulation software. The different input values to ChaRT counts the off-axis angle for the specific observation one needs to model (see Table 2 for values of the off-axis angle for the different obsIDs), obtained with the CIAO script **dmcoords**, an energy (or several energies), which is chosen in the case of this work as the peak emission energy of the source under investigation, and a value for the energy density selected by reading off the effective area of the ACIS-I at 5 keV. The ray density for the simulation is then picked as number of source counts/effective area at the specified energy. The output from ChaRT is a ray package which describes the energies, reflection angles and other relevant parameters. The MARX software then projects the ray package onto the detector, simulating the detector response and making it possible to use the resulting event file for further analysis almost on equal footing with a real observation.

the PSF image is usually binned to match a Chandra observation with a 0.492x0.492 pixel size.

6.3 X-ray spectroscopy

An important tool in astrophysical analysis, is spectroscopy. As we have seen in chapter 3 of this thesis, it is also important in the context of supernova remnants, as a spectrum can tell us a lot about the nature of the SNR, its parameters (such as shock velocity, plasma temperature etc.), and can in the case of a very young SNR be used as an indicator of the SN explosion type.

6.3.1 Spectral extraction

A spectrum can be extracted from an event file using the CIAO script **specextract** taking manual defined regions of the source as input. The region of interest was first selected from the

merged event file where the features are more obvious, and then applied to the individual observations. A source spectrum and background spectrum were created for all regions of interest together with a weighted ARF (Auxillary Response File) and RMF (Response Matrix File). The ARF contains information about the telescope pointing (as given in the aspect solution file for the observation), the detector and telescope effective area and the quantum efficiency (QE) of the detector. For extended sources, the ARF is weighted across the source using a weight map also created by the script **specextract**. The RMF contains information needed in order to relate energy to pulse height in the detector and this is also created in the same run. The script also takes the contamination calibration into account automatically.

It is possible to combine several spectra in one run of the script. This is for instance useful in the context of this thesis since one of the sources has very few source counts, and combining spectra from several observations will produce a spectrum with better statistics that can be fitted with an appropriate model and in some cases it will also make it possible to use χ^2 statistics in the fitting procedure. The spectra can only be combined if no variability is expected from the source, and since we are dealing with SNRs that are only slowly varying, this is valid within reason.

No binning is done for any of the spectral extractions since it is more favorable to do that later with the **grppha** tool distributed with the HEASARC software package. In that way it is possible to produce several binned spectra and from that select the ideal binning for further analysis. All spectra in this thesis have been binned with the method of a minimum number of counts in each bin. Typically a value of 15 is used, but for some spectra with a large spread in counts because of a low count rate, no grouping was done at all.

When a spectrum is grouped, information is lost, since photons of slightly different energy is put in the same bin (statistik papirer). This gives better statistics in the sense that one can use χ^2 statistics as described in Section 6.4.1, but for spectra with very few counts, and therefor a large spread in photon energies, the spectrum will be heavily processed. In the case of this thesis, the sources are all influenced by a large column density, and thereby very few counts in the soft X-ray range. This means that grouping a low count spectrum will influence the calculation of the column density severely.

The choice of grouping is done on the grounds of preserving as much information as possible and still get a reasonable fit. Because the background is low in most cases, the chance of ending up with negative bins for the background subtracted spectrum is small, but it gets bigger when no binning is applied.

The background spectra were not grouped in any case, since the spectral fitting tool XSPEC does this automatically to match the source spectrum.

6.3.2 Spectral fitting with XSPEC

When a spectrum has been extracted and grouped with the **grppha** tool, it is loaded into the X-ray SPECTral fitting package XSPEC. Here it can be displayed and fitted with a customized model. The choice of model for each spectrum is made on the basis of Sections 3.1 and 4.

For each spectral extraction I have used a local background region for the background subtraction. Because of the high column density in the Norma region (as described in Section 4) I have not used the CALDB blank sky files for a background estimate, since they have an overweight of soft X-ray photons resulting in negative bins in the background subtracted source spectrum. The Wilms et al 2000 abundance ratios have been used for all spectral fitting in this thesis. An absorbed power law model has been the model of choice in most cases, but an absorbed Raymond-Smith model has also been utilized in some cases. The XSPEC components used are the following:

The **phabs** component is used for the absorption, since it is with this model possible to select appropriate, up-to-date abundance parameters:

$$M(E) = \exp[-n_{\text{H}}\sigma(E)] \quad (26)$$

where $\sigma(E)$ is the photoelectric cross section and n_{H} is the equivalent hydrogen column in units of 10^{22} atoms cm^{-2} .

The abundance parameters from Wilms et al (2000) are used and set by the **abund** command.

The powerlaw model used for fitting of non-thermal emission is the component **pegpwlw**:

$$A(E) = KE^{\Gamma} \quad (27)$$

where Γ is the photon index of the power law and the normalization is fixed in an energy interval chosen on beforehand as 2-10 keV.

6.4 Statistical analysis

In order to be able to evaluate the results of the analysis performed in this thesis, it is necessary to use statistics. The most common way to evaluate the best fit model to a specific dataset is by the use of χ^2 statistics. This form of statistics can only be used when the net count number is large. As described earlier this is typically not the case for the present analysis and for the situations where it has been necessary, Cash statistics has been used.

6.4.1 Fit statistics

The most commonly used goodness of fit measure is as mentioned the χ^2 statistics, which can help determine how well a specific model can explain a specific distribution of data points (in this case distribution of counts). This is done by dividing the data into bins (energy bins in the case of a spectrum) and for each bin calculate the expected number of data points (or in this case the number of counts) for the specific model. If the data set was in fact produced by the model, the actual number of counts would lie very close to the expected value, and how much the two numbers deviates can be expressed with the χ^2 value, given by:

$$\chi^2 = \sum_1^n \frac{(\text{observed counts} - \text{expected counts})^2}{\text{expected counts}}, \quad (28)$$

with n being the number of bins.

If $\chi^2=0$ there is no deviation between the expected values and the measured values in any of the bins, which is highly unlikely, as some fluctuations are always expected when working with real physical systems. The individual terms in the equation is expected to be of the order 1, which means that χ^2 will be approximately equal to the number of bins n . If χ^2 is much larger than n the deviation between the expected and the measured values are too large, and the data set is most likely not governed by the expected model distribution (Taylor 1982).

In order to make a more correct assessment of the fit quality the χ^2 value can be compared to the degrees of freedom (d.o.f.) of the model instead of the number of bins. The d.o.f. is defined as the number of bins minus the number of free parameters in the model (or number of constraints). This means that the **pegpwlw** model described in Section 6.3.2 has 2 d.o.f., since the model contains 4 parameters (photon index, lower pegged value, upper pegged value and norm) but two

of them are frozen during the fit (lower pegged value and upper pegged value) (XSPEC manual 2010). Since the expected value of χ^2 is precisely the number of d.o.f., a more convenient way to express the χ^2 test result is by the use of the reduced χ^2 , denoted $\tilde{\chi}^2$:

$$\tilde{\chi}^2 = \chi^2/\text{d.o.f.}, \quad (29)$$

where the expected value is $\tilde{\chi}^2 = 1$, which thereby indicate that the data set is most likely produced by the model in question. If $\tilde{\chi}^2 \gg 1$ this indicates that the model did not produce the data set distribution, and if $\tilde{\chi}^2 \ll 1$ it indicates that the errors are somehow overestimated in the fit, since the value indicates a too perfect fit with no deviation between the measured value and the expected value in any of the bins (Press et al 1992).

In order to use the χ^2 test, the expected number of data points (or counts) in each bin should not be too low, which is why one needs to bin the data to get a specific minimum of counts in each bin in order to use χ^2 statistics. On the same note, the number of bins should not be too small as well, which is why it is not possible to use χ^2 statistics for a spectrum with very few counts (Taylor 1982).

If the requirement for χ^2 statistics is not fulfilled, that is if the data contains very few counts or very few bins, one can use counting statistics instead. However, this means that we will not get an automatic goodness-of-fit measure equivalent to $\tilde{\chi}^2$. Instead one can utilize the **goodness** command in XSPEC in order to get an estimate of the quality of the fit. The goodness command generates a number of fake spectra based on the model in use and calculates the fit statistics. The fit statistics distribution is then compared to the actual real data and a percentage is returned describing the amount of fake spectra that had a better fit statistic than the real data. If the data was produced by the model, the percentage will be around 50% (XSPEC manual 2010).

6.4.2 Error estimations

Besides being able to determine whether or not a model is appropriate for a particular data set, we also need to be able to know with which accuracy the best fit model parameters are determined, that is we need to know the size of the error bars and we need to know with which degree of confidence a particular parameter value has been determined.

Generally in this thesis, the 1σ error bars are approximated using the Gehrels weighting for a Poisson distribution (Gehrels 1986), where the upper limit is given by:

$$\sigma = \sqrt{N + 0.75} + 1 \quad (30)$$

And the lower limit is given by:

$$\sigma = \sqrt{N - 0.25} \quad (31)$$

where N is the number of counts in one particular bin.

This equation provides a weighted estimate of the confidence limits that will be applicable to data within the Poisson regime, and that will tend towards a Gaussian distribution for large N. The CIAO tools only operate with symmetric errors and selects therefore the largest of the two calculated values. A problem, however is that the high spatial resolution of the Chandra data and the low count rate of the sources, result in a lot of pixels with zero counts. This means that the zero count bins are given a symmetric and too large error and the errors turn out to be overestimated. For this reason, I have in the case of the radial profiles used for fitting, made use of the standard deviation from the mean for each bin instead of the Gehrels weighting evaluated in each pixel. The standard deviation from the mean is given as:

$$\sigma_{\text{SD}} = \sqrt{\frac{\sum(x_i - \bar{x})^2}{N - 1}}, \quad (32)$$

where N is the number of counts.

6.4.3 The F-test

The F-test is used to test the null hypothesis that two different models describe the same dataset equally well. That is that a more complicated model does not make a better fit to the data than a simpler model (Press et al 1992).

If two χ^2 values have been obtained from two different fits, the models can be compared using the F-test:

$$F = \frac{\Delta\chi_{12}^2/\Delta p_{21}}{\chi_2^2/\text{d.o.f.}_2}, \quad (33)$$

where $\Delta\chi_{12}^2$ is the difference between the best fit χ^2 value for the two models in question, Δp_{21} is the difference in number of parameters for the two models, χ_2^2 is the best fit χ^2 value for the second model, and d.o.f._2 is the number of degrees of freedom for the second model, defined as in Section 6.4.1.

The F-test can be performed using XSPEC and the command **ftest**, which returns an F-value and a percentage. If there is a significant difference between the two model variances, the F-value will be $\gg 1$ and the percentage will be small. The percentage describes how likely it is that the null hypothesis is true (Bevington & Robinson 2003). The more complex model will add more parameters, and will for that reason always provide a better fit than the simple model. This means that one needs to select a critical value for the F statistic, so that the null hypothesis can be rejected if the probability is larger than the critical value. The critical value is usually chosen to be 0.05 (Bevington & Robinson 2003).

The F-test is only valid if the models used are nested, that is that the simple model (model 1) can be obtained by selecting certain parameter values for the more complex model (model 2). It should also be fulfilled that the chosen values should not lie on the boundary of the parameter space. This will be discussed further in Section 8.

7 Results

In this Chapter, all results of the analysis are presented for each source separately.

7.1 G337.2+00.1

The data for the SNR G337.2+00.1 was prepared and filtered as described in section 6 and section 6.1, and all three observations covering the source were merged as described in section 6.2.1, in order to get as good statistics as possible. A non-exposure corrected merged image is shown in Figure 11 where also the contaminating sources are indicated with red circles. All point sources (other than the one indicated with circle number 1) were identified as described in Section 6.1.1 and the ones with a detection significance of $> 3\sigma$ were removed from the raw event files before they were merged and exposure corrected. The red circle labeled 1 were not removed, as it holds the emission from the suspected pulsar in the center of the SNR.

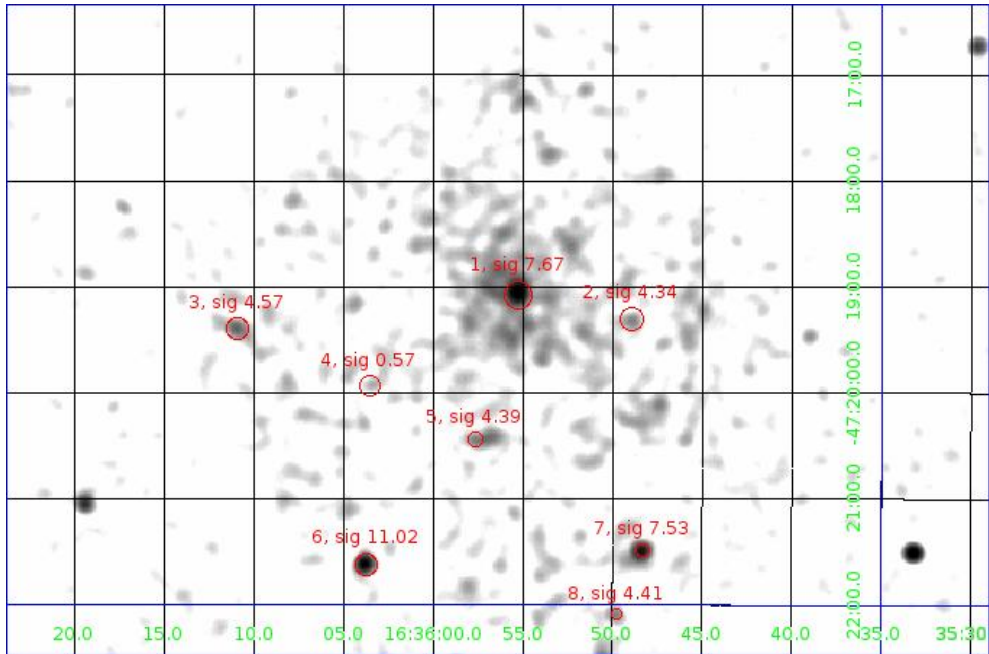


Figure 11: The merged observation of obsIDs 10087, 12523 and 12526, depicting the SNR G337.2+0.1. The contaminating sources listed in the Norma region survey point source catalog (Fornasini et al 2012) are represented by red circles. Only sources in the immediate vicinity of the SNR are represented. The circle label indicate the reference number, and the significance of the source detection. Only sources with a significance of $> 3\sigma$ have been removed from the event file. The image is binned so that each pixel spans 2×2 arcsec

7.1.1 The morphology of SNR G337.2+00.1

The cleaned event file was divided into sub energy bands representing the soft, medium and hard parts of the emission, which can be seen in Figure 12. Based on the fact that only the hard energy range ($> 2\text{keV}$) seem to contain emission from the source (see count historic in Table 3), a monochromatic energy of 3.8keV was chosen for the full band exposure map, which is presented in Figure 13. Fluxed exposure corrected images in the soft, medium, hard and full band were produced by dividing the counts image with the respective monochromatic energy

exposure maps as described in Section 6.2.2. The full band exposure corrected fluxed image can be seen in Figure 14 together with an overlay of radio contours from the MGPS-2 survey.

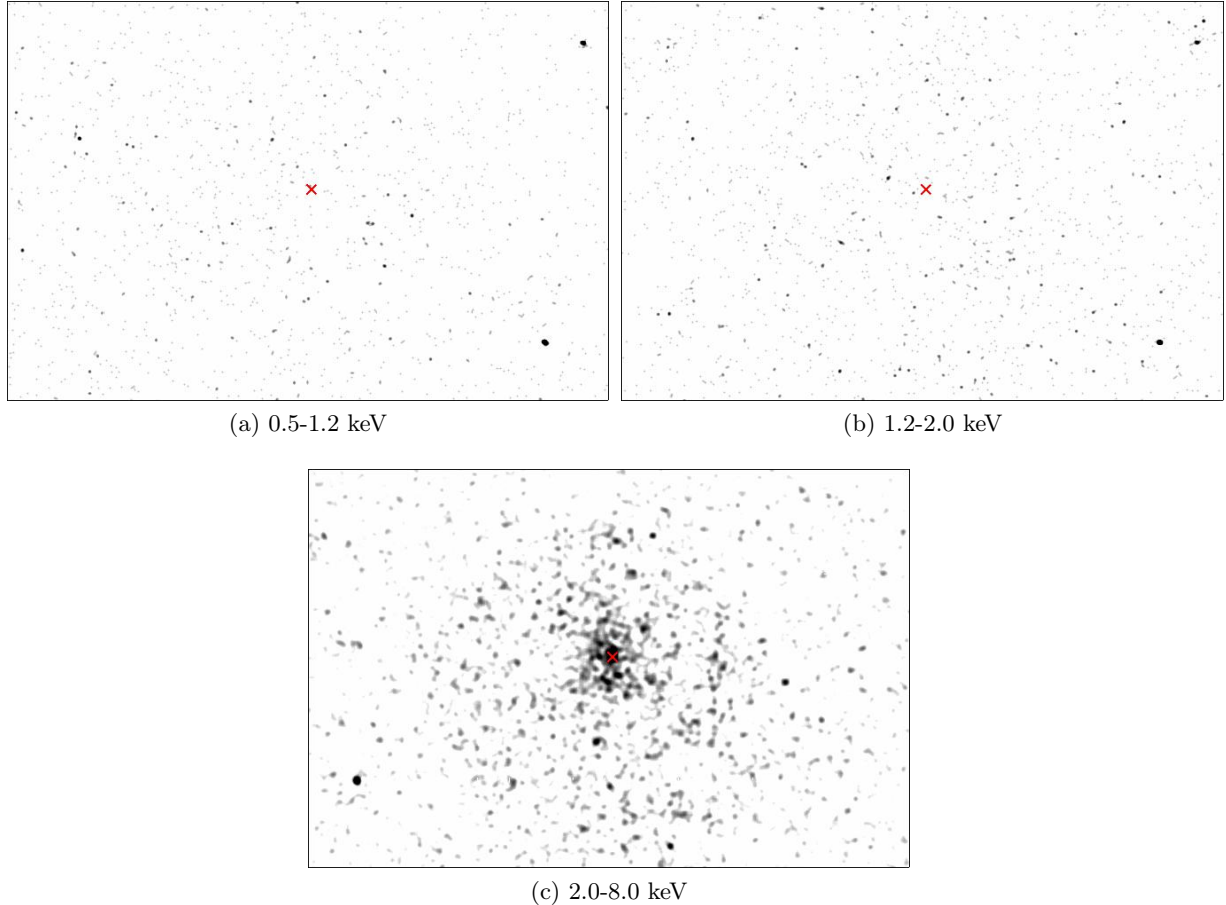


Figure 12: The three images show the merged event file in three narrow energy bands with the red cross marking the center of the source. a) shows the soft 0.5 – 1.2 keV emission, b) shows the medium 1.2 – 2.0 keV emission, and c) shows the hard 2.0 – 8.0 keV emission. Note that only the hard band image contain source emission.

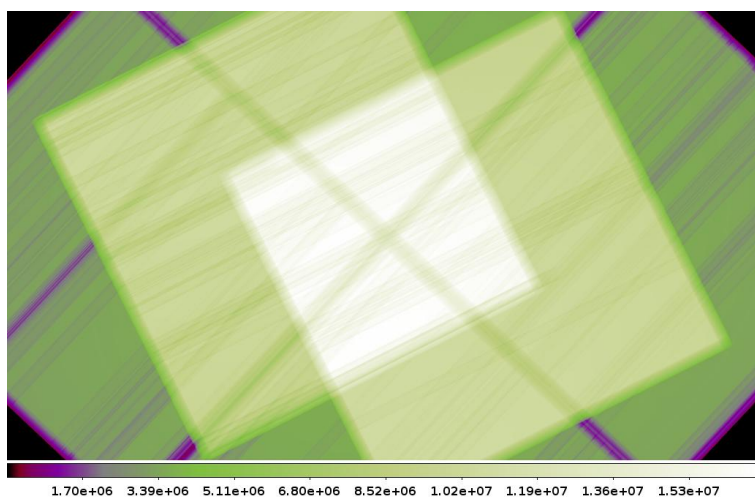
A surface brightness profile was calculated for the whole source using the approach described in section 6.2.3. The background region and annuli source regions used are all shown in Figure 15. The source annuli cover a circular region with radius 179 arcsec centered on the point-like emission in the center of the remnant and each annulus have a radial size of 5.8 arcsec. The exposure map in Figure 13 was used as an input both for the source and the background region in order to get an exposure corrected fluxed radial profile. The radial profile is shown in Figure 16 and the regions that are of interest in the morphological typing of the remnant are indicated with vertical lines.

7.1.2 The point-like central emission

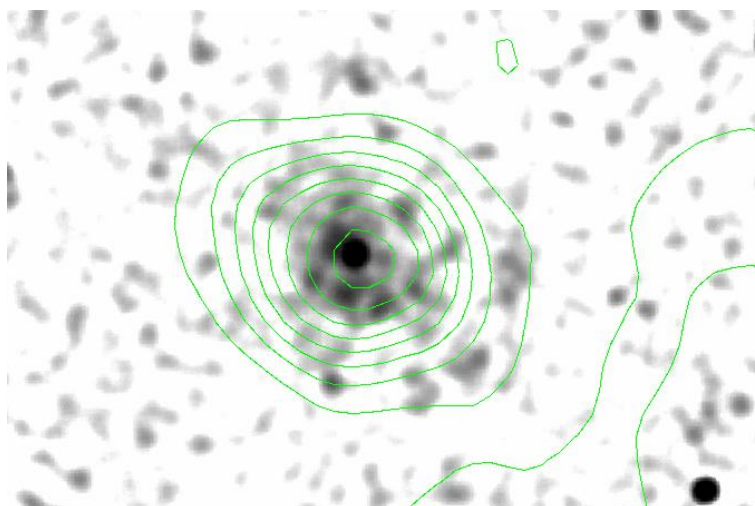
A radial profile with a more narrow binsize was done for the central emission of the SNR. It was evaluated whether to use the merged event file for a surface brightness calculation of the point-like source or just the obsID 10087, based on the simulated PSFs at the various off-axis angles.

Tabel 3:
Source counts for G337.2+00.1

Energy band [keV]	Net counts	Total counts
0.5-1.2	261.6	531
1.2-2.0	227.6	661
2.0-8.0	2369.8	4326



Figur 13: The full band (0.5 – 8.0 keV) exposure map of the merged event file.



Figur 14: The full band (0.5-8.0 keV) exposure corrected image of SNR G337.2+00.1. The image has been smoothed with a Gaussian kernel of $\sigma = 5$ arcsec. The radio emission levels goes from 0.02-0.30 mJy beam⁻¹ in steps of 0.04 mJy beam⁻¹.

The three PSFs, one for each of the three observations, can be seen in Figure 17. They were all produced using the ChART tool and the MARX simulator following the procedure described

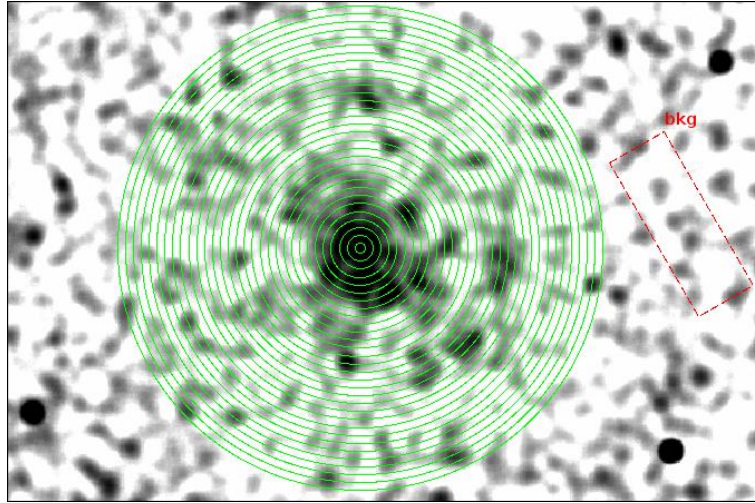
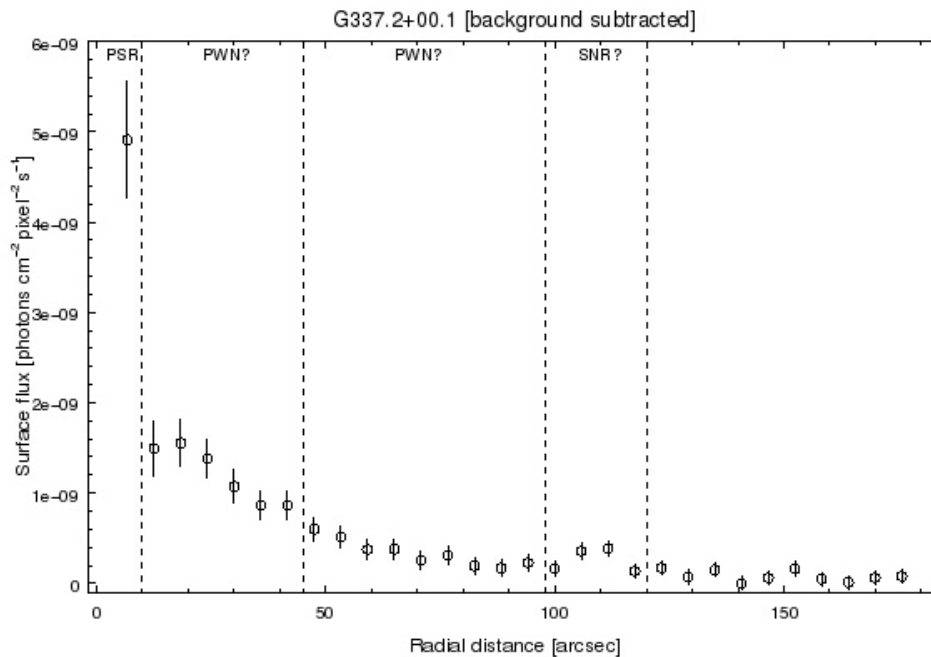


Figure 15: The full band exposure corrected image of SNR G337.2+00.1. The image has been smoothed with a Gaussian kernel of $\sigma = 5$ arcsec. The annuli used for calculation of the radial profile are shown in green and the region used for background subtraction is shown as the red dashed box.

in section 6.2.4. Based on this result, only the observation with obsID 10087 was used, because of its ideal off-axis angle of only 30 arcsec. A local background region was chosen on another chip at a slightly larger off-axis angle than the source, in order to account for the background emission. In order to determine how point-like the source is, a PSF was simulated with an exposure of 200ks at the same off-axis angle as the source. Since the PSF has been simulated to mimic an observation, it is possible to extract a radial profile of it following the same procedure as for a real observation. No background region was defined, since no background emission has been added to the simulated PSF eventfile. The long exposure time provides a nearly perfect PSF model and a comparison between the background subtracted radial profile of the point-like source and the PSF can be seen in Figure 18. The horizontal error bars mark the size of the bins used for the calculation and the vertical error bars are the counting errors calculated using Gehrels weighting and propagated to match the flux data. The PSF was evaluated at the same off-axis angle as the source in the actual observation, and with the same spectrum as the pulsar candidate. The PSF has been normalized to the peak of the point-like emission using $\text{PSF_norm} = \frac{\text{PSF}}{\text{PSF_max}} \times \text{PSR_max}$.

7.1.3 The spectral properties of SNR G337.2+00.1

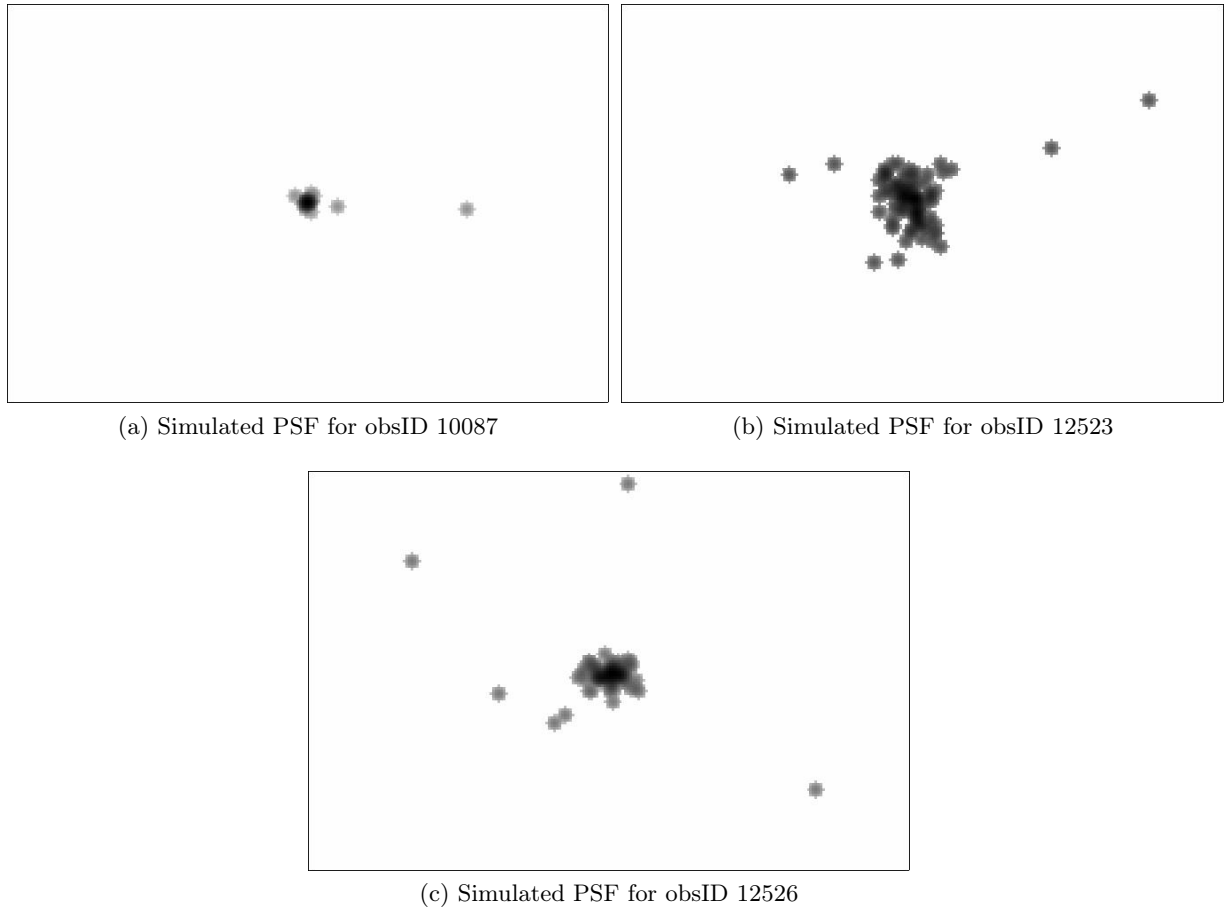
A thorough spatial spectral investigation is not possible, since the photon statistics is not good enough. However, spectra from two regions were extracted using the procedure described in section 6.3. A spectrum of the proposed PWN was extracted from a circular region with radius 42 arcsec, which is a little bit smaller than the 50 arcsec in radius of the extraction region used by Combi et al 2006. A smaller region was chosen in order to fit it on one chip in observation 10087. A spectrum of the PWN was extracted from each of the three obsIDs and fitted simultaneously in XSPEC. Each spectrum was grouped with a minimum of 15 counts per bin, in order to be able to use χ^2 statistics. A spectrum of the low count shell region was obtained by combining the spectrum from the two Norma region survey obsIDs (12523 and 12526) and grouping the resulting spectrum so that each bin has a minimum of 30 counts. The obsID 10087 was not used



Figur 16: Radial profile showing the surface flux of the G337.2+00.1 SNR. The vertical lines mark the different parts of the remnant, being the point-like source, the PWN whose extension is not obvious, and a small bump that can be interpreted as the signature of a remnant shell.

for the shell spectrum, since the source is located almost on axis and therefore is influenced by chip gaps. All spectral fitting of G337.2+00.1 was done using the Wilms et al. (2000) abundance ratios and an absorbed power law model (`phabs(pegpwlw)`). The best fit parameters are listed in Table 4 and the spectra can be seen in Figure 19.

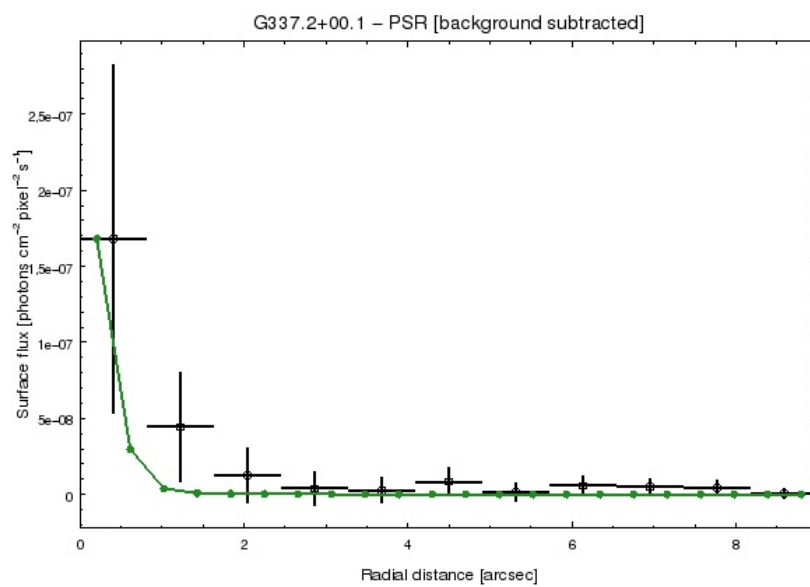
It was also attempted to fit the inner 25 arcsec of the nebula and the 42 arcsec outer part of the nebula, but too few counts were available for a spectral fit. It was additionally attempted to fit the shell spectrum with an absorbed thermal plasma model (`phabs(raymond)`) in order to see if this would provide a better fit. This was not the case, as the fit statistics stayed the same, but the parameters were badly constrained.



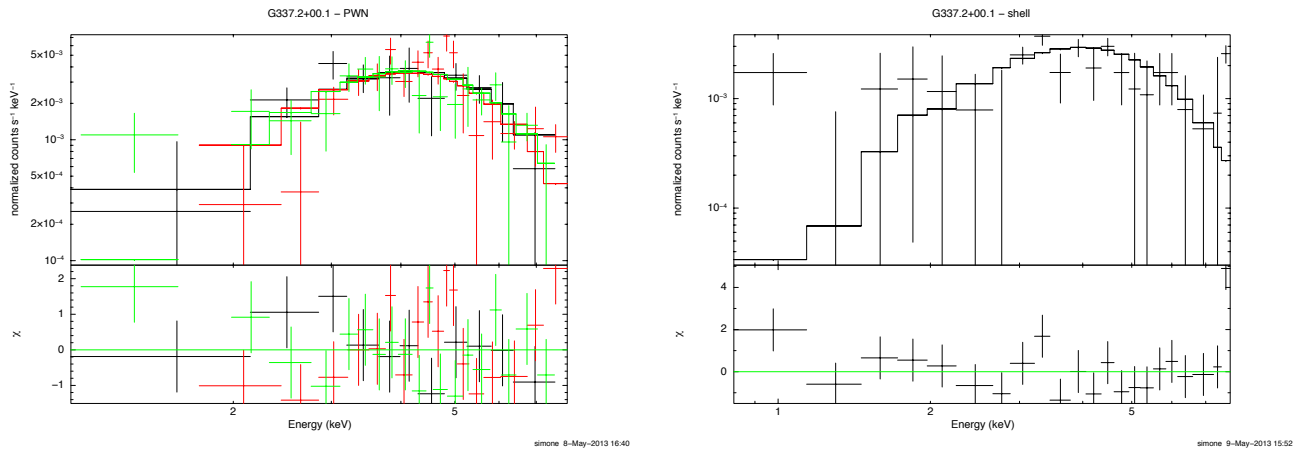
Figur 17: The panels show the simulated PSFs for the three SNR G337.2+00.1 observations. Each PSF has been simulated using the Chandra online ray tracer (ChaRT) and the Marx simulation software. a) is the PSF for obsID 10087, simulated at an off-axis angle of 0.5 arcmin with an exposure time of 10ks. b) is the PSF for obsID 12523, simulated at an off-axis angle 8.4 arcmin and with a 19ks exposure. c) is the PSF for obsID 12526 at an off-axis angle of 6.4 arcmin with an exposure of 19ks.

Tabel 4:
Spectral fitting results for G337.2+00.1

PL parameter	PWN	Shell
nH	$7.97^{+6.62}_{-4.90}$	(7.97)
Γ	$0.73^{+0.91}_{-0.78}$	$1.03^{+0.75}_{-0.76}$
Normalization	0.91	0.66
$\tilde{\chi}^2/\nu$	1.05/45	1.96/20
Abs. flux _(2–10 keV)	7.20e-13	5.07e-13
Unabs. flux _(2–10 keV)	9.09e-13	6.61e-13
Total net counts	~644	~383

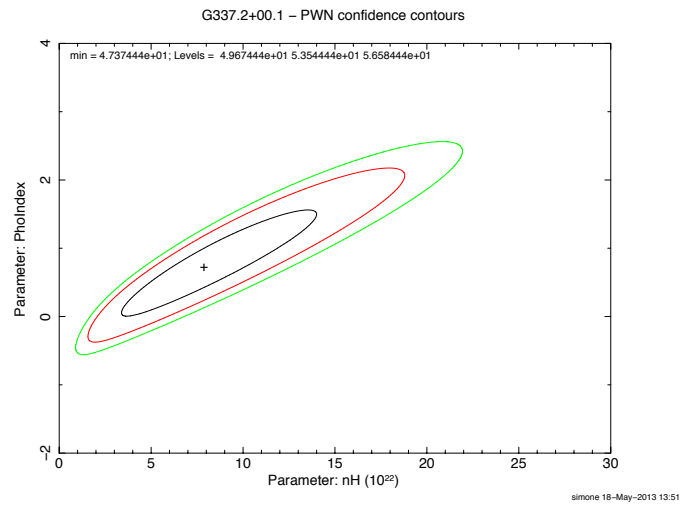


Figur 18: Comparison between the simulated PSF size and surface brightness profile of the central emission. The *green* curve shows the PSF and the *black* data is the radial profile of the central point-like emission.



(a) Spectrum of the PWN

(b) Spectrum of the shell



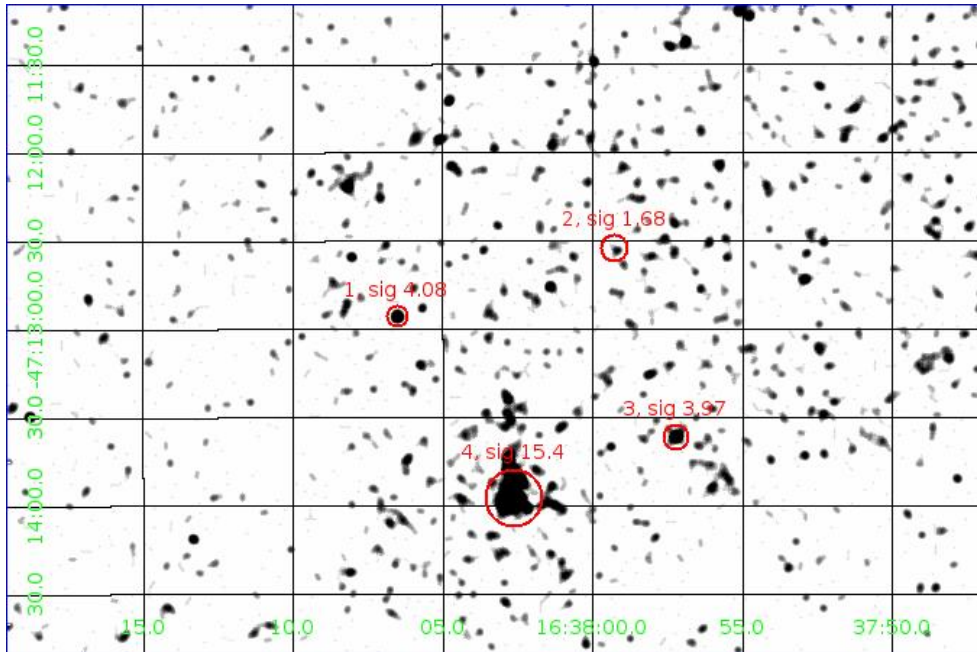
(c) Contours for the PWN fit

Figure 19: Panel *a* shows the spectrum of the PWN part of G337.2+00.1, panel *b* shows the spectrum of the shell part of G337.2+00.1 and panel *c* shows the confidence intervals for the parameters nH and Γ for the PWN spectral fit.

7.2 CXOU J163802.6-471358

Information from the Chandra Norma region survey source catalog (Fornasini et al - in prep) was again used in order to determine the position of any contaminating point sources in the vicinity of CXOU J163802.6-471358 (referred to as J1638 from hereon after. The merged non-exposure corrected image of J1638 can be seen in Figure 20 with the contaminating sources indicated with red circles. Again, only the contaminating sources with a significance above the 3σ threshold were removed from the respective raw event files and the two cleaned files were filtered on energy so that they only include events in the energy range 0.5 – 8.0 keV. The merged event file was then divided into the three science energy bands and as it can be seen from Figure 21, no source emission is detected below 2.0 keV. The number of source counts in the three energy bands are listed in Table 5. This allow us to use a monochromatic energy exposure map evaluated at 3.8 keV in order to create exposure corrected images in four bands following the procedure described in Section 6. The exposure map used can be seen in Figure 22. Three extra narrow band images of energy range 2.0-4.0keV, 4.0-5.5keV and 5.5-8.0keV were created splitting the hard energy band in three. The energy bands were chosen such that an equal amount of source net counts resides in each of them. The result can be seen in Figure 23.

An image of the exposure corrected full band merged observation is presented in Figure 24 with an overlay of radio contours from the MGPS-2. Note that there exists an offset between the X-ray emission and the radio counterpart. This is an interesting fact that we will address in Section 8.



Figur 20: The merged image of obsIDs 12519, and 12520, depicting the source CXOU J163802.6-471358. The contaminating sources listed in the Norma region survey point source catalog (Fornasini et al 2012) are represented by red circles. Only sources in the immediate vicinity of the source are represented. The circle label indicate the reference number, and the significance of the source detection. Only sources with a significance of $> 3\sigma$ have been removed from the event file. The image is not binned, so each pixel has the dimension of 0.492×0.492 arcsec and the image has been smoothed with a gaussian kernel size of $\sigma = 2.5$.

A surface brightness profile of the full band PWN candidate was calculated based on region slices taken along the symmetry axis. A slice width of 2 arcsec was used for the point-like source

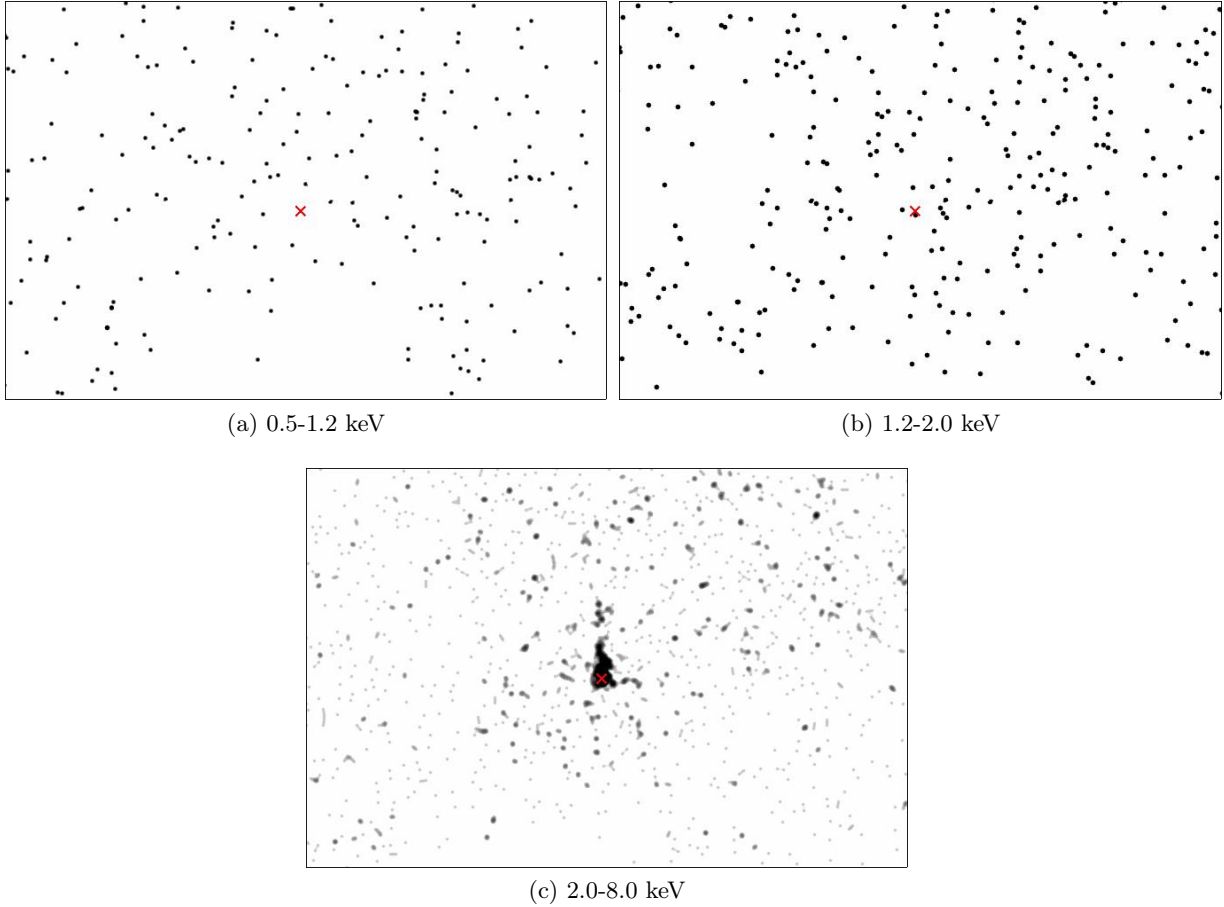


Figure 21: The three images show the J1638 emission in the soft, medium and hard band.

and a width of 4 arcsec was used for the rest of the source regions. The resulting exposure corrected profile can be seen in Figure 27 and the regions used can be seen in Figure 28.

Inspired by a newly released paper on arXiv, as mentioned in Section 5, a search for an IR counterpart to the source was done using the available Vista and Spitzer data. The results can be seen in Figures 25 and 26. Region 1 mark the point-like source position and the radius of the circle indicates the position error on the X-ray emission peak from the Norma region source catalog (Fornasini et al - in prep). Region 2 mark the main source region containing the point-like source and the short tail. Region 3 marks the extra diffuse emission seen as the longer tail part in Figure 27.

7.2.1 The spectral properties of CXOU J163802.6-471358

As mentioned earlier, an important tool in source typing is spectroscopy. Since the total source area only contains a total number of ~ 356 counts this means that caution must be taken when extracting numerous spectra from the source region. The spectral extraction regions used are shown in Figure 29 and the extraction was done following the steps in Section 6.3.

All spectra were left ungrouped because of the small number of counts (see Section 6.3 for more details), and for each region the spectrum taken from obsID 12519 and the one taken from

Tabel 5:
Source counts for CXOU J163802.6-471358

Energy band [keV]	Net counts	Total counts
0.5-1.2	8.24	11
1.2-2.0	-2.84	22
2.0-8.0	259.53	323

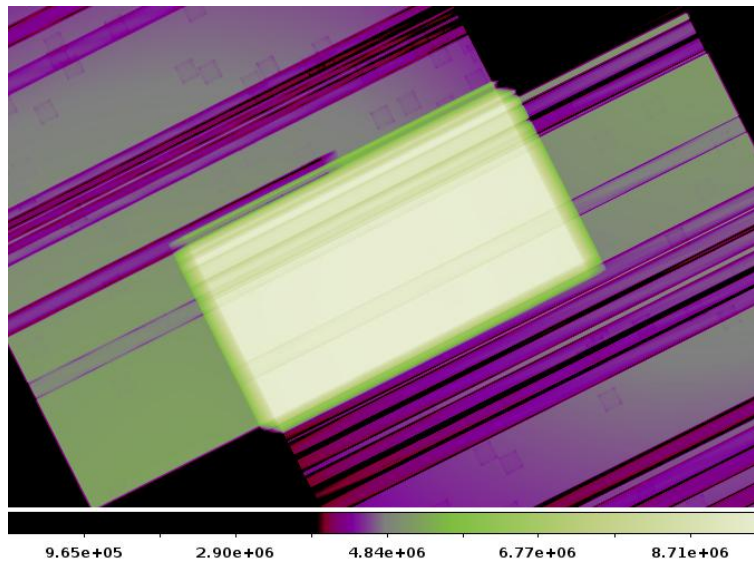
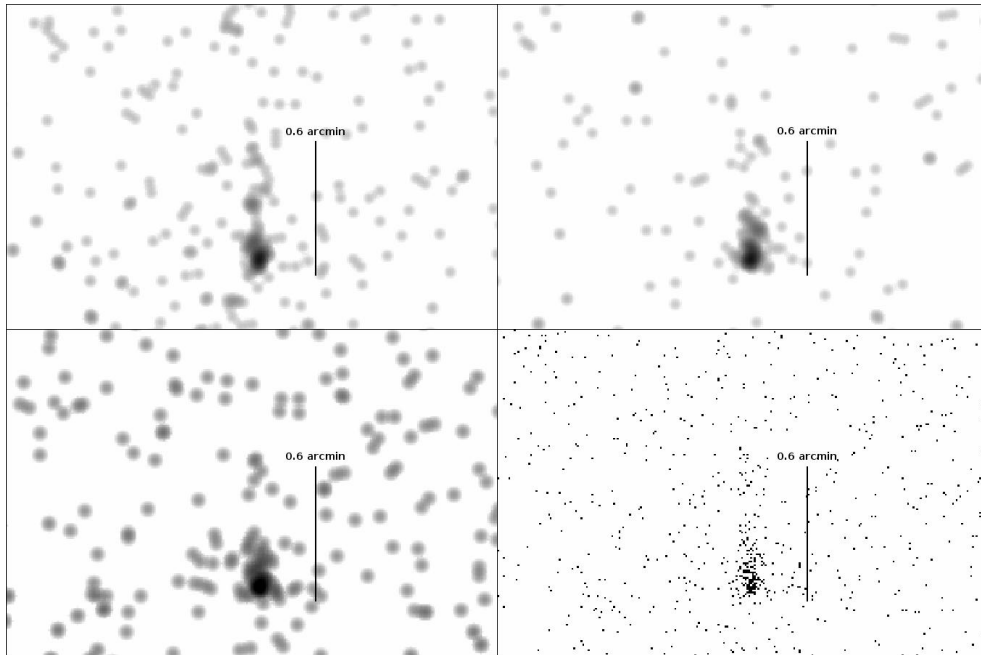


Figure 22: The exposure map for the merged observation of G337.2+00.1 evaluated at the monochromatic energy of 3.8 keV.

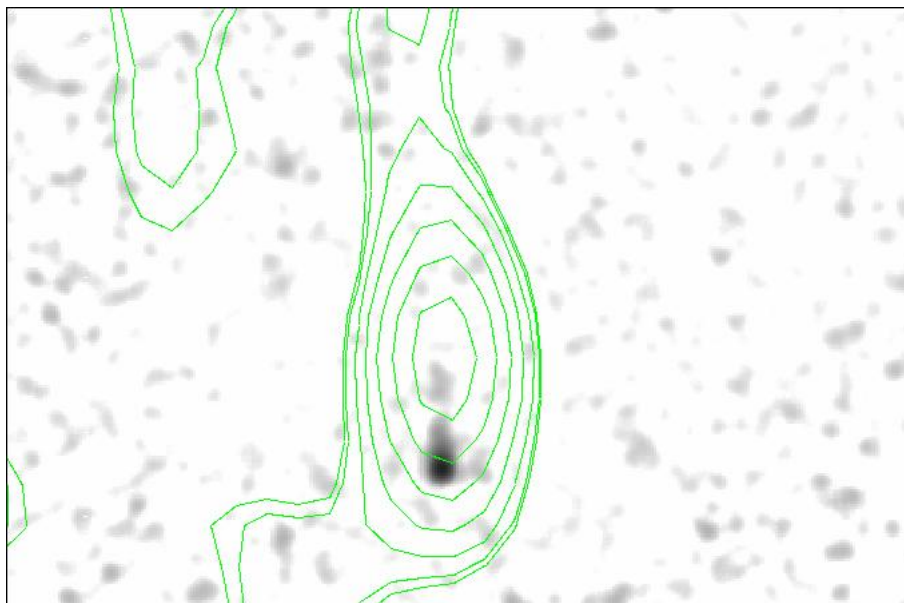
12520 were loaded into XSPEC and fitted simultaneously with an absorbed power law model (phabs(pegpwlw)). The full source spectrum was fitted first in order to get as good an estimate of the column density as possible, and the best fitted value was then used as a frozen parameter for the other spectral fits. The fitting results are all listed in Table 6.

A simultaneous fit of the three full source XMM Newton spectra was performed in order to compare the result to the Chandra full source spectrum fit. The three XMM spectra were grouped with 50 counts per bin for the MOS1 instrument data, 50 counts per bin for MOS2, and 100 counts per bin for PN. Energies below 0.3 keV and energies above 12.0 keV were ignored and the spectra were fitted with the usual absorbed power law model. The fitted spectra are presented in Figure 31 and the best fit result can be seen in Table 6.

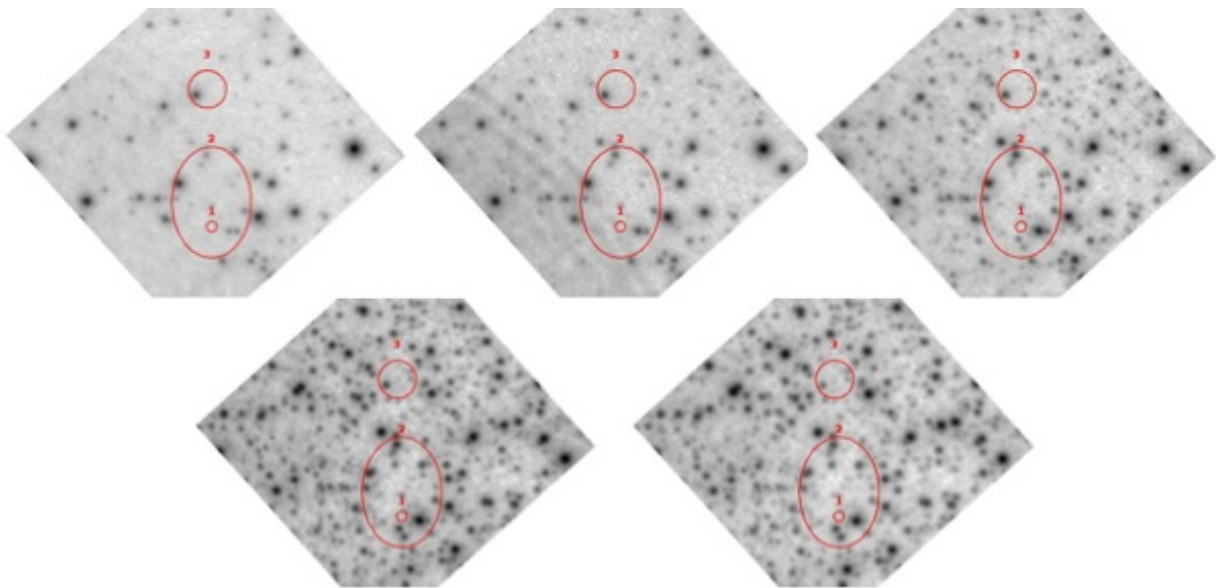
The confidence contours for the Chandra and the XMM spectral fits can be seen in Figure 32 for comparison.



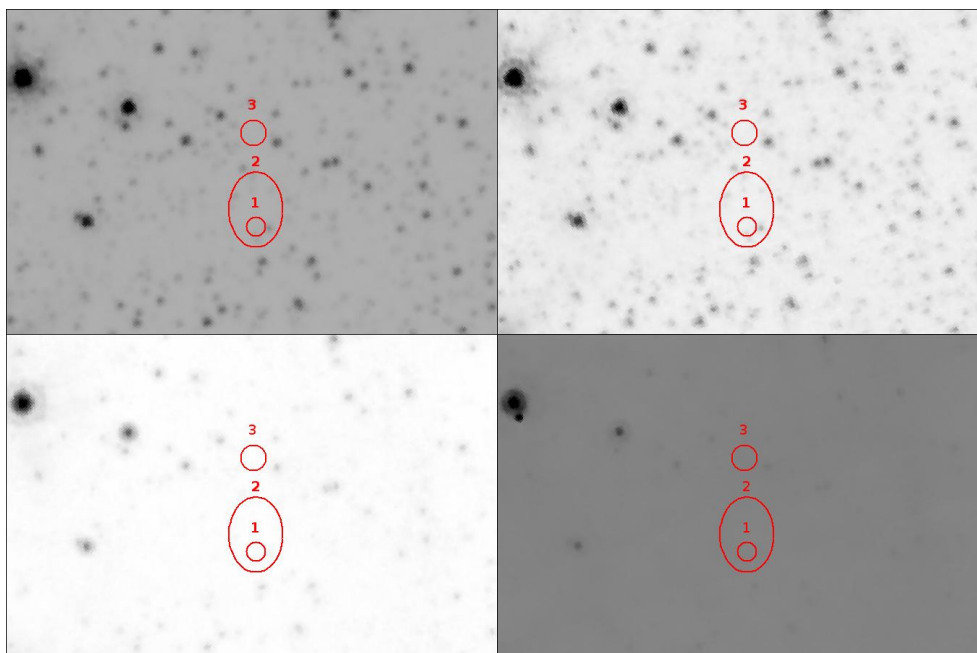
Figur 23: The PWN candidate is here shown in three exposure corrected narrow hard energy bands together with the full band non exposure corrected event file for comparison. The *top left* panel shows the 2.0-4.0 keV band image, the *top right* image is the 4.0-5.5 keV band, the *bottom left* panels shows the 5.5-8.0 keV band and finally the *bottom right* panel shows the full band, full resolution raw event file. The three first panels have been smoothed with Gaussians with a kernel size of $\sigma = 2.5$. All four images have the highest possible resolution of 0.492×0.492 arcsec pixels.



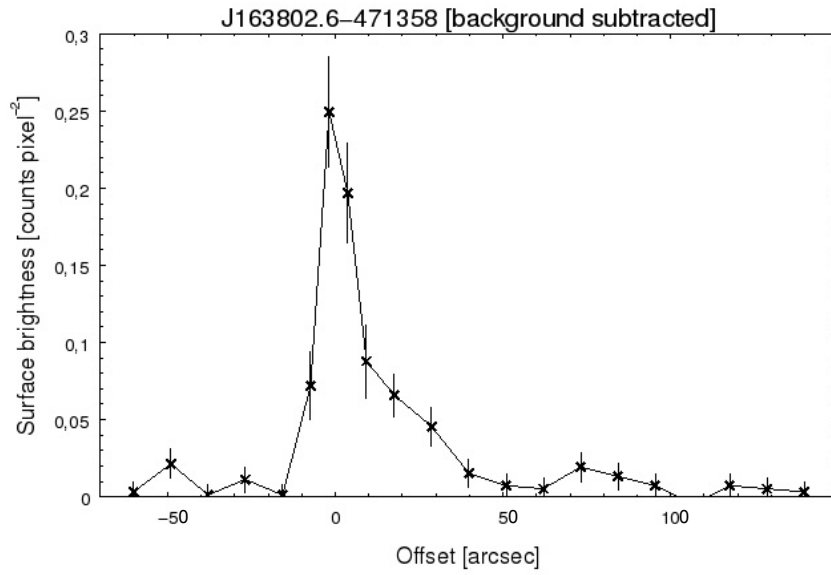
Figur 24: The exposure corrected full band image smoothed with Gaussians with a core radius of $\sigma = 2.5$ and an overlay of radio contours. The radio contours represents the levels 0.007, 0.0083, 0.012, 0.019, 0.028, 0.039, 0.053, 0.07 mJy beam^{-1} .



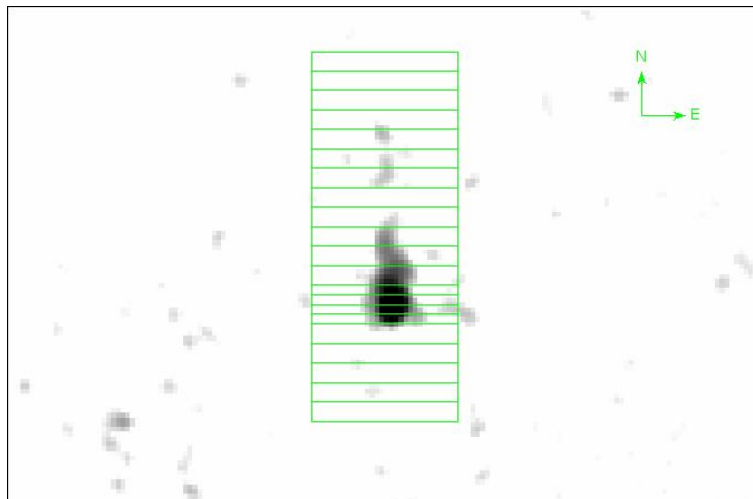
Figur 25: VISTA survey images. From top left: Z-band, Y-band, J-band, H-band, Ks.



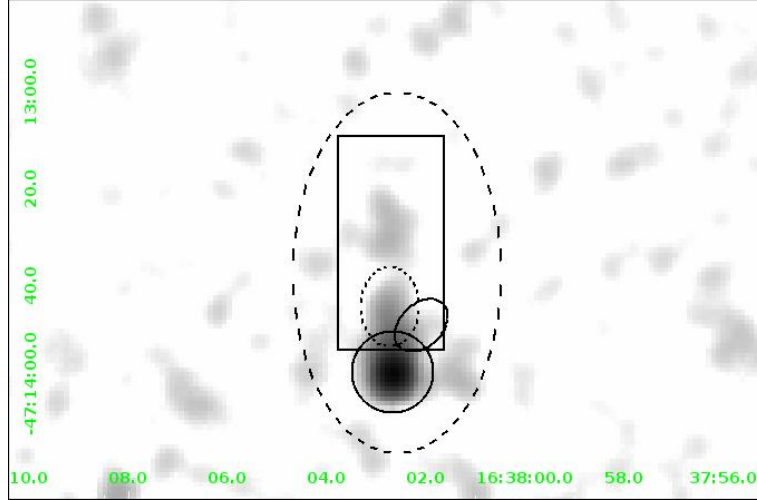
Figur 26: Spitzer GLIMPSE images. From top left: 3.6 μm , 4.5 μm , 5.8 μm , 8.0 μm .



Figur 27: The plot shows a radial profile of J1638 done from aperture slices along the symmetry axis.



Figur 28: The plot shows the region bins used to calculate the radial profile along the symmetry axis for J1638.

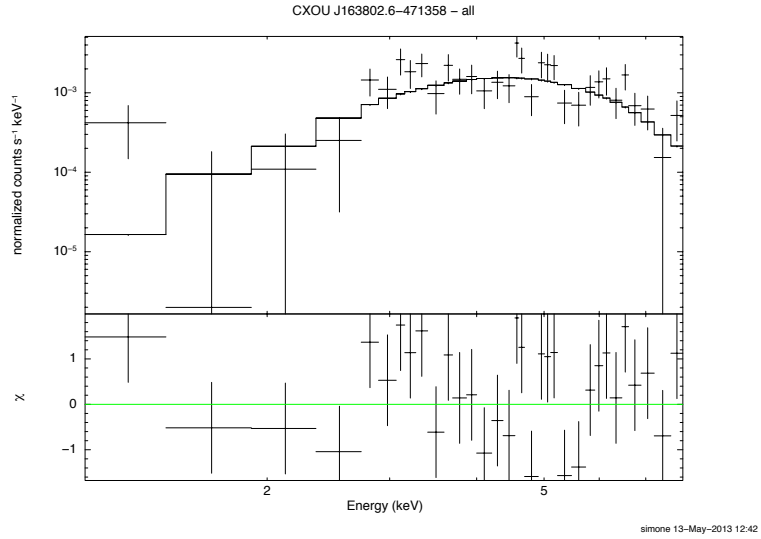


Figur 29: An exposure corrected full band image of J1638 smoothed with a Gaussian with a core radius of $\sigma = 2.5$. The black regions represent the extraction regions used in the spectral investigation. The *large dashed elliptical* region corresponds to the full source region in Table 6, the *circular solid line* region corresponds to the point source, the *rectangular* region is the tail region, the *small dashed ellipse* corresponds to the short tail region, the *small solid lined ellipse* is the side tail region.

Tabel 6:
Spectral fitting results for CXOU J163802.6-471358

Region	nH [10^{22} cm^{-2}]	Γ	Goodness of fit [10000 iterations %] ^a	Absorbed flux	Unabsorbed flux
1 - full source	$10.50^{+7.85}_{-5.50}$	$0.57^{+1.10}_{-0.93}$	43.9	$3.67\text{e-}13$	$4.83\text{e-}13$
2 - point source	(10.50)	$0.14^{+0.46}_{-0.47}$	73.5	$3.55\text{e-}13$	$4.47\text{e-}13$
3 - tail	(10.50)	$1.12^{+0.87}_{-0.87}$	60.7	$8.42\text{e-}14$	$1.19\text{e-}13$
4 - short tail	(10.50)	$0.60^{+0.99}_{-1.10}$	60.5	$5.91\text{e-}14$	$7.77\text{e-}14$
5 - side tail	(10.50)	$-0.45^{+1.60}_{-1.79}$	33.8	$7.65\text{e-}14$	$9.23\text{e-}14$
XMM full source	$27.8^{+11.64}_{-8.56}$	$2.6^{+1.14}_{-0.91}$	68.15/50	$2.72\text{e-}13$	$8.77\text{e-}13$

^aThis percentage is based on a Monte Carlo simulation with 10000 iterations done in XSPEC using the goodness command.



Figur 30: Grouped spectrum of CXOU J163802.6-471358, the total source region. Grouped with a minimum of 10 counts per bin for visualization purposes.

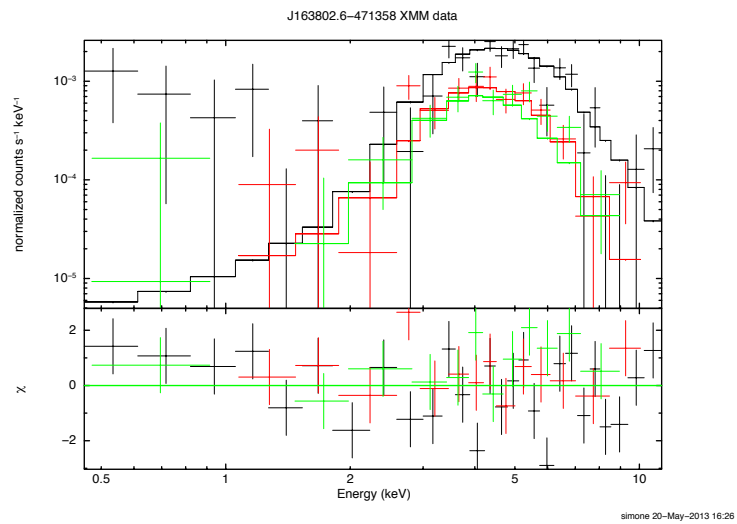
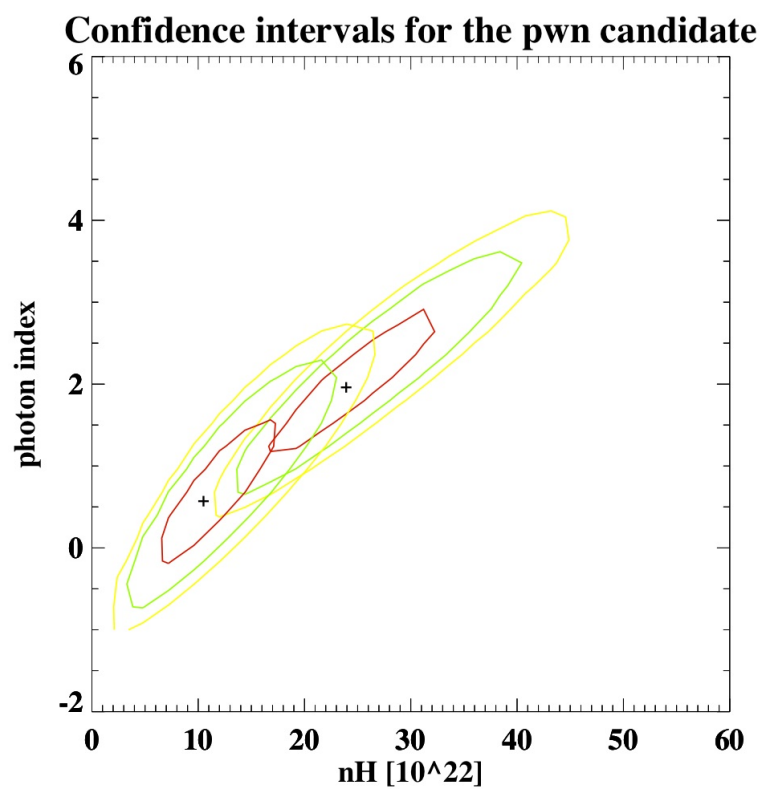


Figure 31: The figure shows the three XMM Newton spectra used for fitting.



Figur 32: Comparison between the confidence intervals for the XMM Newton spectral fit and the Chandra full source spectral fit. The contours correspond to 1σ (red), 2σ (green), 3σ (yellow). Notice the overlapping 1σ contours.

7.3 G337.8-00.1

The four Chandra Norma region observations were prepared and filtered in the same way as for the other two sources and merged in order to examine how the observations cover the source. An image of the merged observations can be seen in Figure 33 where the source is marked with a red elliptical region. The green boxes show how the different observations overlap across the source region. The contaminating point sources above the significant threshold of 3σ (marked with red circles in Figure 34) were removed and the merged event file was filtered in the soft, medium and hard energy bands, as shown in Figure 35 (see count historic in Table 7). Since most emission is detected above 2.0 keV I again chose a monochromatic energy of 3.8 keV for the exposure map (presented in Figure 36). It was attempted to extract narrow band images of the 2.0-8.0 keV range, but no structure was seen in the resulting images, since the structure is very diffuse and blends into the background.

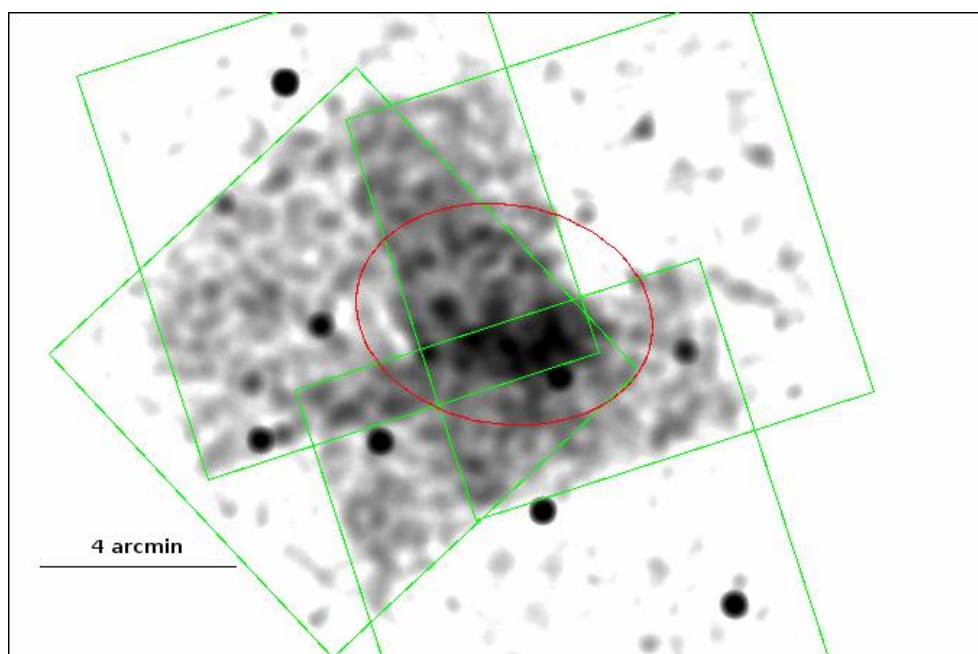


Figure 33: The non-exposure corrected merged image of obsID 12513, 12514, 12516, and 12517. The green box shapes indicate the extension of each observation, and the red elliptical region marks the source position.

Tabel 7:
Source counts for Kes41

Energy band [keV]	Net counts	Total counts
0.5-1.2	75.61	574
1.2-2.0	297.85	871
2.0-8.0	1564.54	4314

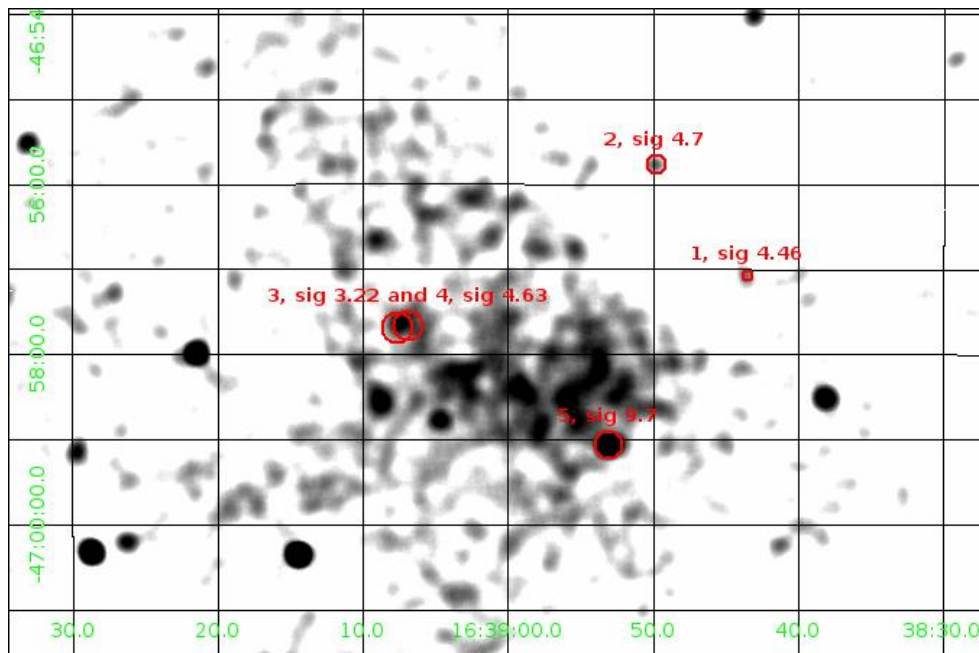


Figure 34: The non-exposure corrected merged image with the contaminating sources indicated by red circles. Only sources above the 3σ significance threshold, and point sources located in the immediate vicinity of Kes 41 are presented. The image has been heavily smoothed with gaussians with $\sigma = 5$ in order to force visualization of structure. Notice the weak emission in the North and North-Eastern corner of the remnant which forms a ring-like shape.

7.3.1 The spectral properties of G337.8-00.1

Spectral extraction of the whole source region was attempted, but as it was expected, the resulting spectrum did not provide the basis for fitting any model. A fit based on an absorbed thermal model and on an absorbed power law was performed, but both of the models resulted in unconstrained parameters.

Extraction of a spectrum and subsequent fitting with an absorbed power law was attempted for the contaminating point source labeled 5 in Figure 34, in order to investigate the possibility of it contributing to the spectral fitting done by Combi et al (2008) using XMM Newton data.

The source is heavily influenced by its position on the edge of the chip in all observations, as can be seen from Figure 33. Since observation 12517 contains most of the compact emission securely on one chip, the optimal approach would be to extract the spectrum from only that observation. This is not possible though, since the photon statistics is too poor.

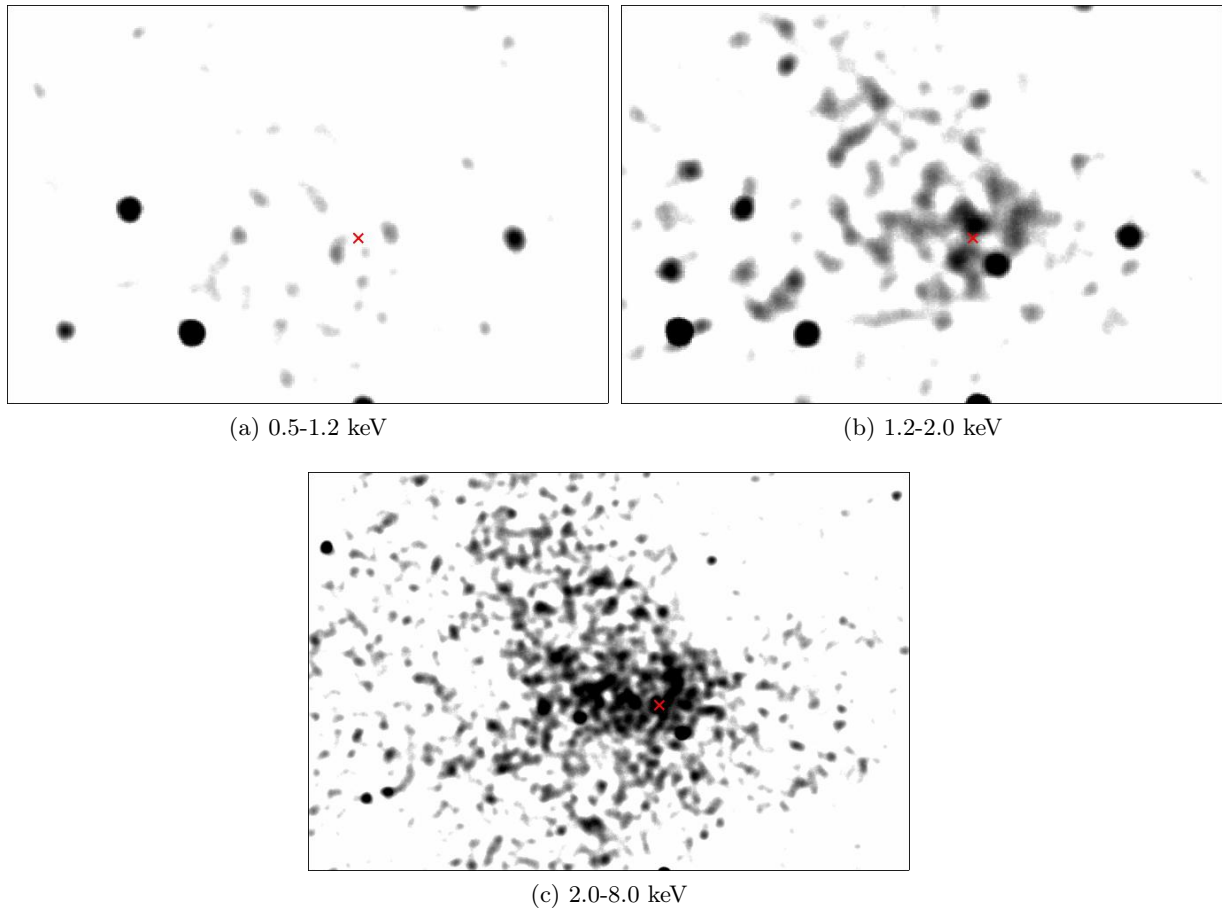


Figure 35: Three narrow band images of Kes 41. The red x marks the position of the X-ray emission peak from XMM imaging. Notice the location of a point source in the near vicinity of the x by comparing with Figure 34.

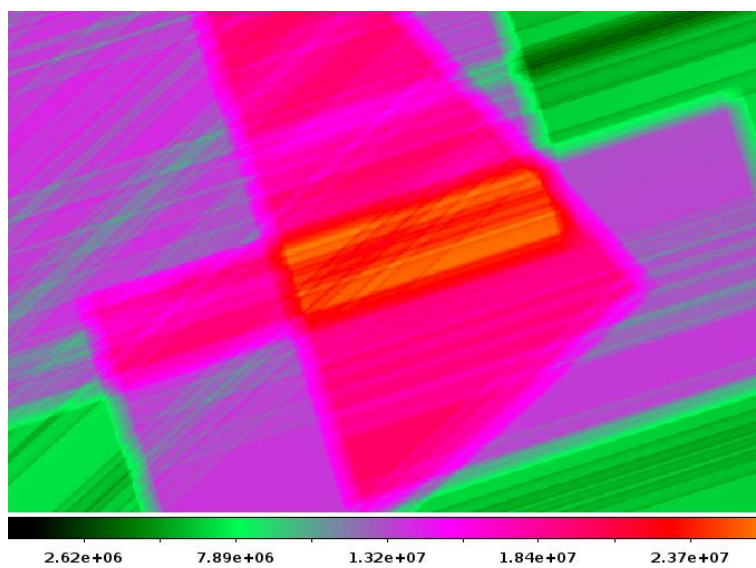
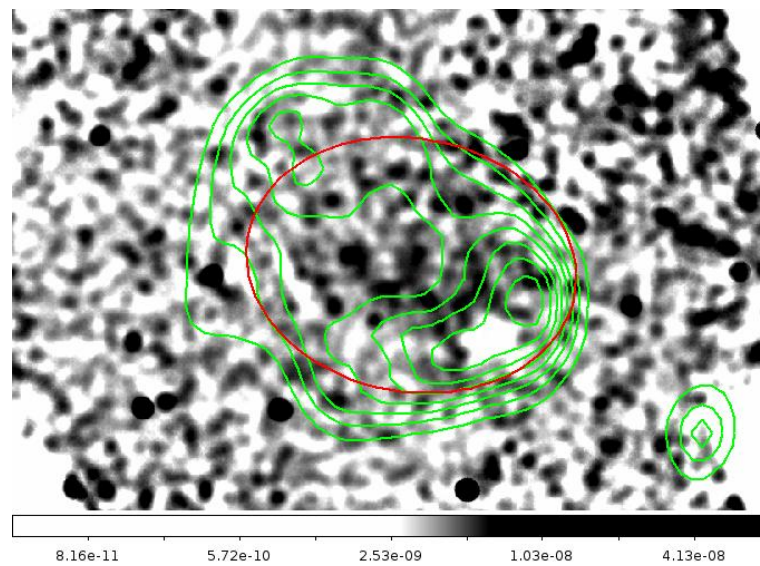


Figure 36: The exposure map evaluated at 3.8keV for the merged observation.



Figur 37: The full band exposure corrected image of Kes41 with an overlay of radio contours from the MGPS-2. The red ellipse is the same one as in Figure 33. The 9 contours levels range from 0.1 to 1.0 mJy beam $^{-1}$ in steps of 0.11 mJy beam $^{-1}$.

8 Discussion

8.1 G337.2+00.1

G337.2+00.1 is listed as a composite SNR with a question mark in the high energy SNR catalog (Ferrand & Safi-Harb 2012). The high spatial resolution of the Chandra telescope made it possible to construct a surface brightness profile of the whole remnant area (see Figure 16), which reveals a structure that is consistent with G337.2+00.1 being a composite SNR.

The surface brightness profile shows a sharp jump in emission from the first data point to the second. This indicates that the central emission is close to that of a point source, which is expected for a composite remnant with a pulsar in its center. Further examination of the central point-like emission through a narrow binned surface brightness profile (see Figure 18) and comparison with a simulated PSF, shows that the source is extended but close to the size of the PSF when taking the errors into consideration. It is expected that the source has a larger extension than the PSF, since diffuse emission is expected to be located in near vicinity of the pulsar (Slane et al 2000), so the existence of a pulsar can neither be confirmed nor rejected. It was attempted to extract a light curve from the source, but since the extraction time intervals were limited by the low count rate, no meaningful results could be extracted.

The emission from the supposed PWN was fitted well with an absorbed power law (see Table 4). When comparing the best fit column density value of $nH = 7.97 \times 10^{22} \text{ cm}^{-2}$ with the value of $nH = 1.86 \times 10^{22} \text{ cm}^{-2}$ obtained from the Leiden/Argentine/Bonn (LAB) Survey of Galactic HI (Kalberla et al. 2005), the fitted value is almost a factor 4 bigger. Since our line of sight towards the Norma region is almost tangent to the Norma spiral arm, and therefore intersects with the known location of several molecular hydrogen clouds (Bronfman et al 1989), it is expected that a source located on the far side of the spiral arm, as it is the case for G337.2+00.1, will be heavily absorbed.

The best fit photon index $\Gamma = 0.73$ is lower than what Combi et al (2006) obtain for the full PWN region, which is $\Gamma = 1.82$, but is consistent with what they obtain for the inner 12 arcsec (equivalent to the pulsar region) of $\Gamma = 0.96$ within 90% confidence.

From the integrated broad band flux of the PWN we can calculate its luminosity, using the unabsorbed flux value from Table 4 and the distance $D \approx 14 \text{ kpc}$ given in Combi et al 2006:

$$L_X = F_X 4\pi D^2 = 4\pi \cdot 9.09 \times 10^{-13} \text{ ergs cm}^{-2} \text{ s}^{-1} \cdot (4.32 \times 10^{22} \text{ cm})^2 = 2.13 \times 10^{34} \text{ ergs s}^{-1} \quad (34)$$

It is still not possible to fully conclude the presence of a pulsar without detection of pulsations. Based on the radial profile of the central emission and based on the detection of non-thermal synchrotron emission in its vicinity, we will assume that a pulsar is present in the center of the SNR G337.2+00.1 at the location of the X-ray emission peak. The coordinates are given in the Norma region Chandra source catalog (Fornasini et al - in prep) as $(\alpha, \delta)_{J2000} = (16^{\text{h}}35^{\text{m}}55^{\text{s}}.27, -47^{\circ}19'04''.52)$ with a position error of $\pm 1.2 \text{ arcsec}$. The position was also determined manually by binning the full band source image to a binsize of $\sim 4 \times 4 \text{ arcsec}$ and identifying the pixel with the largest count number. The value is consistent with the catalog coordinates within the error.

It is possible to find an estimate of the spin-down luminosity of the proposed pulsar using the approach described in Section 3.5. Because of the high absorption in the 0.2-4keV band, the Seward & Wang equations were not ideal. That leaves us with the Possenti et al (2002) equations which are also the most recent and based on the largest sample of pulsars. Using the above value for the luminosity in the 2-10 keV range, we get a spin-down luminosity value of the order

$$\dot{E} = 1.09 \times 10^{37} \text{ ergs s}^{-1}.$$

A small bump is observed in the radial profile of the full source at ~ 109 arcsec from the central emission peak, which could indicate the presence of a shell. This claim is supported by the visual evidence seen for instance in Figure 11, where a weak trace of diffuse emission is observed in the South-Western part of the remnant. In order to determine whether the bump-like feature is significant or not, the extended emission part of the surface brightness profile was consecutively fitted with a one dimensional beta model and then a one dimensional beta model plus a gaussian fixed at the position of the bump. The two model fits were compared using the F-test in order to reject the null hypothesis saying that the bump-like feature is not significant.

The best fit parameters can be seen in Table 8 and Table 9, the fitted radial profile can be seen in Figure 38 and the F-test values are listed in Table 10. The F-test was done for the radial profile with the first and the second datapoint removed, since they are outliers in the sense that they are expected to describe the point source and the PWN, and are therefore expected to deviate from a beta model distribution.

As described in Section 6.4, a critical value of 0.05 is usually chosen for the probability, meaning that the bump in the radial profile can be deemed significant based on the F-test result. It is to be noted though that the F-test is not strictly valid in this case, since the models do not fulfill the second condition for the use of an F-test. This means that one cannot choose specific values for the second model that will reduce it to the first model, without choosing parameter values that are on the edge of the parameter space (i.e. the FWHM or the amplitude for the Gaussian). Using the forward shock radius, which is equivalent to the fitted shell radius given in Table 9, in combination with the Sedov-Taylor solutions given in Equations 5 and 6, we can determine the age of the remnant and the forward shock velocity. We adopt the rounded off value of the gaussian position parameter as the blast wave shock radius in arcsecs $\theta_s = 109$ arcsec, and we adopt the distance of $D = 13.5$ kpc from Combi et al 2006. This gives us a blast wave radius in pc:

$$R_s = \tan(\theta_s)D = 5.2 \times 10^{-4} \cdot 13.5 \times 10^3 \text{ pc} = 7.13 \text{ pc} \quad (35)$$

If we then use Equation 5, we get a lower bound on the age of the remnant by assuming that the Sedov-Taylor solutions are a good estimate of the evolution of the remnant, and by adopting a value for the number density of the assumed to be ionized ambient medium of $n \sim 0.5 \text{ cm}^{-3}$ (Ferrière 2001), and by assuming that an explosion energy of 10^{51} ergs is available for expansion.

$$t = \left(\frac{R_s \rho_0^{1/5}}{S(\gamma)E^{1/5}} \right)^{5/2} = \left(\frac{2.2 \times 10^{19} \text{ cm} \cdot (8.35 \times 10^{-25} \text{ g cm}^{-3})^{1/5}}{1.15 \cdot (10^{51} \text{ ergs})^{1/5}} \right)^{5/2} \approx 1467 \text{ yr} \quad (36)$$

This gives an expansion velocity of the forward shock of:

$$V_s = \frac{2 R_s}{5 t} = \frac{2}{5} \left(\frac{2.2 \times 10^{14} \text{ km}}{4.6 \times 10^{10} \text{ s}} \right) \approx 1913 \text{ km s}^{-1} \quad (37)$$

It is more likely though, that the remnant is in the free expansion phase, since no sign of a reverse shock wave is seen, and since the space between the PWN and the shell is vacant. For this reason we can assume an expansion velocity of the SN explosion equal to 5000 km s^{-1} (given in Section 2.2.1) and from that and the radius of the blast wave front we get an estimated age for the remnant of: $t \sim R_s/v_s = 2.2 \times 10^{14} \text{ km}/5.0 \times 10^3 \text{ km s}^{-1} \sim 1395 \text{ yr}$.

Both results point towards the remnant being young of age, and this fits well with the calculated value of the pulsar spin-down luminosity. The remnant turn out to be only slightly

older than the Crab nebula, explaining its very symmetrical form with the pulsar and the PWN located in the center of the remnant. This is evident from the radio emission shown in Figure 14 where the X-ray peak emission is well correlated to the radio peak emission. The proposed X-ray shell of the remnant is enclosed by the radio emission indicating that it is indeed a part of the remnant structure, and the gap between the shell structure and the PWN supports the claim that this remnant is a young remnant that has not reached the Sedov-Taylor phase yet. Accepting an age of ~ 1400 yr makes this remnant a historical remnant. This means that the remnant could be the relic of a core collapse supernova that exploded sometime during the early 7th century.

An interesting thing would be to investigate whether the explosion would have been visible to people on Earth, which can be found from the apparent magnitude of the explosion. The apparent magnitude can be calculated based on a general peak absolute magnitude value for a core collapse SN. The value seem to lie between ~ -19 for a SN type IIL, and ~ -17 for a SN type IIP (Richardson et al 2001). The extinction is inferred from the relation $nH = 2.2 \times 10^{21} A_V$, where nH is the column density and A_V is the extinction caused by the column density. Using the distance to the SNR, the absolute magnitude and correcting for the extinction caused by the large column density of $nH = 7.97 \times 10^{22} \text{ cm}^{-2}$ from spectral fitting, we get an apparent magnitude for a SN type IIL:

$$m = M_{\text{IIL}} - 5(1 - \log D) + A_V = -19 - 5(1 - \log(1.4 \times 10^4 \text{ pc})) + \frac{7.97 \times 10^{22} \text{ cm}^{-2}}{2.2 \times 10^{21}} = 33.0 \quad (38)$$

And for a SN type IIP:

$$m = M_{\text{IIP}} - 5(1 - \log D) + A_V = -17 - 5(1 - \log(1.4 \times 10^4 \text{ pc})) + \frac{7.97 \times 10^{22} \text{ cm}^{-2}}{2.2 \times 10^{21}} = 35.0 \quad (39)$$

The SN of G337.2+00.1 would definitely not have been observable no matter which kind of explosion it was, because of the extreme extinction in the line of sight. If no extinction had been present on the other hand, the SN event would have had a brightness comparable to that of the planet Jupiter at its brightest if it was a type IIL explosion or as the star Sirius if it had been a type IIP explosion.

Tabel 8:
Best fit parameters for Beta model fit

x_0	r0	A	β
0	$25.8^{+8.16}_{-7.28}$	$2.32e - 9^{+7.45e-10}_{-4.45e-10}$	$0.47^{+0.04}_{-0.03}$

Tabel 9:
Best fit parameters for Beta+Gaussian model fit

Beta	x_0	r0	A	β
	0	$29.98^{+8.62}_{-7.48}$	$2.26e - 9^{+5.80e-10}_{-3.85e-10}$	$0.52^{+0.06}_{-0.04}$
Gaussian	x_0	A	FWHM	
	$109^{+0.76}_{-0.53}$	$3.53e - 10^{+8.26e-8}_{-8.79e-11}$	$7.53^{+3.14}_{-5.62}$	

Tabel 10:
F-test values for the bump feature in G337.2+00.1

Beta	Beta+Gaussian	F-test value	Prob.
62.607/25	20.805/22	14.73	1.76e-5

8.2 CXOU J163802.6-471358

It is obvious from Figures 24 and 27 that the emission from this object is extended. This leaves a somewhat small number of possibilities for the source type. The ones that have been proposed (private conversation with John Tomsick) are a pulsar driving a PWN, an AGN with a jet, or a LMXB with a jet. In this thesis the focus has been on the possibility of the source being a PWN.

J1638 is a hard source, peaking at ~ 5 keV. The exposure corrected image in Figure 24 shows a compact structure with a diffuse nebula that is elongated in the Northern direction. The shape of the X-ray emission fits well with the cometary structure expected for a moving pulsar that is driving a shock either through its host remnant or the ISM (see Section 3.4). Since the radio emission from such an object is expected to form a larger structure stretching further away from the X-ray emission caused by the difference in synchrotron lifetime for high and low energy emitting electrons, contours from MGPS-2 have been added to Figure 24 for comparison. It is evident that the radio emission stretches far longer than the X-ray emission in the Northern direction, consistent with what is expected from a PWN. Furthermore is it obvious that there is an offset between the peak of the radio emission and the peak of the X-ray emission, which we will get back to later in this Section.

The source is as mentioned hard, and this is also a consequence of the severe absorbing column, as seen from Figure 21, where emission from the source is only seen above 2keV. To examine this further, three narrow band images was made splitting up the hard energy band. The three bands were chosen so that an equal amount of net counts from the source were present in each. This was done as to rule out any selection effects and in order to see how the shape of the source changes with energy. The result can be seen in Figure 23 where the scale, color bar and smoothing are equivalent for the three narrow band images. An image of the full band raw event file has been added for comparison purposes. Comparing the softest image with the hardest shows that the emission tends to clump towards the point-like source for higher energies making the point-like source more prominent, and the tail emission is observed to shrink. This is indeed what would be expected for a moving pulsar, since the high energy photons will probe the acceleration site and the lower energy photons will mostly be detected at larger distance from the pulsar and will be left behind, since the lower energy synchrotron emitting electrons will have longer synchrotron lifetimes.

A spatial spectral investigation of J1638 was performed using spectra extracted from the aperture regions shown in Figure 29 and modeling them with an absorbed power law. Because of the poor photon statistics, the full source spectrum was fitted first, and the best fit result for the column density was kept fixed for the other spectral fits. Three of the five spectra provide fairly good fits, namely the full source spectrum, the full tail spectrum and the short tail spectrum. The rest of the spectral fits are at best mediocre. The full source spectrum provided the best basis for a fit with the absorbed power law model, which strengthens the possibility that the emission is that from synchrotron emitting accelerated particles, which is expected for a PWN.

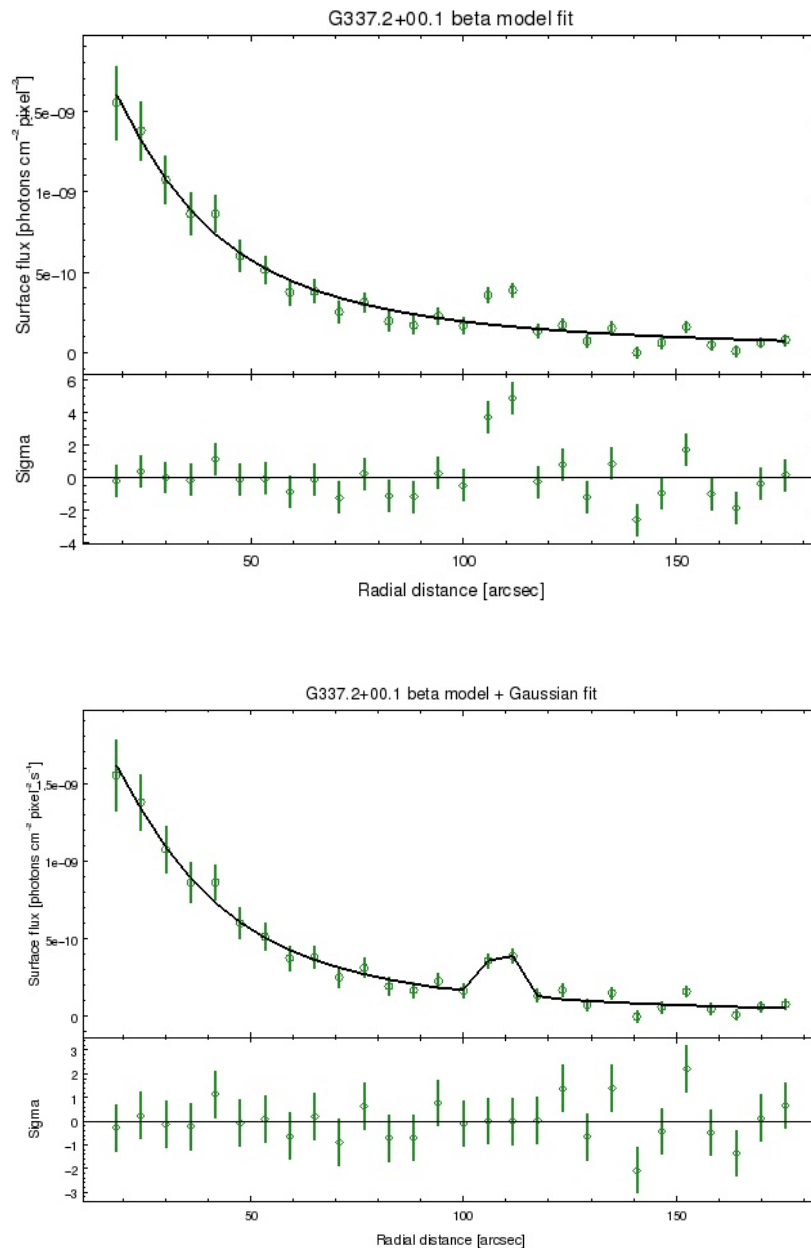


Figure 38: The full source radial profile of G337.2+00.1 fitted with a beta model in the upper panel, and with a beta model + Gaussian in the bottom panel. The fit statistics and the F-test values can be seen in Table 8, 9, and 10. The two first points of the full source radial profile has been excluded from the fit, since they are believed to describe the point-like source and the PWN.

The power law fits of the spectra show signs of softening with increasing distance from the pulsar candidate, which is expected for both young and old PWNe. However, nothing can be concluded, since better photon statistics is needed to provide better constraints on the parameters.

It was additionally attempted to fit the spectra with a thermal model, but this resulted in unconstrained parameters and unacceptable fit statistics.

A spectral investigation was also done using data from the XMM Newton telescope. A serendipitous observation of the PWN candidate was performed in 2005 August, and the data from that observation was used in order to take advantage of the great sensitivity of XMM Newton, provided by the large effective area. The source was located more than 10 arcmin off-axis, but given the large exposure time of 98 ks, the spectral information is valuable. The 3 grouped XMM spectra can be seen in Figure 31 and the full source combined Chandra spectrum can be seen in Figure 30 where it has been grouped for visualization purposes only. A lot of excess emission in the soft end of the spectrum is observable in the XMM spectra. This could be an effect caused by foreground sources (combi et al 2006).

The fits were performed separately because of the need to use different statistics for the two fits, since the XMM spectra were grouped and the Chandra spectrum was not. The best fit parameters for the XMM Newton fit are also listed in Table 6 and it is obvious that the column density is much larger than for the Chandra fit, and the spectrum is much softer. The two spectral fits are furthermore compared in Figure 32 where the top right contours are for the XMM Newton spectral fit and the bottom left contours are from the Chandra fit. The contours indicate the confidence intervals for 1σ , 2σ and 3σ and it can be seen that the 1σ contours overlap only at $\Gamma \sim 1.25$ and $nH \sim 17 \times 10^{22} \text{ cm}^{-2}$. It is curious that the XMM spectral fit results in such a large column density, but taking into account that the best fit $\tilde{\chi}^2$ takes a value of 1.36, we should accept the value with precaution. Still the column density inferred by the Chandra best-fit parameter is large, and recalling the large distance of $\sim 14 \text{ kpc}$ for G337.2+00.1 and its somewhat lower column density we can make the 14 kpc a lower bound on the distance to the PWN candidate J1638.

If we make use of this lower bound on the distance to the source, we can calculate its luminosity and from that infer the pulsar spin-down luminosity following the same procedure as for G337.2+00.1.

$$L_X = F_X 4\pi D^2 = 4\pi \cdot 4.83 \times 10^{-13} \text{ ergs cm}^{-2} \text{ s}^{-1} \cdot (4.32 \times 10^{22} \text{ cm})^2 = 1.13 \times 10^{34} \text{ ergs s}^{-1} \quad (40)$$

This is still a lower bound on the luminosity and from this we can get a lower bound on the spin-down luminosity of the pulsar candidate from the Possenti et al 2002 relation. The spin-down luminosity is then $\dot{E} = 6.78 \times 10^{36} \text{ ergs s}^{-1}$.

From Figure 27 it is easily seen that the source is asymmetric and similar in structure to what is seen for other moving pulsars (i.e. the Mouse (Gaensler et al 2004)). The source shows a peak feature with a quick decline towards the South and a much slower decline towards the tail region. The tail like feature stretches from the point-like source and approximately 10 arcsec to the North. The short part of the tail stretching out to a distance of $\sim 5 \text{ arcsec}$ can be compared to what is called the tongue in the case of the Mouse (Gaensler et al 2004). The tail is quite short, especially compared to the Mouse, but since the source only contains around 100 net counts, it is likely that the emission from a longer tail is blended into the background. As mentioned in Section 3.4 it is possible to determine the Mach number of a moving pulsar as the ratio between the forward termination shock radius and the radius of the termination shock behind the pulsar. If we assume that this source is a PWN, we can make an estimation of the Mach number by assuming that the forward termination shock is located where the emission blends into the background ($\sim 1.5 \text{ arcsec}$), and by assuming that the termination shock behind the proposed pulsar is located where the tongue emission terminates ($\sim 5 \text{ arcsec}$), which is a reasonable assumption to make, according to Gaensler et al (2004). The Mach number is then:

$$M = \frac{r_{\text{behind}}}{r_{\text{front}}} = \frac{5 \text{ arcsec}}{1.5 \text{ arcsec}} \approx 3 \quad (41)$$

This is a very crude estimate since it is done by eye and it is not certain that the X-ray emission terminates at those specific radii since the number of photons detected directly from the source is only ~ 100 net counts. A Mach number of 3 is reasonable for a pulsar traveling through its parent SNR (van der Swaluw et al 2003, see Section 3.4), but no sign of a parent SNR is seen in X-rays. However, the MGPS-2 image in Figure 10 reveals a structure that might be interpreted as a SNR. An image of the radio map centered on the PWN candidate is seen in Figure 39. The radio counterpart is obvious in the image and a radio trail is seen stretching North of the PWN candidate. The trail seem to end in a big lump of emission, but this could be a foreground source that is not linked to J1638. Both the PWN candidate and the trail is enclosed in a shell-like structure which could naively be thought off as a candidate for a host SNR.

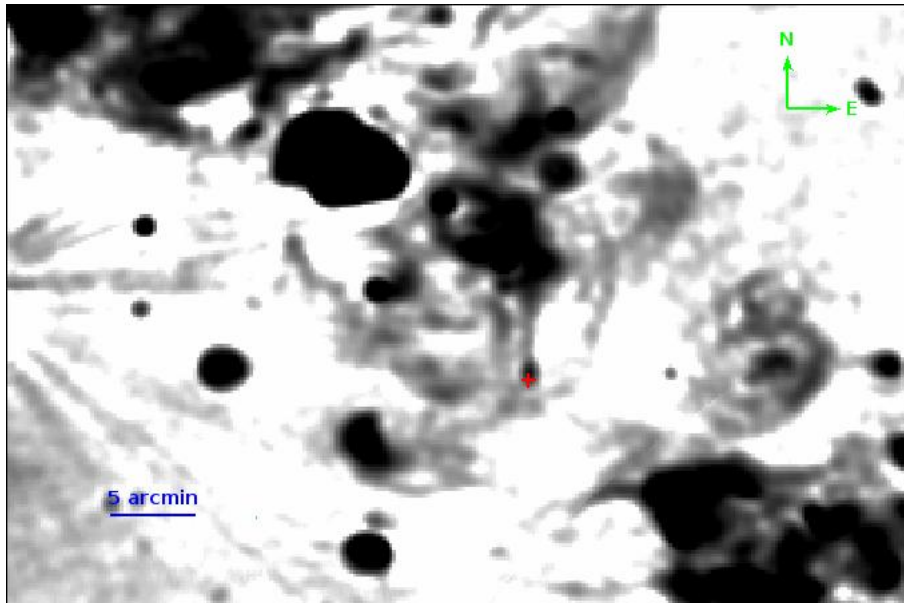


Figure 39: A MGPS-2 image of the PWN candidate CXOU J163802.6-471358 and the region around it. The red cross mark the position of the X-ray peak and radio counterpart is easily detected as a blob of emission around the cross, and as a trail stretching out in the Northern direction. A shell-like structure of radio emission is seen enclosing the emission from the PWN candidate.

The diameter of the shell-like radio emission is ~ 13 arcmin, and if we assume that it is in fact the remnant of a core collapse event producing the PWN candidate, and that it is therefore located at approximately the same distance as the PWN candidate, we can use the distance estimation based on the absorbing column determined from spectral fitting, and from that calculate the linear size:

$$R_s = \tan(\theta_s)D = 1.9 \times 10^{-3} \cdot 15.0 \times 10^3 \text{ pc} = 27 \text{ pc} \quad (42)$$

Furthermore assuming that the remnant would have been initially expanding freely with the velocity of 5000 km s^{-1} (which is the accepted initial expansion velocity of a SN of the core collapse type, see Section 2.2.1) and continued to do so until it reached its present size, we get an age estimate of: $t \sim R_s/v_s = 1.8 \times 10^{15} \text{ km}/5.0 \times 10^3 \text{ km s}^{-1} \sim 5264 \text{ yr}$. This would definitely be an underestimation of the true age, since the remnant would not be freely expanding through its lifetime, but would be decelerating when encountering the ISM. If the structure is a SNR, the size of it ($> 10 \text{ pc}$ across, see Section 2.2.4) indicates that it will have reached the radiative snowplough phase. Furthermore, it does not seem to be detectable in X-rays, but only at radio

wavelengths, which also characterizes a remnant that is in the snowplough phase. The Sedov-Taylor solutions would therefore, probably give a better estimation of the age. Using the Sedov-Taylor solutions with the assumptions about the density of the medium from the discussion of G337.2+00.1 (see the previous Section 8.1), we get an age estimate of:

$$t = \left(\frac{R_s \rho_0^{1/5}}{S(\gamma) E^{1/5}} \right)^{5/2} = \left(\frac{8.3 \times 10^{19} \text{ cm} \cdot (8.35 \times 10^{-25} \text{ g cm}^{-3})^{1/5}}{1.15 \cdot (10^{51} \text{ ergs})^{1/5}} \right)^{5/2} \approx 40550 \text{ yr} \quad (43)$$

and an expansion velocity of:

$$V_s = \frac{2 R_s}{5 t} = \frac{2}{5} \left(\frac{1.8 \times 10^{15} \text{ km}}{1.3 \times 10^{12} \text{ s}} \right) \approx 554 \text{ km s}^{-1} \quad (44)$$

As mentioned earlier, an offset is seen for the X-ray peak and the radio peak. The offset could perhaps be explained by the fact that the radio observation is a mosaic of observations performed in the years from 1998 to 2004, whereas the Chandra observation is from 2011. Assuming that the source is actually a traveling pulsar and assuming that the offset is caused by that very fact, we can calculate the pulsar proper motion. The offset is measured as the distance between the X-ray peak of emission and the radio peak of emission, and is determined as 40.5 arcsec. This amounts to a linear distance of:

$$D_{\text{offset}} = 1.9 \times 10^{-4} \text{ rad} \cdot 14 \times 10^3 \text{ pc} = 2.7 \text{ pc} \quad (45)$$

This is a rather large offset, but assuming the largest temporal offset of 13 years, the proper motion of the pulsar is:

$$V_{PSR} = D_{\text{offset}}/t_{\text{offset}} = \frac{8.3 \times 10^{13} \text{ km}}{4,0 \times 10^8 \text{ s}} = 207500 \text{ km s}^{-1} \quad (46)$$

This is of course not possible, since this means that the pulsar would be moving with a speed comparable to the speed of light in vacuum, and that even assuming that the pulsar would be traveling perpendicular to our line of sight. The offset must therefore be caused by something else.

The shape of the radio emission is also a little unusual, since the radio emission from moving pulsars often portray a cometary structure like in the X-ray regime. The radio emission from J1638 looks as if it comes from a static source. This makes it important to investigate other possibilities for the source type, for instance whether it could be an AGN with a jet, or a LMXB with a jet.

A solid detection of pulsations from the source or of a bow shock structure in H α would make a valuable and indisputable evidential for the PWN hypothesis. Unfortunately none of the above are available. It was attempted to extract temporal information from the source, but taking into account the sparse number of photons detected, it was not possible to extract anything useful from the Chandra data.

In regards to a bow shock structure in H α it is not expected that anything would show up even if we had observations available since the source is located in the Norma region, and therefore heavily obscured by the high number of molecular clouds in the region (Bronfman et al 1989). However, recently an observation of an infrared bow shock from a moving pulsar was reported in a paper released on arXiv by Wang et al (2013) reporting the serendipitous discovery of an infrared bow shock near a moving pulsar detected at 8 μm with the Spitzer space telescope. Inspired by this, and by the fact that both Spitzer observations from GLIMPSE (the Galactic

Legacy Infrared Mid-Plane Survey) and observations from the Vista all sky survey, are available for the region of the sky where J1638 is located, the plots in Figure 25 and Figure 26 were created. The Vista images show a lot of point sources and some close to the position of the pulsar candidate. None of them seem to be a counter part to the X-ray emission given the fact that the circular region marked number 1 has a size that reflects the positioning error for the X-ray peak. The Spitzer images show weak point sources as well in the vicinity of the PWN candidate in general, but neither the Vista nor the Spitzer images show any sign of diffuse emission that could be linked to the PWN candidate.

8.3 G337.8-00.1

Kes41 or SNR G337.8-00.1 is believed to be an addition to the relatively new class of remnants, namely the thermal composites or Mixed-Morphology (MM) remnants. Because this class of sources is characterized by exhibiting central compact thermal emission in the X-ray regime, it would have been interesting to do a spectral investigation of the source. Unfortunately, the far from ideal location of the remnant in all four Chandra observations (see Figure 33) does not allow us to perform such an investigation. Generally speaking, will an ARF extracted at the edge of an ACIS chip be wrong since the response tools assume that 100% of the PSF is on one chip at all times, which is probably not correct for a source close to the edge. It was instead attempted to extract a spectrum from two of the observations where the source is covered entirely on one chip, but given the fact that the source is very dim, the spectrum turned out to be very noisy and fitting it with an absorbed thermal model resulted in unconstrained parameters that were not sensitive to the fit.

This outcome is not entirely surprising since the XMM Newton spectra created by Combi et al (2008) were based on approximately the same amount of counts, and their spectrum was also affected by low photon statistics.

One thing to notice is the presence of a point source in the near vicinity of the X-ray peak determined from the XMM Newton observations. Only because of the high spatial resolution of the Chandra telescope, were we able to filter out the contribution from this unknown source. This does not seem to be the case for the XMM Newton analysis, and it was therefore attempted to extract a spectrum from that point source in order to see whether this could have had any effect on the XMM Newton spectral fit. Unfortunately, it was once more not possible to extract a useable spectrum of the source. One thing we can report on is the detection of a ring like structure seen in the North-Eastern part of the remnant (see Figure 37). This is a structure that was not observed directly in the broad band XMM Newton observation, but was revealed from a narrow band image in the 4.0-6.0 keV range as a semi-circular structure. Now we can report the detection of it in the full energy band 0.5-8.0 keV.

9 Conclusion

Based on the above it is evident that the Norma region sources suffer under the large absorbing column, leading for the most part to mediocre spectral fits and very few source counts for imaging analysis. Nevertheless, the above results and discussion offers some new insight into the nature of at least the two first sources.

9.1 G337.2+00.1

None of the results for this source contradicts the classification of G337.2+00.1 as a plerionic composite remnant. The results that supports this classification, counts:

- The resolved remnant center reveals a central point-like source surrounded by diffuse emission and the visual evidence of a half shell. This morphology is observed both visually and through a full source radial profile.
- The central diffuse emission believed to origin from a pulsar is well correlated with the radio emission and has a size that is smaller than the size of the radio emission. The shell furthermore pinpoints the location of the forward shock leading to a more secure estimate of the remnant age and expansion velocity.
- The spectral characteristics of the emission is consistent with the idea of non-thermal synchrotron emission, which supports the idea that the central diffuse emission is that from a pulsar wind nebula with a pulsar in its center.

If the feature seen as a bump in the radial profile and as a faint diffuse ring in the X-ray images of G337.2+00.1 is the manifestation of a shell, it is a sign of the SNR interacting with a denser region of the ISM. No diffuse emission is visible on the North-Eastern side of the remnant, indicating that the ISM is denser on one side than on the other. This is a common feature observed in many SNRs i.e. Kes 75 (see Figure 4). This is expected, since massive stars evolve quickly and therefor explode very close to their birth place close to dense clouds (Vink 2011).

9.2 J163802.6-471358

The idea of this source being a moving pulsar driving a bow-shock has been investigated. Most of the results seem to support this notion. Only the shape of the radio emission is somewhat different than what could be expected, but not to such a degree that it will give reason to doubt the PWN nature of the source.

- Imaging reveals a cometary structure in X-rays with an elongated tail in radio.
- The tail part of the source is observed to shrink in size with higher energy, indicating that the emission from the point-like source is harder than the emission from the tail.
- Spatial spectral investigation supports the above result.
- The spectrum is fitted well with an absorbed power law, which indicates the presence of non-thermal synchrotron emission, consistent with the pulsar hypothesis.
- The inferred spin-down luminosity of the supposed pulsar of $\dot{E} = 6.78 \times 10^{36} \text{ erg s}^{-1}$ is reasonable for a bow-shock pulsar.

- A Mach number $M=3$ is reasonable for a moving pulsar, but also indicates that the pulsar should be moving inside its host remnant, which is not directly observed in X-rays.

Further investigation is needed in order to fully reject other possibilities for the source type, such as an AGN with a jet, or a LMXB with a jet.

9.3 G337.8-00.1

This source turned out to be very dim, and therefore not suitable for spectral investigation, which is the most interesting aspect of these supposed mixed-morphology remnants. In order to say something qualitative about this source in the Chandra energy range, other more sophisticated methods are needed to achieve new insight.

10 Further investigations

Several things could be done to improve the above. One of the things that would be valuable for all three sources, because of their dim nature, is to calculate hardness ratio maps for all of them in order to infer from that their spatial spectral properties. Hardness ratio maps for the three sources were calculated during this thesis work, but more work will need to be done since a balance between the high spatial resolution of the observations and the count rate of the sources need to be determined. In order to get something qualitatively out of the maps, one needs to bin them coarsely, which erases some of the spatial information that is precious for source typing purposes. Using these maps, one can use simulated spectra, in order to translate between the hardness ratio in each pixel and the photon index of the spectrum. This of course rely on the fact that the whole source can be described by the same model.

Furthermore, none of the attempts to extract timing information from the point-like central source of G337.2+00.1 or the supposed pulsar of J1638, resulted in any useful information, caused especially by the low number of counts. For J1638 it would be interesting to look at temporal variations in the emission from the point source using the XMM data available.

It would be very useful to do a Monte Carlo simulation of the observed shell-bump in the radial profile of G337.2+00.1 to determine the significance of the detection with more accuracy, since the F-test is not strictly valid. Furthermore it would be helpful to do a 2D image fit of the shell in order to account for the overestimation of the Poisson errors for the profile.

Litteratur

- [1] F. Aharonian, A. G. Akhperjanian, A. R. Bazer-Bachi, M. Beilicke, W. Benbow, D. Berge, K. Bernlöhr, C. Boisson, O. Bolz, V. Borrel, I. Braun, F. Breitling, A. M. Brown, P. M. Chadwick, L.-M. Chounet, R. Cornils, L. Costamante, B. Degrange, H. J. Dickinson, A. Djannati-Ataï, L. O. Drury, G. Dubus, D. Emmanoulopoulos, P. Espigat, F. Feinstein, G. Fontaine, Y. Fuchs, S. Funk, Y. A. Gallant, B. Giebels, S. Gillessen, J. F. Glicenstein, P. Goret, C. Hadjichristidis, M. Hauser, G. Heinzelmann, G. Henri, G. Hermann, J. A. Hinton, W. Hofmann, M. Holleran, D. Horns, A. Jacholkowska, O. C. de Jager, B. Khélifi, N. Komin, A. Konopelko, I. J. Latham, R. Le Gallou, A. Lemièrre, M. Lemoine-Goumard, N. Leroy, T. Lohse, J. M. Martin, O. Martineau-Huynh, A. Marcowith, C. Masterson, T. J. L. McComb, M. de Naurois, S. J. Nolan, A. Noutsos, K. J. Orford, J. L. Osborne, M. Ouchrif, M. Panter, G. Pelletier, S. Pita, G. Pühlhofer, M. Punch, B. C. Raubenheimer, M. Raue, J. Raux, S. M. Rayner, A. Reimer, O. Reimer, J. Ripken, L. Rob, L. Rolland, G. Rowell, V. Sahakian, L. Saugé, S. Schlenker, R. Schlickeiser, C. Schuster, U. Schwanke, M. Siewert, H. Sol, D. Spangler, R. Steenkamp, C. Stegmann, J.-P. Tavernet, R. Terrier, C. G. Théoret, M. Tluczykont, G. Vasileiadis, C. Venter, P. Vincent, H. J. Völk, and S. J. Wagner. The H.E.S.S. Survey of the Inner Galaxy in Very High Energy Gamma Rays. *ApJ*, 636:777–797, January 2006.
- [2] J. Als-Nielsen, D. McMorro, and I. Robinson. Elements of modern x-ray physics. *Physics Today*, 55(3):030000–66, March 2002.
- [3] W. Baade and F. Zwicky. Cosmic Rays from Super-novae. *Proceedings of the National Academy of Science*, 20:259–263, May 1934.
- [4] J. Ballet. Supernova remnants. In C. Motch and J.-M. Hameury, editors, *EAS Publications Series*, volume 7 of *EAS Publications Series*, page 217, 2003.
- [5] A. Bamba, T. Anada, T. Dotani, K. Mori, R. Yamazaki, K. Ebisawa, and J. Vink. X-ray Evolution of Pulsar Wind Nebulae. *ApJ*, 719:L116–L120, August 2010.
- [6] R. Bandiera, F. Pacini, and M. Salvati. The evolution of nonthermal supernova remnants. II - Can radio supernovae become plerions? *ApJ*, 285:134–140, October 1984.
- [7] W. Becker and J. Truemper. The X-ray luminosity of rotation-powered neutron stars. *A&A*, 326:682–691, October 1997.
- [8] A. R. Bell. The acceleration of cosmic rays in shock fronts. I. *MNRAS*, 182:147–156, January 1978.
- [9] P. R. Bevington and D. K. Robinson. *Data reduction and error analysis for the physical sciences*. 2003.
- [10] F. Bocchino and A. M. Bykov. The plerion nebula in IC 443: The XMM-Newton view. *A&A*, 376:248–253, September 2001.
- [11] L. Bronfman, H. Alvarez, R. S. Cohen, and P. Thaddeus. A deep CO survey of molecular clouds in the southern Milky Way. *ApJS*, 71:481–548, November 1989.
- [12] N. Bucciantini, J. M. Blondin, L. Del Zanna, and E. Amato. Spherically symmetric relativistic MHD simulations of pulsar wind nebulae in supernova remnants. *A&A*, 405:617–626, July 2003.

-
- [13] A. M. Bykov, F. B. S. Paerels, and V. Petrosian. Equilibration Processes in the Warm-Hot Intergalactic Medium. *Space Sci. Rev.*, 134:141–153, February 2008.
- [14] J. L. Caswell, D. H. Clark, D. F. Crawford, and A. J. Green. Molonglo and Parkes Supernova Remnant Observations. *Australian Journal of Physics Astrophysical Supplement*, 37:1, 1975.
- [15] R. A. Chevalier. Self-similar solutions for the interaction of stellar ejecta with an external medium. *ApJ*, 258:790–797, July 1982.
- [16] S. A. Colgate and C. McKee. Early Supernova Luminosity. *ApJ*, 157:623, August 1969.
- [17] J. A. Combi, J. F. Albacete-Colombo, and J. Martí. Discovery of thermal X-ray emission in the supernova remnant G337.8-0.1 (Kes 41). *A&A*, 488:L25–L28, September 2008.
- [18] J. A. Combi, P. Benaglia, G. E. Romero, and M. Sugizaki. <ASTROBJ>G337.2+0.1</ASTROBJ>: A new X-ray supernova remnant?. *A&A*, 431:L9–L12, February 2005.
- [19] D. P. Cox, R. L. Shelton, W. Maciejewski, R. K. Smith, T. Plewa, A. Pawl, and M. Różyczka. Modeling W44 as a Supernova Remnant in a Density Gradient with a Partially Formed Dense Shell and Thermal Conduction in the Hot Interior. I. The Analytical Model. *ApJ*, 524:179–191, October 1999.
- [20] W. Cui and D. P. Cox. Two-temperature models of old supernova remnants with ion and electron thermal conduction. *ApJ*, 401:206–219, December 1992.
- [21] A. Decourchelle. Elemental composition and distribution in SNRs: X-ray spectroscopy. *New A Rev.*, 48:75–79, February 2004.
- [22] A. Decourchelle, D. C. Ellison, and J. Ballet. Thermal X-Ray Emission and Cosmic-Ray Production in Young Supernova Remnants. *ApJ*, 543:L57–L60, November 2000.
- [23] V. V. Dwarkadas and R. A. Chevalier. Interaction of Type IA Supernovae with Their Surroundings. *ApJ*, 497:807, April 1998.
- [24] E. Fermi. On the Origin of the Cosmic Radiation. *Physical Review*, 75:1169–1174, April 1949.
- [25] G. Ferrand and S. Safi-Harb. A census of high-energy observations of Galactic supernova remnants. *Advances in Space Research*, 49:1313–1319, May 2012.
- [26] K. M. Ferrière. The interstellar environment of our galaxy. *Reviews of Modern Physics*, 73:1031–1066, October 2001.
- [27] A. V. Filippenko. Optical Spectra of Supernovae. *ARA&A*, 35:309–355, 1997.
- [28] C. J. Foot. *Atomic Physics*. Oxford University Press, 2005.
- [29] B. M. Gaensler and P. O. Slane. The Evolution and Structure of Pulsar Wind Nebulae. *ARA&A*, 44:17–47, September 2006.
- [30] B. M. Gaensler, E. van der Swaluw, F. Camilo, V. M. Kaspi, F. K. Baganoff, F. Yusef-Zadeh, and R. N. Manchester. The Mouse that Soared: High-Resolution X-Ray Imaging of the Pulsar-powered Bow Shock G359.23-0.82. *ApJ*, 616:383–402, November 2004.

-
- [31] N. Gehrels. Confidence limits for small numbers of events in astrophysical data. *ApJ*, 303:336–346, April 1986.
- [32] P. Ghavamian, W. P. Blair, R. Sankrit, J. C. Raymond, and J. P. Hughes. The Detection of Far-Ultraviolet Line Emission from Balmer-Dominated Supernova Remnants in the Large Magellanic Cloud. *ApJ*, 664:304–321, July 2007.
- [33] V. L. Ginzburg and S. I. Syrovatskii. The Origin of Cosmic Rays. In *International Cosmic Ray Conference*, volume 1 of *International Cosmic Ray Conference*, page 48, 1967.
- [34] T. Gold. Rotating Neutron Stars as the Origin of the Pulsating Radio Sources. *Nature*, 218:731–732, May 1968.
- [35] E. V. Gotthelf, B. Koralesky, L. Rudnick, T. W. Jones, U. Hwang, and R. Petre. Chandra Detection of the Forward and Reverse Shocks in Cassiopeia A. *ApJ*, 552:L39–L43, May 2001.
- [36] D. A. Green. A revised Galactic supernova remnant catalogue. *Bulletin of the Astronomical Society of India*, 37:45–61, March 2009.
- [37] E. A. Helder, D. Kosenko, and J. Vink. Cosmic-ray Acceleration Efficiency versus Temperature Equilibration: The Case of SNR 0509-67.5. *ApJ*, 719:L140–L144, August 2010.
- [38] J. R. Hörandel. Cosmic-ray composition and its relation to shock acceleration by supernova remnants. *Advances in Space Research*, 41:442–463, 2008.
- [39] F. Hoyle, J. V. Narlikar, and J. A. Wheeler. Electromagnetic Waves from Very Dense Stars. *Nature*, 203:914–916, August 1964.
- [40] H.-T. Janka, K. Langanke, A. Marek, G. Martínez-Pinedo, and B. Müller. Theory of core-collapse supernovae. *Phys. Rep.*, 442:38–74, April 2007.
- [41] E. M. Jones, B. W. Smith, and W. C. Straka. Formation of supernova remnants - The pre-blast-wave phase. *ApJ*, 249:185–194, October 1981.
- [42] J. S. Kaastra, F. B. S. Paerels, F. Durret, S. Schindler, and P. Richter. Thermal Radiation Processes. *Space Sci. Rev.*, 134:155–190, February 2008.
- [43] V. M. Kaspi. Radio pulsar/supernova remnant associations. *Advances in Space Research*, 21:167–176, 1998.
- [44] J. G. Kirk, Y. Lyubarsky, and J. Petri. The Theory of Pulsar Winds and Nebulae. In W. Becker, editor, *Astrophysics and Space Science Library*, volume 357 of *Astrophysics and Space Science Library*, page 421, 2009.
- [45] B. Leibundgut. Type Ia Supernovae. *A&A Rev.*, 10:179–209, 2000.
- [46] D. A. Liedahl. The X-Ray Spectral Properties of Photoionized Plasma and Transient Plasmas. In J. van Paradijs and J. A. M. Bleeker, editors, *X-Ray Spectroscopy in Astrophysics*, volume 520 of *Lecture Notes in Physics*, Berlin Springer Verlag, page 189, 1999.
- [47] C. F. McKee. X-Ray Emission from an Inward-Propagating Shock in Young Supernova Remnants. *ApJ*, 188:335–340, March 1974.
- [48] C. F. McKee and D. J. Hollenbach. Interstellar shock waves. *ARA&A*, 18:219–262, 1980.
-

-
- [49] C. F. McKee and J. P. Ostriker. A theory of the interstellar medium - Three components regulated by supernova explosions in an inhomogeneous substrate. *ApJ*, 218:148–169, November 1977.
- [50] F. Melia. *High-Energy Astrophysics*. 2009.
- [51] R. Mewe. Atomic Physics of Hot Plasmas. In J. van Paradijs and J. A. M. Bleeker, editors, *X-Ray Spectroscopy in Astrophysics*, volume 520 of *Lecture Notes in Physics*, Berlin Springer Verlag, page 109, 1999.
- [52] R. Minkowski. Spectra of Supernovae. *PASP*, 53:224, August 1941.
- [53] A. Possenti, R. Cerutti, M. Colpi, and S. Mereghetti. Re-examining the X-ray versus spin-down luminosity correlation of rotation powered pulsars. *A&A*, 387:993–1002, June 2002.
- [54] M. Renaud, V. Marandon, E. V. Gotthelf, J. Rodriguez, R. Terrier, F. Mattana, F. Lebrun, J. A. Tomsick, and R. N. Manchester. Discovery of a Highly Energetic Pulsar Associated with IGR J14003-6326 in the Young Uncataloged Galactic Supernova Remnant G310.6-1.6. *ApJ*, 716:663–670, June 2010.
- [55] S. P. Reynolds. Supernova Remnants at High Energy. *ARA&A*, 46:89–126, September 2008.
- [56] S. P. Reynolds. Synchrotron-Loss Spectral Breaks in Pulsar-Wind Nebulae and Extragalactic Jets. *ApJ*, 703:662–670, September 2009.
- [57] D. Richardson, R. C. Thomas, D. Casebeer, Z. Blankenship, S. Ratowt, E. Baron, and D. Branch. SUSPECT - The Online Supernova Spectrum Database. In *American Astronomical Society Meeting Abstracts*, volume 33 of *Bulletin of the American Astronomical Society*, page 1428, December 2001.
- [58] S. Safi-Harb. Plerionic supernova remnants. In F. A. Aharonian, W. Hofmann, and F. M. Rieger, editors, *American Institute of Physics Conference Series*, volume 1505 of *American Institute of Physics Conference Series*, pages 13–20, December 2012.
- [59] R. Schaeffer. Supernovae. In C. Motch and J.-M. Hameury, editors, *EAS Publications Series*, volume 7 of *EAS Publications Series*, page 155, 2003.
- [60] F. D. Seward and Z.-R. Wang. Pulsars, X-ray synchrotron nebulae, and guest stars. *ApJ*, 332:199–205, September 1988.
- [61] S. L. Shapiro and S. A. Teukolsky. *Black holes, white dwarfs, and neutron stars: The physics of compact objects*. 1983.
- [62] D. H. Sharp. An overview of Rayleigh-Taylor instability. *Physica D Nonlinear Phenomena*, 12:3–3, July 1984.
- [63] P. A. Shaver and W. M. Goss. Galactic Radio Sources II: High Resolution 408 MHz observations. *Australian Journal of Physics Astrophysical Supplement*, 14:77, 1970.
- [64] R. L. Shelton, K. D. Kuntz, and R. Petre. Chandra Observations and Models of the Mixed-Morphology Supernova Remnant W44: Global Trends. *ApJ*, 611:906–918, August 2004.

-
- [65] P. Slane, Y. Chen, N. S. Schulz, F. D. Seward, J. P. Hughes, and B. M. Gaensler. Chandra Observations of the Crab-like Supernova Remnant G21.5-0.9. *ApJ*, 533:L29–L32, April 2000.
- [66] J. R. Taylor. *Introduction to Error Analysis, 2nd Ed. (cloth)*. University Science Books, 1997.
- [67] J. K. Truelove and C. F. McKee. Evolution of Nonradiative Supernova Remnants. *ApJS*, 120:299–326, February 1999.
- [68] E. van der Swaluw, A. Achterberg, Y. A. Gallant, T. P. Downes, and R. Keppens. Interaction of high-velocity pulsars with supernova remnant shells. *A&A*, 397:913–920, January 2003.
- [69] S. D. Van Dyk, C. Y. Peng, A. J. Barth, and A. V. Filippenko. The Environments of Supernovae in Post-Refurbishment Hubble Space Telescope Images. *AJ*, 118:2331–2349, November 1999.
- [70] B. van Veelen, N. Langer, J. Vink, G. García-Segura, and A. J. van Marle. The hydrodynamics of the supernova remnant Cassiopeia A. The influence of the progenitor evolution on the velocity structure and clumping. *A&A*, 503:495–503, August 2009.
- [71] J. Vink. Supernova remnants: the X-ray perspective. *A&A Rev.*, 20:49, December 2012.
- [72] Z. Wang, D. Kaplan, P. Slane, N. Morell, and V. Kaspi. Serendipitous Discovery of An Infrared Bow Shock Near PSR J1549-4848 with Spitzer. April 2013.
- [73] R. L. White and K. S. Long. Supernova remnant evolution in an interstellar medium with evaporating clouds. *ApJ*, 373:543–555, June 1991.
- [74] J. B. Z. Whiteoak and A. J. Green. The MOST supernova remnant catalogue (MSC). *A&AS*, 118:329–380, August 1996.
- [75] J. Wilms, A. Allen, and R. McCray. On the Absorption of X-Rays in the Interstellar Medium. *ApJ*, 542:914–924, October 2000.
- [76] S. Woosley and T. Janka. The physics of core-collapse supernovae. *Nature Physics*, 1:147–154, December 2005.